12-2007

MIXED CONVECTIVE HEAT TRANSFER AND EVAPORATION AT THE AIR-WATER INTERFACE

Prasad Gokhale
Clemson University, pgokhal@clemson.edu

MIXED CONVECTIVE HEAT TRANSFER AND EVAPORATION AT THE AIR-WATER INTERFACE

A Thesis
Presented to
the Graduate School of
Clemson University

In Partial Fulfillment
of the Requirements for the Degree
Master of Science
Mechanical Engineering

---

by
Prasad N. Gokhale
August 2007

Accepted by:
Dr. John R. Saylor, Committee Chair
Dr. Richard S. Figliola
Dr. Donald E. Beasley

ABSTRACT

Functional forms for mixed convective heat transfer and evaporation from an air-water interface were obtained. To obtain these functions, heat transfer and evaporation rates from the air-water interface of an evaporating body of water were quantified in a wind/water tunnel in the presence of an oleyl alcohol monolayer on the water surface. The Nusselt (Nu) and Sherwood (Sh) numbers, parameterizing the dimensionless heat and mass transfer respectively, for transport from the water bulk to air were expressed as functions of the air side Rayleigh (Ra) and Reynolds (Re) numbers. The Nu and Sh were calculated for a range of Ra from 1.1×10^7 to 4.1×10^7 and a range of Re from 0 to 3.5×10^5. Power law $Nu(Ra)$ and $Nu(Re)$ relationships parameterizing natural and forced convective heat transfer respectively were then obtained as were $Sh(Ra)$ and $Sh(Re)$ relationships parameterizing natural and forced convective evaporation.

Mixed convective $Nu(Ra, Re)$ and $Sh(Ra, Re)$ functions were formulated using a vectorial additive model having an exponent of four. These functions predicted the experimentally obtained $Nu(Ra)$, $Nu(Re)$, $Sh(Ra)$ and $Sh(Re)$ relationships with reasonable accuracy. From the $Nu(Ra)$, $Nu(Re)$, $Sh(Ra)$ and $Sh(Re)$ results as also from the results of the mixed convective equations, it was concluded that the mixed convective regime lay between 1 - 3 m/s i.e. $0.6 \times 10^5 < Re < 2.1 \times 10^5$ for both heat and mass transfer.

To obtain repeatable results and for these results to be applicable to field conditions, a monolayer of oleyl alcohol was applied to the water surface to maintain spatially and temporally consistent surface conditions. An IR camera was used to visualize the surface flow and to judge the homogeneity of the surfactant film. It was found that the oleyl alcohol monolayer applied to the water surface formed a homogenous surfactant film thus ensuring consistent conditions for all experiments.

DEDICATION

To my mother, Anuradha Gokhale.

ACKNOWLEDGMENTS

I would like to thank the following people for their assistance and advice that helped me complete this research project successfully: Dr. Peter Judd for his guidance and assistance with the experimental work for my thesis; Dr. Tim Conover for lending me the pump that helped me start my experiments; Dr. Dennis Stevenson for his assistance in understanding the basics of the statistical methods employed for this research project; Mr. David Moline for his guidance on using Matlab with greater effect; Mrs. Barbara Ramirez for her guidance with writing and revising this thesis and Michael Justice, Jamie Cole and Gerald Nodine for their help in setting up my experimental facility. I would also like to thank my advising committee for their time and feedback that helped improve my thesis.

I would like to thank my fellow graduate students and friends Jie Kou, Na Geng, Ray McDonnel, Paul Wright, Steven Bower, Justin Lapp, Nithya Sivasubramanian, R. J. Lee, Diana Lang, Gavin Wiggins and Miheer Gurjar for their valuable advice, assistance and the long discussions on the intricacies of this project. I am also grateful to my good friend Liz Stephen for her friendship.

Finally, I want to thank my graduate advisor Dr. John Saylor, for his guidance and insight which has helped me better myself as a student, researcher and technical writer and will hold me good stead during any future academic and professional undertakings.

TABLE OF CONTENTS

LIST OF TABLES

LIST OF FIGURES

1 INTRODUCTION

Convection can be classified into three categories depending on the mechanism of heat transfer, the three categories being natural, forced and mixed convection. Irrespective of the category, the heat transfer during convection is described using Eq. (1), which is also known as Newton's law of cooling:

$$q_1'' = \frac{h_t}{\Delta T} \tag{1}$$

where q_1'' is the convective heat flux from the system, ΔT the characteristic temperature difference between the heat exchanging media and h_t the heat transfer coefficient. Newton's law of cooling is used to model the temperature change of an object of some temperature placed in an environment of a different temperature. Research on heat transfer often involves the measurement of the heat transfer coefficient, which is affected by particular boundary conditions and a number of thermodynamic and transport properties of the fluid. A discussion of each of the above mentioned categories of convection is given below.

1.1 Natural convection

Consider a fluid layer which is confined between two isothermal plates maintained at different temperatures as shown in Fig. 1. This is a typical setup for studying Rayleigh-Bénard convection, where the fluid layer is heated from below and cooled from above to produce a fixed temperature difference. This results in heating and consequent expansion of the bottom fluid layer and cooling and contraction of the top fluid layer thus producing an unstable density gradient in the fluid layer. If the density gradient is sufficiently strong, the hot fluid will rise and the cooler fluid at the top will sink, causing a buoyancy driven convective flow which results in enhanced transport

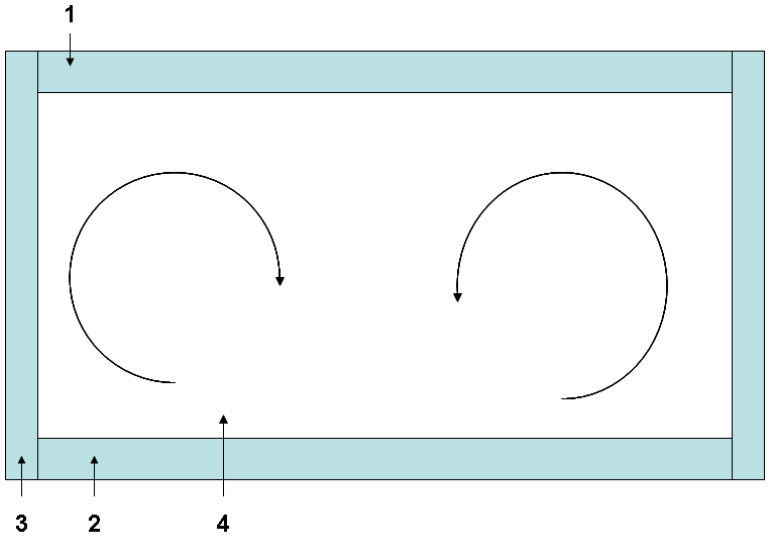

Figure 1: Typical experimental setup for Rayleigh-Bénard convection: 1) Cold plate, 2) hot plate, 3) walls, 4) fluid layer.

of heat between the two plates. This form of convection, where a fluid is confined between a bottom hot plate and a top cold plate to induce buoyancy driven convection is known as Rayleigh-Bénard convection. A measure of the thermal instability causing a buoyant flow within a fluid is given by the Rayleigh number defined as:

$$Ra = \frac{\beta g \Delta T L^3}{\nu \alpha} \tag{2}$$

where ΔT is the characteristic temperature difference, which in the case of Rayleigh-Bénard convection is the temperature difference between the two plates, L is the characteristic length scale, which is the distance between the two plates, α the thermal diffusivity of the fluid, β the thermal expansion coefficient, ν the kinematic viscosity of the fluid and g is the acceleration due to gravity. The Rayleigh number can also be defined as the product of the Grashof number, which approximates the ratio of the buoyancy to viscous forces acting on a fluid, and the Prandtl number, which

approximates the ratio of momentum diffusivity and thermal diffusivity. The Grashof and Prandtl numbers are defined as:

$$Gr = \frac{\beta g \Delta T L^3}{\nu^2} \tag{3}$$

$$Pr = \frac{\nu}{\alpha} \tag{4}$$

where Gr is the Grashof number and Pr is the Prandtl number. The onset of buoyancy driven convection occurs when the Rayleigh number is greater than a critical value which in the case of Rayleigh-Bénard convection is approximately 1700.[1]

While the thermal instability in the fluid during buoyancy driven convection is quantified using the Rayleigh number, the dimensionless heat transfer during this process is quantified using the Nusselt number. The Nusselt number is a dimensionless heat transfer coefficient and quantifies the enhancement of heat transfer in comparison to that of just conduction. The Nusselt number is defined as:

$$Nu = \frac{h_t L}{k} \tag{5}$$

where k is the thermal conductivity of the fluid.

Natural convective heat transfer is a function of the thermal instability driving heat transfer and the Prandtl number. The Nusselt number for natural convection is thus parameterized according to the form:

$$Nu_n = \text{function}(Ra, Pr) \tag{6}$$

where Nu_n is the Nusselt number for natural convection. The nature of this functional relationship for natural convective heat transfer has been the subject of many studies in the past. These studies have established that a power law relationship exists between the Nusselt, Rayleigh and Prandtl numbers having the form:

$$Nu_n = A(Ra)^b(Pr)^x \tag{7}$$

where A, b and x are constants. Various authors, having conducted research on natural convective heat transfer, have obtained different values for these constants.[2–29] These researchers have found that the value of the exponent b lies between 0.25 and 0.34 with most of these studies showing effectively a $\frac{1}{3}$ power law relationship between Nu and Ra. The value of A varies considerably from 0.06 to 0.1[2–29] depending on the geometry of the setup whereas the exponent of the Prandtl number has been found to vary between 0.05 and 0.1.[2–29] The power law is often used to model transport relationships because it is a result obtained from theoretical studies on the subject of natural convective heat transfer. Though the heat transfer and consequently the Nusselt number will also depend on the aspect ratio of the container in which natural convection is studied, this is not the focus of the research done for this thesis. As most of the past research on natural convective heat transfer has focused on Rayleigh-Bénard convection, presented below are two classic studies on the subject. A reason for presenting these particular studies is that the power law relationship between Nu and Ra demonstrated by these researchers falls close to the limits of the range of exponents which have been obtained by various researchers.

Globe and Dropkin[3] studied Rayleigh-Bénard convection for different fluids. They aimed to obtain the $Nu(Ra, Pr)$ relationship over a range of $1.51 \times 10^5 < Ra < 6.76 \times 10^8$ and $0.02 < Pr < 8750$. Their results indicate that the heat transfer rate for their entire range of Ra and Pr may be determined by the relationship:

$$Nu_n = 0.069(Ra)^{0.33}(Pr)^{0.074} \tag{8}$$

This Rayleigh number exponent of approximately 0.33 or $\frac{1}{3}$ is a classic result seen by many researchers studying Rayleigh-Bénard convection.[3–6,9–18,21–23]

In a similar study, Chu and Goldstein[2] studied Rayleigh-Bénard convection in a water layer. Their study focused on obtaining a relationship between Nu and Ra and explaining the mechanism governing heat transfer in natural convection. For the range of Rayleigh numbers explored by them ($2.76 \times 10^5 < Ra < 1.05 \times 10^8$), their results showed the exponent of the Rayleigh number to be equal to 0.28. Though this result is close to the classic $\frac{1}{3}$ power law relationship between Nu and Ra, it is one of the small number of studies[2,24–29] demonstrating a Rayleigh number exponent smaller than 0.3. They also showed that natural convective heat transfer in their setup was driven by the formation of thermal plumes which originated from the bottom plate.

Most of the studies cited above address natural convection between solid boundaries and few have addressed natural convection when the upper boundary is a free surface. Several researchers have studied natural convective heat transfer and evaporation and provided empirical relations governing this process.[30–37] However most these studies focus on obtaining the evaporation rate and completely neglect the heat transfer accompanying evaporation. Notable exceptions to this are the studies by Sparrow[38] and by Katsaros *et al.*[4] Katsaros *et al.* investigates natural convective heat transfer from an evaporating water surface. This study is thus closely aligned

with the work done for this thesis as it addresses the transport process at the air-water interface. The authors chose the form shown in Eq. (7) to describe their results for natural convective heat transfer from hot water to air. The equation provided by them is:

$$Nu_n = 0.156(Ra)^{0.33} \tag{9}$$

This equation agrees well with the classical $\frac{1}{3}$ power law relationship for natural convection.

1.2 Forced convection

Forced convection is heat transfer due to an externally imposed flow, where the flow can be imposed by a pressure gradient or an external shear on the fluid. A measure of the forced flow is given by the Reynolds number:

$$Re = \frac{UL}{\nu} \tag{10}$$

where U is the characteristic velocity and L is the characteristic length, which, for forced convection is typically the length of the fluid medium along the flow direction. For forced convection, heat transfer is typically parameterized according to:

$$Nu_f = \text{function}(Re, Pr) \tag{11}$$

where Nu_f is the Nusselt number for forced convection. The nature of the functional relationship between Nu, Pr and Re has been studied by many researchers in the

past,[39–50] establishing a power law relationship between the Nusselt, Reynolds and Prandtl numbers such as:

$$Nu_f = C(Re)^d(Pr)^y \tag{12}$$

where C, d and y are constants. Most researchers studying forced convective heat transfer have found the exponent d to have a value between 0.5 and 0.8.[40–44,46] This result is clearly demonstrated by a number of researchers for a variety of surface geometries. The value of the constant C has been reported to be typically between 0.1 and 0.9[39–50] whereas the exponent of the Prandtl number is reported to be approximately 0.3.[40–42,47,48]

1.3 Mixed convection

Sometimes the mechanisms responsible for natural and forced convection can be simultaneously present and exert comparable influence on the transport process. This phenomenon is known as mixed convection or combined convection.

Because mixed convection consists of both forced and natural convection, the Nusselt number for mixed convection is a function of Re, Ra and Pr:

$$Nu_m = \text{function}(Re, Ra, Pr) \tag{13}$$

where Nu_m is the Nusselt number under mixed convective conditions. The Reynolds number is a measure of the forced flow within a fluid and the Rayleigh number is a measure of the thermal instability in a fluid, thus another way of presenting the Nusselt number in a mixed convective flow is:

$$Nu_m = \text{function}(Nu_n, Nu_f) \tag{14}$$

The functional form adopted by several researchers to model this mixed convective relationship is:

$$Nu_m \;=\; (Nu_n^n + Nu_f^n)^{\frac{1}{n}} \tag{15}$$

where n is a constant optimized to best fit the experimental data.[51–56] This is a vectorial addition of the Nusselt numbers for natural and forced convective heat transfer alone. Proof of the validity of this form for modeling mixed convective results is given by Jackson and Yen[57] who first suggested this form for modeling mixed convection. A thorough literature search failed to reveal another functional form to model mixed convective heat transfer.

Some of the earliest known research on mixed convection was done by Sparrow and co-workers.[58,59] Sparrow and Gregg[58] studied mixed convection over horizontally oriented flat plates while Mori[59] studied this phenomenon over vertical plates. Later researchers have focused mainly on horizontally oriented flat plates[46,59–62] and cylinders,[53,63,64] these setups being most relevant to the study of electronics cooling and solar and other heat exchangers. However, most of these are numerical studies which focus on studying mixed convection under varying thermal conditions e.g. isothermal flat plates, imposed temperature gradient on flat plates, etc. The focus of this thesis is the study of mixed convective heat transfer and evaporation at an air-water interface. Thus, mixed convection studies in general and those at an air-water interface in particular will be used to understand the basics of this topic.

An air-water interface geometrically resembles a flat plate, thus mixed convection

studies over flat plates will also be used to understand this interfacial phenomenon. The study presented below is most relevant to the work done for this thesis as it addresses mixed convection over a horizontal flat plate and attempts to obtain a functional relationship for mixed convective heat transfer of the form described in Eq. (15).

Oosthuizen and Bassey[46] conducted a series of experiments which focussed on flow over a solid plate for the assisting and opposing flow scenarios. A flow is said to be assisting, when the direction of the buoyant force is the same as the direction of the forced velocity, whereas an opposing flow is where the buoyant force opposes the forced velocity. The assisting or opposing flow was initiated by inclining the plate at various angles to the forced flow, varying the plate position from being horizontally oriented to being vertically oriented. The researchers proposed a functional relationship between the relevant dimensionless groups of the form:

$$Nu = \text{function}(Re, Gr, Pr, \alpha) \tag{16}$$

α being the angle of inclination of the flat plate to the flow. To obtain this functional relationship describing mixed convection, the authors had to first get individual relationships for natural and forced convection similar to Eqs. (7) and (12), respectively and combine them as shown in Eq. (14). They obtained an equation which best described the natural convection data by carrying out tests at zero wind speed and then fitting the experimental data to an equation of the form:

$$Nu_n = 0.42Gr^{0.25} \tag{17}$$

Experiments were then conducted over a range of wind speeds, with Gr varied at

each wind speed. Using their experimental data for constant Grashof number forced velocity runs, which was achieved by maintaining a fixed temperature difference between the flat plate and the free stream, the authors obtained a relationship between Nu and Re for forced convection which was:

$$Nu_f = 0.59Re^{0.5} \tag{18}$$

Thus, after obtaining separate equations for the forced and natural convection regimes, a model for the mixed convective regime was obtained as shown in Eq. (15) by vectorially adding the results for the above two cases as follows:

$$Nu_m \ = \ (Nu_n^n + Nu_f^n)^{1/n} \tag{19}$$

The value of the exponent n being four. Though Oosthuizen and Bassey[46] do not provide a reason for the use of a fourth order fit, one assumes that it provided the best fit to the data. By substituting Eqs. (17) and (18) in to Eq. (19), the authors obtain an equation which describes the $Nu(Gr, Re)$ behavior over the entire experimental range:

$$Nu = [(0.42Gr^{0.25})^4 + (0.59Re^{0.5})^4]^{\frac{1}{4}} \tag{20}$$

Oosthuizen and Bassey[46] thus obtained a relationship for mixed convective heat transfer and that work will be used to guide efforts towards formulating a $Nu(Ra, Re)$ model from the experimental data for this thesis, with the exponent n optimized to give the best fit results.

1.4 Interfacial transport

All the studies mentioned above focus on mixed convection over vertically and horizontally oriented solid plates or other solid geometries such as ducts, cylinders etc. A thorough search of past literature revealed very few relevant studies which focused on mixed convective transport at the air-water interface,[32,33] demonstrating that though widespread, this phenomenon is poorly understood. Understanding mixed convection at an air-water interface is important for quantifying the heat transfer taking place in industrial cooling ponds and other inland water bodies such as lakes. These inland water bodies are used as repositories of waste heat for industries. This waste heat disposal affects aquatic life and can severely disturb the limnological ecological balance. Another important field where the results from such a study would be applicable is in the study of global heating and cooling cycles which is relevant to global warming.

Consider a body of water with the surface exposed to the ambient, where the water temperature is higher than the air temperature as shown in Fig. 2. Energy loss from water to the ambient in such a setup is due to convection, latent heat loss due to evaporation, radiation and wall heat loss:

$$q = q_1 + q_2 + q_3 + q_4 \tag{21}$$

Where q is the total energy loss from the water, q_1 is the heat loss due to convection, q_2 is the energy loss due to evaporation, q_3 is wall heat loss and q_4 is the net heat loss due to radiation. The mass loss due to evaporation from the water surface to air is due to the water vapor concentration difference between the water surface and the air. For air flowing over a water body, the air is saturated at the interface[31,65] while the free stream vapor concentration depends on the psychrometric conditions of air. For the situation where the air is cooler than the water, as is the case for the research

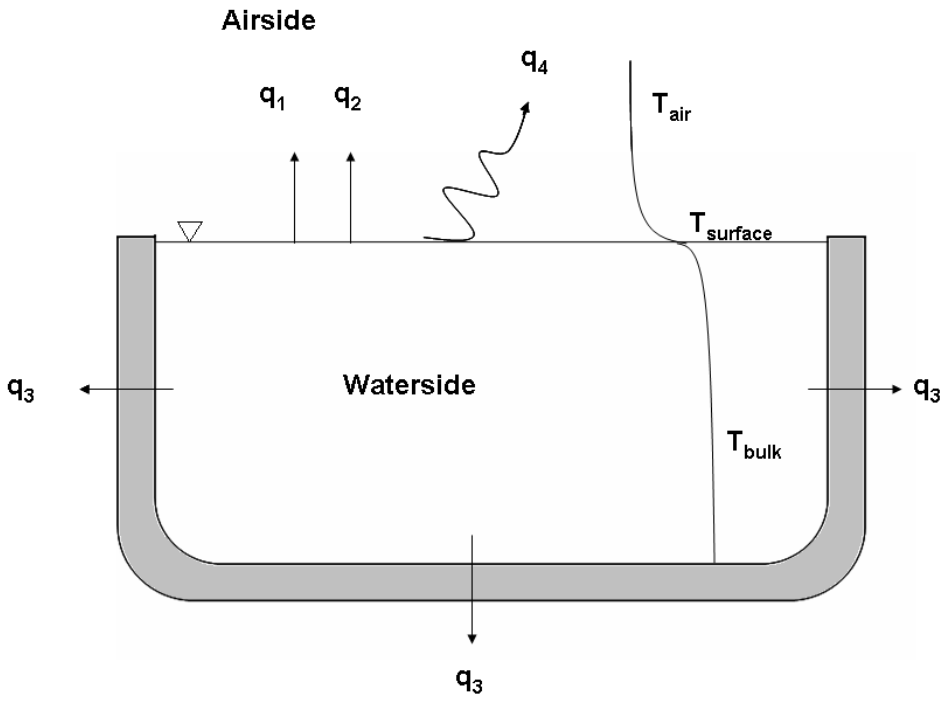

Figure 2: Typical experimental setup for studying interfacial transport: 1) q_1 is the convective heat loss, 2) q_2 is the evaporative loss, 3) q_3 is the wall heat loss and 4) q_4 is the radiative heat loss.

conducted for this thesis, the energy for evaporation is provided by the internal energy of the water. The mass flux from a free water surface due to evaporation is:

$$\dot{m}'' = h_m(\rho_i - \rho_a) \tag{22}$$

where $\dot{m}''$ is rate of evaporation in $\frac{\text{kg}}{\text{s}\cdot\text{m}^2}$, h_m is the mass transfer coefficient for water in $\frac{\text{m}}{\text{s}}$ and ρ_i and ρ_a are water vapor densities at the interface and in the free stream in $\frac{\text{kg}}{\text{m}^3}$. Here, the saturated vapor at the interface is assumed to be an ideal gas. The rate of energy loss due to evaporation from the water surface is:

$$q_2 = \dot{m}'' A \cdot h_{fg} \tag{23}$$

where A is the water surface area over which evaporation occurs and h_{fg} is the latent heat of vaporization of water at the water surface temperature. Once the losses due to evaporation, radiation and the wall heat loss are deducted from the total energy loss from the water, the convective heat transfer from water to air can be quantified. The method for calculating the wall heat loss and the radiation loss will be presented in Section 3.2.

The Sherwood number, which is a dimensionless mass transfer coefficient is defined as:

$$Sh = \frac{h_m L}{D} \tag{24}$$

where Sh is the Sherwood number, L the characteristic length and D the diffusion coefficient of water in air. Just as various studies have established relationships

between Nu, Ra, Re and Pr for heat transfer under natural and forced convective conditions, similar relationships have been established between Sh, Ra, Re and Sc for mass transfer under natural[32] and forced convective conditions:[66–70]

$$Sh_n = A_1(Ra)^{b_1}(Sc)^{x_1} \tag{25}$$

$$Sh_f = C_1(Re)^{d_1}(Sc)^{y_1} \tag{26}$$

where A_1, b_1, x_1, C_1, d_1 and y_1 are functional constants of the natural and forced convective power law relationships for mass transfer. Sc is the Schmidt number defined as:

$$Sc = \frac{\nu}{D} \tag{27}$$

The Schmidt number, which is a dimensionless number approximating the ratio of momentum diffusivity and mass diffusivity, is used to characterize transport processes where there are simultaneous momentum and mass diffusion convection processes. Equations describing the $Sh(Ra, Re)$ relationships which are similar to the $Nu(Ra, Re)$ relationships presented in Section 1.3 will be developed for the research presented here as follows:

$$Sh_m \ = \ (Sh_n^p + Sh_f^p)^{\frac{1}{p}} \tag{28}$$

where p is the exponent of the vectorial model and is optimized iteratively. Studies which focus on mixed convective mass transfer will be discussed later in conjunction with other works that are used to guide the research done for this thesis.

1.4.1 Surfactants

The word surfactant originates from the term 'surface active agent'.[71] Surfactants are substances which are adsorbed at the interface between two phases of the same or of different materials such as an air-water interface.[71] In nature, surfactants are omnipresent in natural and man-made water bodies[71] such as lakes, rivers and cooling ponds. The research conducted for this thesis focuses on transport at the air-water interface, where surfactants naturally collect, and a brief discussion of these compounds is now presented.

Surfactants belong to a category of compounds known as amphiphiles[71] which are compounds having a water soluble (hydrophilic) part and a water insoluble (hydrophobic) part. Thus, surfactants present in water tend to accumulate at the air-water interface with the hydrophilic part immersed in water and the hydrophobic part oriented away from the water in a layer which is one molecule thick as shown in Fig. 3.[71] This mono-molecular formation of surfactant molecules at the interface is known as a monolayer.

The hydrodynamic boundary condition on the free surface of water varies depending on the presence or absence of a surfactant monolayer. In the absence of a surfactant, the hydrodynamic boundary condition on the water surface is a shear free boundary condition, whereas the presence of a surfactant monolayer imparts elasticity to the water surface[71] changing the boundary condition at the interface to a shear supporting constant elasticity boundary condition. The elasticity of the surfactant monolayer is given by the following relation:

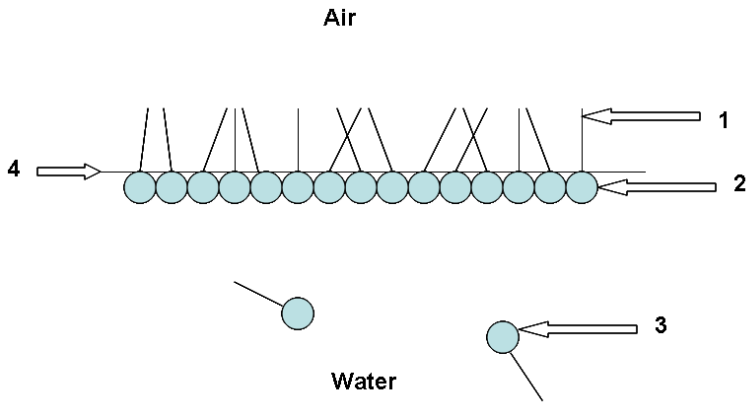

Figure 3: Surfactant monolayer at an air-water interface:[71] 1) Hydrophobic part, 2) hydrophilic part, 3) dissolved surfactant, 4) air-water interface.

$$\varepsilon = \frac{\partial \sigma}{\partial (lnA)} \tag{29}$$

where ε is the elasticity of the film, σ the surface tension of the film and A the area over which the film exists.[72,73] This elasticity damps near surface turbulence[74] and reduces the velocity of water imparted by the presence of an air current above the water surface.[74,75] The elasticity of the water surface imparted to it by the surfactant monolayer,[73,75] as defined in Eq. (29), determines the extent of this damping.[74] Surfactants also decrease the range of turbulent length scales and the number of structures on the surface.[74] The subsurface turbulence plays an important role in interfacial transport, thus the presence of surfactants can alter transport at the interface. Another important effect of having a surfactant film on the water surface is the retardation of evaporation of water from the free surface, which can affect the rate of energy loss from the water surface.[73,75] Due to these reasons, for any study on heat and mass transport at an air-water interface the surfactant concentration on the surface should be precisely known and controlled.

1.5 Interfacial mixed convective heat transfer

Convective heat transfer at an air-water interface depends on the convective processes occurring on both sides of that interface. For example, when the water is warmer than the air, the warmer water heats the bottom layer of air causing it to rise, thus creating buoyant flow in the air. At the same time the water is cooled at the surface resulting in the cooled heavier water sinking into the bulk and thus driving natural convection on both sides of the air-water interface. If wind were to be present under either of these situations, it would result in the presence of either natural, mixed or forced convection dominated conditions depending on the strength of the buoyancy driven flows on both sides of the interface and on the strength of the wind. When the air is warmer than the water, it results in stable stratification of both water and air and no buoyancy, thus if wind were present, forced convection would be the only possible transport regime on either side of the interface. Under the first situation, the possibility of the existence of mixed convection on either side of the interface is a real one.

Table 1 shows all the combinations of the different convective regimes that can exist at the air-water interface. The numbers indicate the regime number for the particular air and water conditions. The regimes marked 'M' indicate the presence of mixed convection for either the air side, the water side or both and are the focus of this thesis. Though regime numbers 1, 3 and 4 have been explored in the research presented here, they are not the focus of this thesis. A note should be made of regime 2 which was not explored in the research presented here as such conditions can only exist when forced convection is induced in water by some mechanism other than a forced air velocity e.g. pumping of water, downhill flow etc. Thus, this regime of heat transfer was not explored as the research done for this thesis deals with situations where the forced velocity in water is induced by wind.

Figure 4 is a probability density function (pdf) showing the annual wind speed

Table 1: Convective regimes at the air-water interface

Convective regimes	Air forced	Air mixed	Air natural
Water forced	1	M	2
Water mixed	M	M	M
Water natural	3	M	4

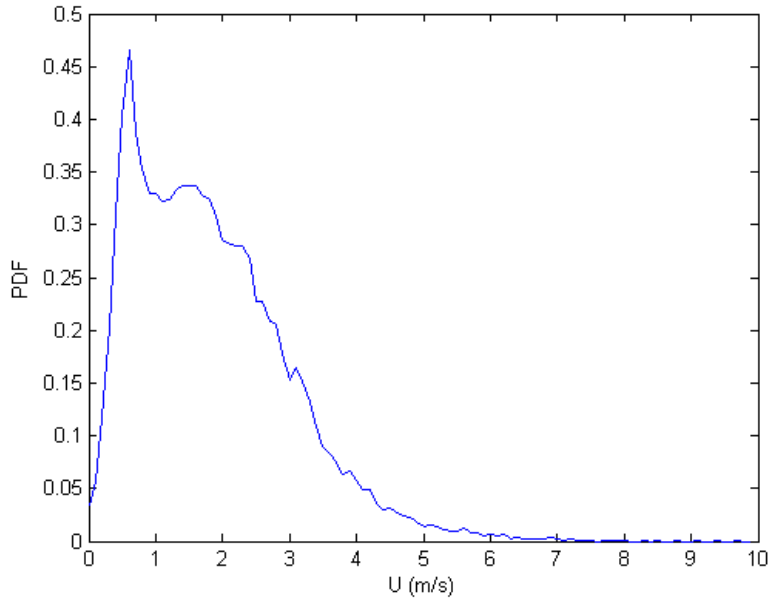

Figure 4: Annual wind speed distribution over the Savannah River Site[76]

distribution obtained near a lake at the Department of Energy (DOE) Savannah River Site in Aiken, South Carolina.[76] It is evident from this figure that limnological conditions are characterized by wind speeds lower than 4 m/s. Such low wind speeds are characteristic of wind speed conditions over inland water bodies in the U.S.A.[77] As shown by Rasmussen *et al.*,[35] this is the range of wind speeds over which combined forced and natural convection exist over lakes and cooling ponds. It is thus evident that mixed convection is an important transport regime over inland water bodies and thus needs to be better understood.

For an air-water system, the heat transfer between the air and water is quantified

using the heat transfer coefficient defined as:

$$h_t = \frac{q_1''}{\Delta T} \tag{30}$$

where h_t is the convective heat transfer coefficient, q_1'' the convective heat flux and ΔT is the temperature difference driving the heat transfer. This temperature difference can be that between the water surface and either the bulk air or the bulk water depending on what side of the air-water interface is being investigated. Thus the heat transfer coefficient can be defined in such a way that its value will be different for the air side and the water side.

The temperature difference between the bulk water and the bulk air is referred to here as the gross temperature difference between the fluids. This temperature difference is the driving force behind the gross convective (sensible) heat transfer taking place in the air-water system. This is so because, while the water surface serves as a heat transfer conduit between the bulk water and the bulk air, ultimately it is the subsurface water which loses its heat to the air. This gross temperature difference driving the heat transfer is:

$$\Delta T_g = T_b - T_a \tag{31}$$

where T_a is the bulk air temperature and T_b the bulk water temperature.

While the gross temperature difference ultimately drives the heat transfer from water to air, the mass transfer is due to the water vapor density difference between the surface and the air. However for reasons discussed in Section 1.6, this temperature difference between the water surface and the free stream could not be used to

quantify the mass transfer. Instead, the gross temperature difference was used to characterize mass transfer as well. The errors introduced in the results and any resultant qualitative change in the mass transfer relationships due to this assumption will be discussed in Section 4. To investigate this change a measure of the temperature difference between the water surface and the ambient (air side temperature difference) will be obtained as described in Section 1.6.

On the air side, ΔT_a will be the temperature difference driving the heat transfer.

$$\Delta T_a = T_s - T_a \tag{32}$$

where T_s is the water surface temperature. On the water side, ΔT_w is the temperature difference.

$$\Delta T_w = T_b - T_s \tag{33}$$

The air and water side temperature differences are later used to compute the resistance to heat and mass transfer presented by the water and air side respectively.

While the Rayleigh and Reynolds numbers quantify natural and forced convection respectively, the term that quantifies the relative influence of these terms on the transport process, and thus the presence or absence of a mixed convective regime, is the term 'G':

$$G = \frac{Ra}{Re^2 \cdot Pr} \tag{34}$$

This term G was derived by Oosthuizen[78] by an order of magnitude analysis that uses assumptions based on the characteristics of the boundary layer. This term is basically a form of the Richardson number (Ri), the relationship between them being:

$$G = \frac{Ri \cdot \beta \cdot \Delta T \rho_0}{\Delta \rho} \tag{35}$$

This analysis provides for mixed convective flow by considering the buoyancy force to be more or less equally influential to the forced flow. Oosthuizen derived this term by analyzing the characteristics of a boundary layer over an inclined solid plate. The boundary layer mentioned above exists at the air-water interface and influences the transport at the interface. The analysis done by Oosthuizen to obtain this term G is presented below.

For any kind of forced flow, Oosthuizen[78] accounted for the effect of buoyancy in the momentum equation by the addition of the following buoyancy term on the right hand side of the momentum equation.

$$\beta g(T_s - T_b)\cos\phi \tag{36}$$

where ϕ is the angle between the direction of the forced velocity and the direction of the buoyancy force, g the acceleration due to gravity, T_s the water surface temperature, T_b the bulk water temperature and β the thermal expansion coefficient. Thus, the momentum equation accounting for the buoyancy force was written as:

$$u\frac{\partial u}{\partial x} + \nu\frac{\partial u}{\partial y} = \frac{-1}{\rho}\frac{dp}{dx} + \nu\frac{\partial^2 u}{\partial y^2} + \beta g(T_s - T_b)\cos\phi \tag{37}$$

This equation was then non-dimensionalized to get the following equation:

$$u_* \frac{\partial u_*}{\partial x_*} + \frac{v_* L}{\delta} \frac{\partial u_*}{\partial y_*} = -\frac{dp_*}{dx_*} + \frac{\nu L}{\delta^2 U} \frac{\partial^2 u_*}{\partial y_*^2} + \frac{\beta g (T_s - T_b) \cos\phi \; L}{U^2} \tag{38}$$

where δ is the boundary layer thickness and the asterisk indicates the dimensionless form of the variable. These dimensionless variables are defined as:

$$u_* = \frac{u}{U} \tag{39}$$

$$v_* = \frac{v}{U} \tag{40}$$

$$x_* = \frac{x}{L} \tag{41}$$

$$y_* = \frac{y}{\delta} \tag{42}$$

$$p_* = \frac{p}{\rho U^2} \tag{43}$$

Oosthuizen further conducted an order of magnitude analysis of Eq. (38). Assuming that the x-direction velocity is of order 'U', u_* will be of order one, similarly x_* and

y_* will also be of order one due to the scaling variables selected. It can be deduced from an order of magnitude analysis of the continuity equation, that v_* is of order δ/L in the boundary layer and hence negligible and since the pressure is scaled with the stagnation pressure, p_* will also be of order one. Hence, Eq. (38) was written in terms of the orders of magnitude of its terms as follows:

$$\theta(1)\frac{\theta(1)}{\theta(1)} + \frac{\theta(\delta/L)}{\theta(\delta/L)}\frac{\theta(1)}{\theta(1)} = -\frac{\theta(1)}{\theta(1)} + \theta(\frac{L^2}{\delta^2 Re})\frac{1}{\theta(\delta/L)}\frac{\theta(1)}{\theta(1)} + \theta(G) \tag{44}$$

where 'θ' indicates the order of a term. In the term $\frac{L^2}{\delta^2 Re}$, the value of $\frac{L^2}{\delta^2}$ is very small while the value of Re will be very large for a boundary layer, thus it can be seen that G will be important if it is of order one or greater. Thus Oosthuizen concluded that forced convective flow will dominate if G is of an order lower than one, mixed convection will exist if G is of order one, and if it is of an order much greater than one then natural convective flow will dominate.

The parameter G was further manipulated as shown in Eq. (45) to get it in the form $\frac{Ra}{Re^2 \cdot Pr}$ which is in fact equal to $\frac{Gr}{Re^2}$. It should be noted that Oosthuizen looks at the scenario here where the flow is either assisting or opposing. Thus, the value of $cos\phi$ will be equal to ± 1. However, as comparisons between the forced and natural convective forces are based on the order of magnitude of the term G, only the absolute value of G is important. The parameter range for these experiments is enumerated in Section 3.

$$G = (\frac{\beta g(T_s - T_b) cos\phi \; L^3}{\nu^2})(\frac{\nu^2}{U^2 L^2}) = \frac{Ra}{Re^2 \cdot Pr} = \frac{Gr}{Re^2} \tag{45}$$

Thus it can be seen that as G gives the comparative influence of forced and free

convection in a flow, it can be used as a tool for the comparison and analysis of experimental results and to differentiate between different convective regimes. However, it should be noted that for the case of a forced flow over an air-water interface, ϕ will always be 90° and thus the analysis breaks down and cannot be used for the situation here as the buoyancy term shown in Eq. (36) will always be equal to zero. Thus, the effectiveness of this term in differentiating between transport regimes for the research done for this thesis is to be verified. A decision on the applicability of the term G to the present research will be made in Section 5.

With the exception of the study by Katsaros, the studies supporting this work that have been presented all dealt with natural, forced or mixed convection over flat plates or others solid geometries. Though these studies are important to understand the basic mixed convective process, they cannot be used as precedents to understand interfacial mixed convective transport. Very few authors have studied this interfacial transport phenomenon. Presented next is a work by Pauken which studies the mass transfer process under mixed convective conditions.

Among the many works on evaporative mass transfer,[32,35,66,69] the only work which studies the evaporative mass transfer process from a free surface under mixed convective conditions is the study by Pauken.[32] In this study the author conducted experiments for wind velocities from 1 m/s to 3 m/s and modeled the results for forced and natural convection as shown in Eqs. (46) and (47) respectively.

$$Sh_f = \text{function}(Re, Sc) \tag{46}$$

$$Sh_n = \text{function}(Gr_m, Sc) \tag{47}$$

where Sh_f is the Sherwood number under forced convective conditions, Sh_n the Sherwood number under natural convective conditions and Gr_m the mass transfer Grashof number which is defined as:

$$Gr_m = \frac{\rho(\rho_a - \rho_i)L^3}{\mu^2} \tag{48}$$

where μ is the dynamic viscosity of air.

Pauken obtained the following equations describing turbulent evaporation of hot water in a cold air stream:

$$Sh_f = 0.036 Sc^{\frac{1}{3}} Re^{0.8} \tag{49}$$

$$Sh_n = 0.14(Gr_m Sc)^{\frac{1}{3}} \tag{50}$$

These results were then vectorially added to give the functional form for the mixed convective regime, in a manner similar to the mixed convective Nusselt number function given in Eq. (19).

$$Sh_m = (Sh_f^p + Sh_n^p)^{\frac{1}{p}} \tag{51}$$

It was shown before, that the term $\frac{Ra}{Pr \cdot Re^2}$ i.e. $\frac{Gr}{Re^2}$ is a useful tool to distinguish between convective regimes and was thus used by Pauken. However, Pauken employs a variant of this term to distinguish between convective regimes, this term being $\frac{Gr_m}{Re^2}$.

The data obtained by Pauken is for $0.1 < \frac{Gr_m}{Re^2} < 10$. Pauken observed that for this range of $\frac{Gr_m}{Re^2}$, the effect of natural convection could not be neglected anywhere, whereas the contribution of forced convection to the total mass transfer falls below 10% for $\frac{Gr_m}{Re^2} > 5.0$. For the convective regime explored here, Pauken obtains the following expression which describes the nature of the mass transfer process:

$$Sh_m = (Sh_f^3 + Sh_n^3)^{\frac{1}{3}} \tag{52}$$

Although many researchers have studied evaporation and provided empirical relations governing this process,[30–37] most of these studies focus on obtaining the evaporation rate and completely neglect the heat transfer accompanying evaporation. A notable exception is the study by Katsaros *et al.*[4] However, these authors define the Nusselt number based on the heat transfer from water due to convection and evaporation and do not account for the fact that heat loss due to evaporation from the water will be comparable to convective heat loss. Thus Katsaros *et al.* don't account for the large contribution of evaporation to the cooling process while defining the Nusselt number. Thus, the Nusselt number obtained by them is effectively defined on the basis of heat lost due to mass transfer in conjunction with that lost due to the convective heat transfer process. Another difference between this study and the research conducted for this thesis is that the study by Katsaros *et al.* only explores evaporative heat transfer in the natural convective regime, without the presence of wind over the water surface and without surfactants. However, although this work does not focus on mixed convection at an air-water interface, it may be useful to compare the natural convection results obtained by Katsaros *et al.* to that from the present work.

The study by Pauken effectively explores the mixed convective regime with respect

to mass transfer, however they do not employ surfactants to ensure consistent surface conditions and also no surface observational tools to check the consistency of surface conditions. The authors also do not explore the completely forced convective regime, the forced convective component was obtained from a Sherwood number having at least some natural convective component. In spite of these differences from the present work, this work is selected for comparison and as a guiding tool for the proposed research, in conjunction with the studies by Oosthuizen[46] and Katsaros,[4] as these were the studies which were closest to the research presented here in terms of the experimental scenario and the research objectives. Though each is limited in its scope, together they provide valuable groundwork on which this research project can be based.

1.6 Experimental limitations

Although the concentration difference driving mass transfer is due to the temperature difference between the water surface, T_s, and the free stream, T_a, the gross temperature difference was used instead to compute this concentration difference. An infrared (IR) camera was utilized to observe flow on the water surface. These IR images permit measurement of T_s. However, the total uncertainty in the IR temperature measurement was large. Thus, surface temperature measurements were not used to quantify the heat transfer from water and the gross temperature difference was used instead. This method is justified as irrespective of the water surface temperature, it is the gross temperature difference between the bulk water and the ambient that drives the heat transfer process.

A similar argument, however, cannot be made for mass transfer, which should ideally be calculated using the water vapor density difference between the water surface and the ambient, the former obtained from measured surface temperature using the IR camera or from estimates from past research. However, as stated before, water

surface temperature measurements made using the IR camera had large uncertainties, in some cases the uncertainty being larger than the measurement itself.

The value of ΔT_w is largest at higher water temperatures i.e. at the start of each experiment and smallest at the end. For a maximum ΔT_w of 5 °C at the start of an experiment, a conservative estimate obtained from measurements made using the IR camera and also from results presented by past researchers,[79] the saturation density at the surface calculated using the bulk water temperature will increase by approximately 23% from that calculated using the surface temperature. Similarly, for the minimum estimated value of ΔT_w of 0.5°C at the end of an experiment, the saturation density calculated using the bulk water temperature increases by 4% from that calculated using the surface temperature. Thus the use of the bulk temperature to calculate the density at the surface is feasible. However, this increase in saturation density will affect the $Sh(Ra)$ results, the extent and nature of which will be analyzed in Section 5.4. The estimates for surface temperature were obtained from preliminary surface temperature measurements. This was corroborated by Judd[79] who showed surface temperature to differ from the bulk temperature by 1 to 5°C.

Here, it should be noted that though the IR camera will not be used to obtain water surface temperature time traces, it will be used to observe flow on the water surface. The IR camera will also be used to judge the homogeneity of the surface film.

2 OBJECTIVES

The objectives of this thesis are as follows:

1. To determine whether natural and forced convective heat transfer at an air-water interface can be modeled by power law relationships. To formulate functional relationships between the Nusselt number and the Rayleigh and Reynolds numbers i.e. $Nu(Ra)$ for natural convection and $Nu(Re)$ for forced convection, in the form:

$$Nu = ARa^b \tag{53}$$

$$Nu = CRe^d \tag{54}$$

   where A, C, b and d are empirically determined constants.

2. To determine whether natural and forced convective mass transfer at an air-water interface can be modeled by power law relationships. To formulate $Sh(Ra)$ and $Sh(Re)$ relationships defining natural and forced convective evaporative mass transfer respectively, which will be in the form:

$$Sh = A_1 Ra^{b_1} \tag{55}$$

$$Sh = C_1 Re^{d_1} \tag{56}$$

where A_1, C_1, b_1 and d_1 are empirically determined constants.

3. To determine whether mixed convective heat transfer and evaporation at the air-water interface can be defined by expressing the Nusselt and Sherwood numbers as functions of the Rayleigh and Reynolds numbers. To formulate equations describing the heat transfer and evaporative mass transfer in the mixed convective regime as a function of Ra and Re i.e. $Nu(Ra, Re)$ and $Sh(Ra, Re)$ for heat and mass transfer respectively. These equations will be of the form:

$$Nu = [(CRe^d)^n + (ARa^b)^n]^{\frac{1}{n}} \tag{57}$$

$$Sh = [(C_1Re^{d_1})^p + (A_1Ra^{b_1})^p]^{\frac{1}{p}} \tag{58}$$

4. To investigate whether the mixed convective regime lies between wind speeds of 0 - 5 m/s for the present experimental setup.

3 EXPERIMENTAL METHOD

3.1 Experimental apparatus

The experiments conducted for this thesis are performed in a wind/water tunnel facility. The wind/water tunnel is constructed by attaching a water tank to the test section of a wind tunnel. The wind/water tunnel is fabricated from wood, sheet metal, gasket material and Plexiglas and consists of a blower, isolator section, diffuser section, test section and a water tank. A schematic of the experimental setup is shown in Fig. 5.

A one HP, 1745 rpm Dayton blower which provides the forced air flow necessary for the experiments, is connected to the power supply through a Fuji AF-300 Mini speed controller, which controls the blower rpm accurately from 30 rpm to 1745 rpm with an uncertainty of $\pm$ 5 rpm. Thus a range of wind speeds from 0.05 m/s to 5 m/s with an uncertainty of $\pm$ 0.02 m/s (which translates into an uncertainty of $\pm$ 5 rpm in the blower rpm) is obtained. The wind speeds were measured using a hot wire anemometer, thus this procedure effectively amounted to hot wire calibration of the blower controls. This uncertainty is calculated by recording the wind speed at 5 minute intervals over a period of three hours and then computing the standard deviation of each point from the mean of the time trace.

A vibration isolator connects the blower to the diffuser section of the wind tunnel. The isolator serves to isolate vibrations caused by the blower, preventing them from being transmitted to the test section. The diffuser has an area contraction ratio of 4, is fabricated from sheet metal and has a honeycomb flow straightener installed at its downstream end. This straightener serves to break any large turbulent eddies into smaller ones, thus promoting uniform flow at the test section inlet.

The test section, fabricated from Plexiglas, is connected to the diffuser and is 1.145 m long with a glass water tank attached to its floor at its downstream end. This water

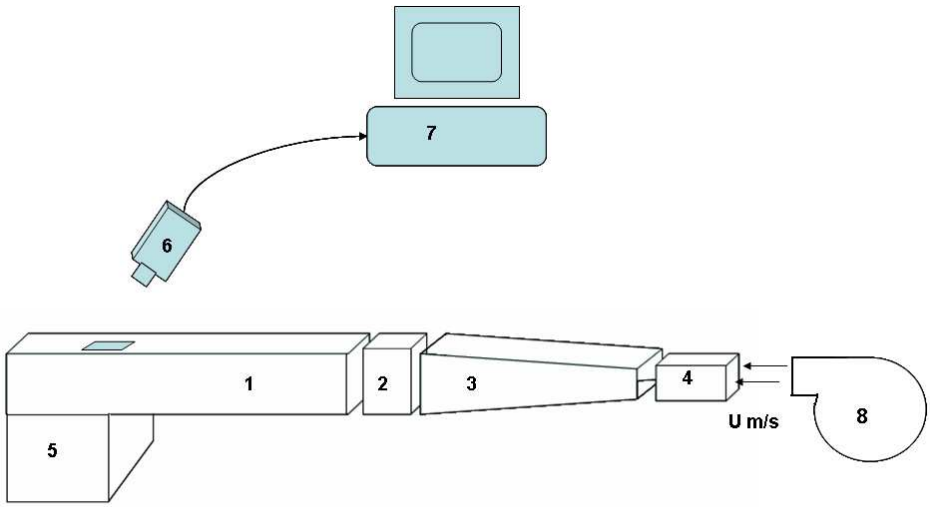

Figure 5: Schematic of the experimental setup: (1) Test section, (2) honeycomb section, (3) flow diffuser, (4) vibration isolator, (5) water tank, (6) infrared camera, (7) computer for data storage/processing, (8) blower.

tank, which is 0.27m long, 0.254m wide and 0.31m deep, is covered on all sides except the top surface by one half inch of Dow polyurethane Weathermate insulation board. This board reduces wall heat loss from the sides of the tank, thus ensuring that the dominant heat losses are due to the evaporative and convective losses from the water to the ambient. The water tank serves as a control volume in which the mixed convective effect can be studied, and is coupled to the wind tunnel in such a way that once full, the water level is flush with the floor of the test section. The glass tank and the Plexiglas enclosure are sealed using GE RTV silicone adhesive (type 110). The silicone was allowed to cure for one day and the water tank was soaked in water for an additional day after the curing process. This process ensured leak-proof and clean experimental conditions.

The electronic instrumentation consists of an infrared camera and a Fluke Chubb E-4 temperature logger with two temperature measurement probes. One probe is a dedicated bulk water temperature probe while the second is a dedicated bulk air

Table 2: Wind speed at different locations above the water surface at the center of the tank for a nominal velocity of 5 m/s

Location above water surface	left wall (m/s)	center (m/s)	right wall (m/s)
10 cm	5.10	5.00	4.99
20 cm	5.00	5.09	5.09
30 cm	4.99	4.99	4.99

temperature probe. A DigiSense HydrologR thermohygrometer is used to record relative humidity in the laboratory during the experiment. The water side thermistor is located in the geometric center of the tank, the air side thermistor is in the plenum and the thermohygrometer is placed in the laboratory to log humidity values. The water surface is observed using an Inframetrics SC1000 infrared (IR) camera having an FOV of 16°. The infrared camera is mounted on a movable platform on top of the test section in such a way that it looks down and at an angle of 16° upon the water surface. Specifically, this angle eliminates the narcissus spot, the cold array reflection from the water surface appearing as a black spot in an image. An additional reason for setting up the camera at an angle to the normal is to avoid the evaporating water rising up which can penetrate and damage the camera's optical system. Plexiglas is opaque to infrared radiation and thus a small opening at the top of the test section allows radiation from the surface of the water to be captured by the camera.

A TSI model 231 hot wire anemometer is used to measure wind speeds at the downstream end of the wind tunnel. The total uncertainty in measurements made by the anemometer is ± 0.01 m/s. Wind speed measurements are taken at the center of the tank at nine different locations spatially in the plane perpendicular to the water surface and facing the test section exit. The wind speed at all these locations varies by less than 5% of the centerline velocity as shown in Table 2.

A mass balance, which has an uncertainty of ±0.1 mg is used to measure the rate of evaporation from the tank. The balance and the entire mechanism used to

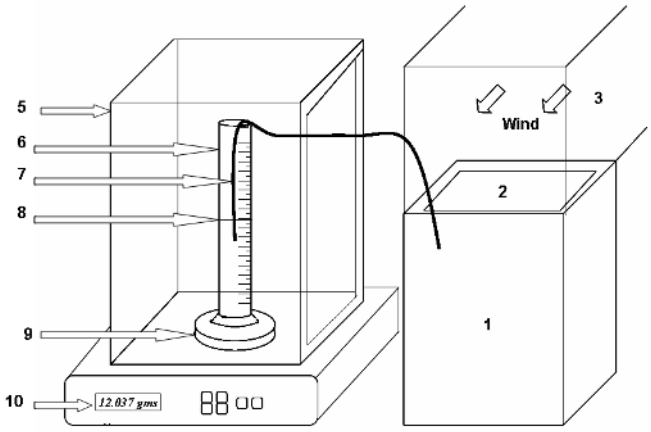

Figure 6: The evaporation measurement bench: (1) Water tank, (2) water bulk, (3) test section, (4) wind direction, (5) weighing scale enclosure, (6) cylinder, (7) water line, (8) water level in cylinder, (9) weighing platform, (10) display.

quantify the rate of evaporation is shown in Fig. 6 (not to scale), which shows the mass balance placed next to the wind tunnel. The mass flux measurement apparatus consists of a 50mL graduated glass cylinder placed on a weighing scale. This entire apparatus is then placed on a wooden platform in such a way that at least half of the height of the cylinder is above the water level in the tank. This platform is not shown in the diagram. The cylinder is connected to the tank with a small length of tubing, one end of which is submerged in the tank, providing a siphon between the two containers. To avoid fluctuations in the water level due to the formation of waves on the water surface, the tank-side end of the tube is submerged far upstream in the tank as the amplitude of waves is a minimum in this region. The cylinder holds a small volume of water and its level equilibrates with that of the main tank.

Because the tube is connected to the wind tunnel which is a source of vibrations, care is taken to ensure that the tube does not touch the cylinder. A 100% relative humidity environment is required inside the balance to avoid evaporation of water in the cylinder preventing any error due to evaporation from the cylinder. This is ensured by keeping a small beaker full of warm water inside the balance enclosure.

The water in this beaker evaporates to saturate the air inside the balance in less than 5 minutes, thus ensuring that any changes in water level in the cylinder are solely due to the water level in the cylinder responding to changing water levels in the tank. The relative humidity in the enclosure was typically measured to be 98 - 100%, thus, though the air inside the beaker wasn't fully saturated the evaporation rate from the beaker was negligible. This was confirmed by measuring evaporation from the beaker over a period of one full day. The weighing scale is placed on an optical table which is supported on an inner tube which isolates the weighing scale and reduces any background vibrations from the lab.

3.2 Experimental procedure

The water for the experiments is taken directly from the tap, its temperature at the start of each run being approximately 41°C. The tank is filled until the water surface is flush with the lower wall of the test section. Once the tank is full, the mass flux measuring apparatus is connected to the tank and the water in the two vessels is allowed to equilibrate. Next the IR camera is turned on and the thermistor probes positioned in and above water. This is followed by swiping the water surface with lab wipes to remove any indigenous surfactant on the water surface, which is immediately followed by the surfactant film application to the water surface to prevent any indigenous surfactant diffusing back to the water surface. Details regarding the surfactant application are described in Section 3.3.

Data collection begins an hour after the blower is started to allow the setup to reach a steady state. A typical experiment ran for three hours, during which time the bulk air and water temperatures and the relative humidity are logged at the rate of one data value every 30 seconds. The mass balance also recorded data every 30 seconds. The time rate of decay of the mass balance time trace gave the mass loss rate which is then used to calculate the Sherwood number.

The water temperature range for these experiments is selected to give a range in Ra from 2×10^9 to 2.2×10^{10} while at the same time ensuring that the Boussinesq approximation[78] is not violated. The Boussinesq approximation assumes that the density difference within the fluid is small enough to be neglected, except where it appears in terms multiplied by g, the acceleration due to gravity. The underlying essence of the Boussinesq approximation is that the difference in inertia is negligible but gravity is sufficiently strong to make the specific weight appreciably different between the two fluids. For the range of temperatures selected, the Boussinesq approximation was not violated:

$$\frac{|\Delta\rho|}{\rho_0} = \beta|\Delta T_w| < 1 \tag{59}$$

Here $\Delta\rho$ is the difference in densities of the bulk and surface water at the maximum bulk water temperature of 41°C, ρ_0 is the density of the bulk water at the maximum temperature of 41°C and β is the coefficient of volume expansion. Similarly, ΔT_w is the temperature difference between the bulk water and the surface water when the bulk water temperature is 41°C and T_0 is the maximum water temperature of 41°C. This equation shows that at the highest temperature of 41°C, the ratio between the density difference of the bulk and the surface water and the bulk water density is smaller than one. Here, the surface water temperature was set to be 5°C below the bulk water temperature. This estimate is the higher limit of the water side temperature difference as shown by Judd[79] and also from preliminary measurements using the IR camera. Although the measurements obtained using the IR camera had large errors, even after accounting for these errors, the upper limit of T_s is 5°C. Thus, it is shown that the Boussinesq approximation isn't violated.

3.3 Surfactant application

Natural bodies of water such as lakes and rivers contain a large amount of a variety of surfactants.[71] Tap water, which is obtained from such natural fresh water reserves contains some of these surfactants. Although tap water contains surfactants, the exact quantity and type are unknown and they are also liable to vary from day to day. This can result in inconsistent surface conditions and lack of reproducibility of experimental results. Thus, a foreign surfactant is applied to the water surface during experimentation. The added surfactant helped control the surface conditions by providing spatial and temporal consistency during an experiment and also over the entire period of experimentation.

The surfactant chosen for the experiments conducted for this thesis was oleyl alcohol. This choice was influenced by the low evaporation and dissolution rates of oleyl alcohol in water[80] thus causing lower film losses and more consistent surfactant coverage. The surfactant solution is prepared by dissolving one gram of oleyl alcohol in 500 mL of heptane, the heptane serving as a spreading agent for the highly viscous oleyl alcohol. The solution is stored in a flask tightly sealed with a glass stopper and covered with parafilm which prevents the solvent from evaporating. To apply this solution during a run, 40 μL of the stock solution is applied to the water surface in a protected region of the tank using a microsyringe as it prevents surfactant 'lenses', which are local agglomerations of the surfactant on the surface, from being blown over to the edge of the tank or over it by wind. Thus applying the surfactant in a protected region prevents premature loss of the surfactant film due to bleeding over the tank edge and effectively creates a reservoir of surfactant in the tank. This reservoir was a piece of Teflon tubing with a slit cut along its length, shown in Fig. 7, positioned in a corner of the tank farthest downstream and out of the field of view of the IR camera as shown in Fig. 8. The slit on the tube allows the deposited surfactant to seep out and replenish the surfactant lost from the water surface thus maintaining the

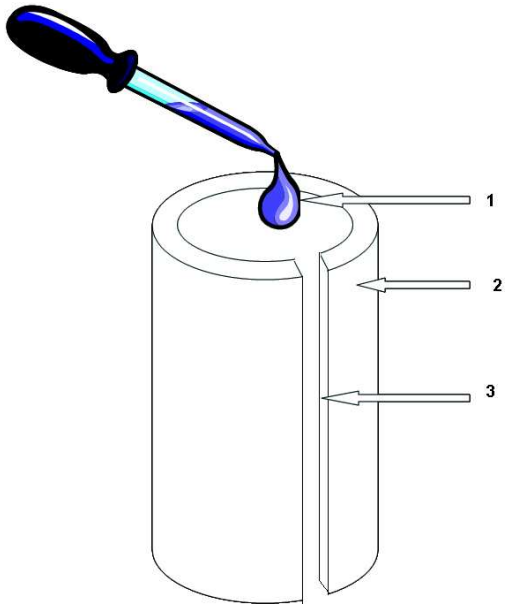

Figure 7: Surfactant reservoir: 1) Surfactant, 2) reservoir, 3) slit.

surfactant film on the water surface. The reservoir acts as a protected region where the surfactant is not affected by waves on the water surface and controls the surfactant supply to the water surface. Stated another way, this arrangement functioned as an automatic equilibrium mechanism in which the water surface draws out the required amount of surfactant to maintain a homogenous surfactant film.

In spite of the low evaporation and dissolution rates of oleyl alcohol,[80] the high operating temperatures, high wind velocities and lengthy duration of the experiments reported here cause considerable loss of the surfactant film. Thus, the surfactant film needs to be maintained by replenishing the reservoir. All the available research on surfactant loss rates concerns surfactant loss in the absence of wind, thus the amount of surfactant to be applied to the water surface and the replenishment rate was determined through trial and error. The surfactant concentration chosen was that which provides homogenous conditions throughout an experiment at the highest operating temperature and wind speed.

These trial and error experiments showed that for the worst possible scenario i.e.

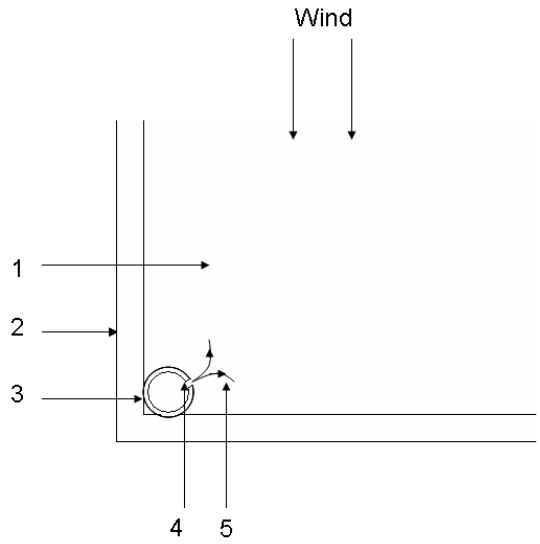

Figure 8: Top view of the water tank showing the position of the surfactant reservoir: 1) Water surface, 2) water tank, 3) surfactant reservoir, 4) slit in reservoir, 5) spreading surfactant.

water temperature of 41°C and wind velocity of 5 m/s, it is possible to maintain a homogenous surfactant film for a period of 30 minutes when 40 μL of the solution of oleyl alcohol in heptane is applied to the water surface. The homogeneity of the film is determined from the presence or absence of a Reynolds ridge[81] on the water surface. When an external shear, in the form of an air flow is induced on the water surface, the surfactant present on the water supports this shear to some extent. However, as this shear increases beyond a certain point, it causes the surfactant film to rupture thus forming what is known as a Reynolds ridge, which is the physical boundary between the surfactant free water surface and the surfactant covered water surface. This ridge is clearly evident in the IR imagery as a boundary separating the clean and surfactant-covered region of the water surface. An example is shown in Fig. 9 which is a grayscale image of the water surface taken using the IR camera, where a lighter shade indicates a higher temperature and a darker shade indicates a lower temperature. The direction of the wind over the water surface in this image is from the bottom to the top of the image, thus the wind is pushing against the top dark

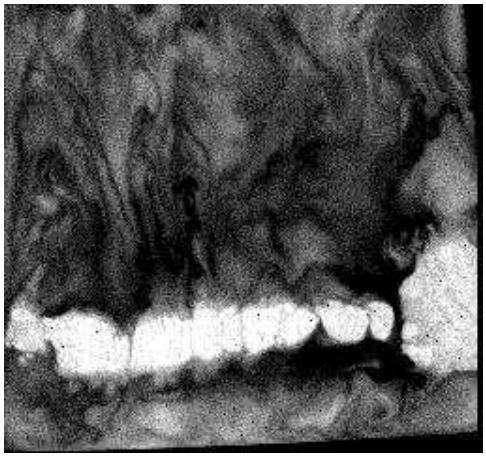

Figure 9: Image showing the Reynolds ridge. The lighter region is the clean one while the darker is the surfactant covered region. The black strips along the right and bottom edges are due to the plexiglas obstructing the view of the camera.

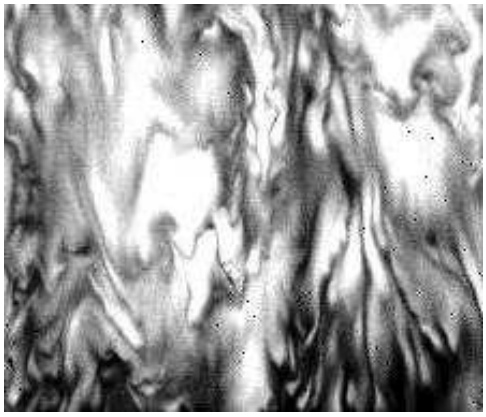

Figure 10: Image showing a homogeneous surfactant film

half of the image which shows the sheared and compressed surfactant film. The image covers an area that is a 0.24 m by 0.24 m square on the water surface in the center of the tank, this format being the same for all of the IR images presented here. The lighter region is the surfactant free or clean region whereas the dark region is the surfactant covered region. This image can be compared to Fig. 10 which shows a homogeneous surfactant film on the water surface.

During the initial set of trial experiments, 10 μL of oleyl alcohol stock solution is added to the surfactant reservoir. It was observed that this amount could not

hold a homogenous surfactant film for longer than 10 minutes after which a Reynolds ridge was formed. Hence in subsequent trial experiments this amount was steadily increased. These experiments revealed that 30 μL of stock solution resulted in a steady surfactant film for 35 minutes. To provide a margin of safety, the procedure adopted was adding 40 μL of surfactant every 30 minutes, thus ensuring the presence of a homogenous surfactant film on the water surface throughout the experiment. This procedure was used for all experiments presented herein.

After each run, the water surface was swiped with lab wipes and the water tank was thoroughly cleaned using methanol, thereby preventing any surfactant from being carried on to the next experiment. Thus consistent experimental conditions were maintained.

3.4 Data processing

Figure 11 shows typical time traces of the bulk air and water temperatures during an experiment at a wind speed of 4 m/s. As expected, the air temperature varies very little during an experiment, the maximum air temperature variation during a single experiment being typically 0.4°C. The bulk water time trace decays with time, the temperature range visible in this plot being the typical temperature range of an experimental run. Thus it can be seen that the bulk air temperature change compared to the bulk water temperature change is negligible. The bulk water temperature data points are plotted 5 minutes apart in time, the logging rate is one data value every 30 seconds and every tenth data point is shown on the plot. The same applies to Fig. 12 which shows the typical mass time trace obtained from the mass balance.

The overall goal of each experiment is to compute the dimensionless heat and mass transfer from the bulk water to the bulk air and relate it to the driving force behind the transport. In each case this involved taking the derivative of the temperature and mass time traces. To do this, the time traces of the bulk water, bulk air and mass were

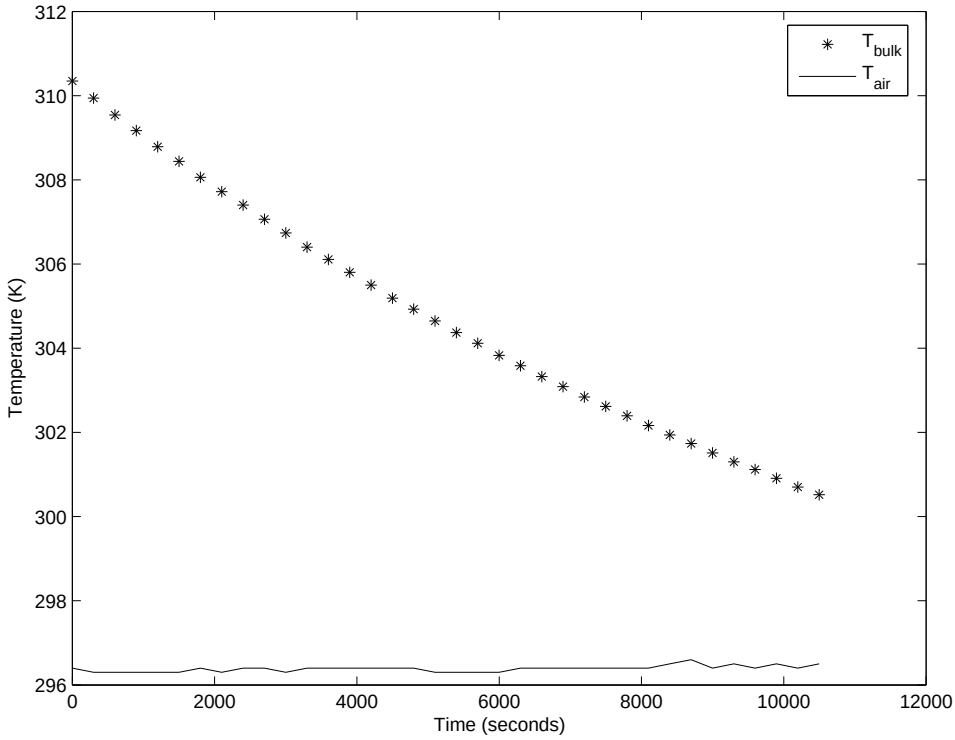

Figure 11: Typical water and air temperature time traces at 4 m/s wind speed.

first fit by calculating a least squares fit to the data using a fourth order polynomial model. The fourth order polynomial model was chosen after testing polynomial fits of orders 1 - 25 as it gave the best fit to the data that also correctly modeled the data.

The time rate of decay of the bulk water temperature, which was calculated from the derivative of the polynomial fit to the water temperature data gave the heat loss from water. This heat loss from the water is a sum of various components:

$$q = q_1 + q_2 + q_3 + q_4 \tag{60}$$

where the variables are the same as defined in Eq. (21). The tank wall heat loss was quantified by filling the water tank to the brim and covering all sides with insulation,

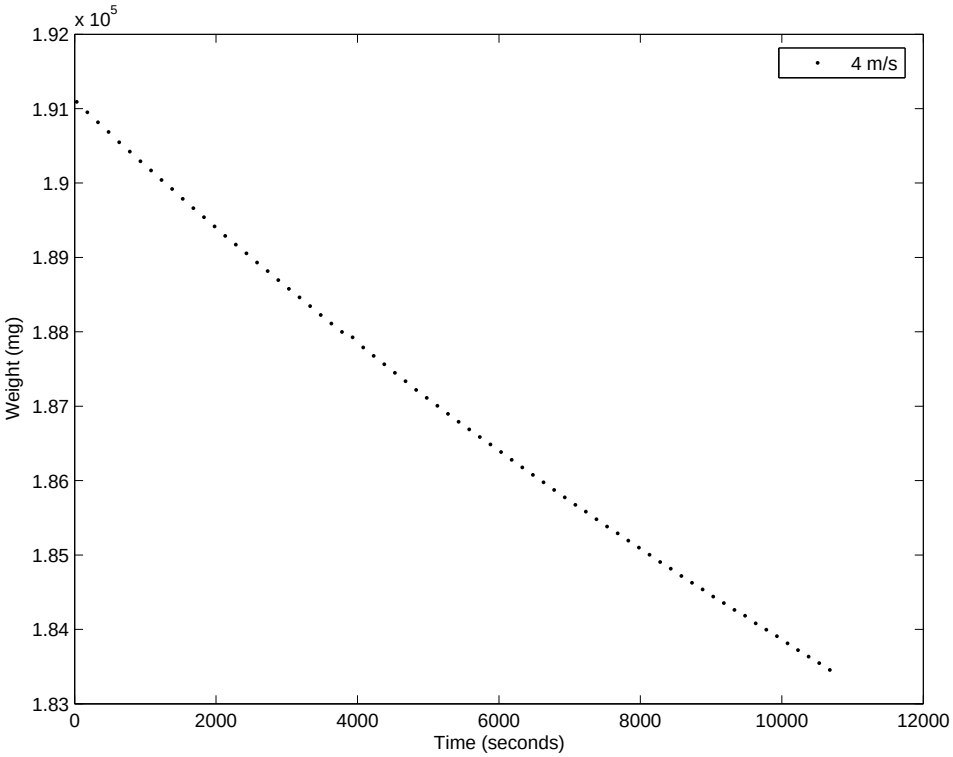

Figure 12: Typical mass loss time trace at 4 m/s wind speed.

including the top surface. The only possible mode of heat loss from the water in that case is due to conduction through the tank walls. The water was then allowed to cool and the temperature of water and the air surrounding the tank were recorded. The derivative of the bulk water time trace gave the rate of wall heat loss. This heat loss is calculated as:

$$q_4 = (m_1 C_{p_1} + m_2 C_{p_2}) \frac{dT_b}{dt} \tag{61}$$

where m_1 is the mass of water in the tank, m_2 the mass of the glass tank, C_{p_1} the specific heat of water and C_{p_2} the specific heat of glass. This heat loss from the tank is only due to conduction, driven by the temperature difference between the water and air on either side of the insulation and dependent on the properties of the insulation. This wall heat loss is then plotted against the gross temperature difference and the following linear fit to the data is obtained:

$$q_{4c} = 1.127(T_b - T_a) + 2.5163 \cdot 10^{-14} \tag{62}$$

where q_{4c} is the heat loss during a closed top experiment. The closed top experiment thus provided an estimate of the wall heat loss for particular values of ΔT_g, this loss being 9-10% of the total heat loss from the water for experiments at the lowest wind speed i.e 0 m/s. This percentage further decreased as the wind speed increased and was accurately accounted for. This heat loss is dependent only on the insulation around the tank, the insulated surface area and the temperature difference between the water bulk and the ambient air temperature, thus the absolute loss would remain the same irrespective of the wind speed, relative humidity or any other factors.

The heat loss from this experiment is the wall heat loss from the entire surface area of the tank. Since during a regular open top experimental run, the top surface of the tank was not insulated, the wall heat loss during an experiment will be different from that obtained from the closed top run. This loss was obtained by multiplying the total heat loss by a correction factor which is a ratio of the tank surface area insulated during an experiment, A_i, to the total tank surface area during a closed top experiment A_c as:

$$c_1 = \frac{A_i}{A_c} = 0.87 \tag{63}$$

where c_1 is the correction factor to be applied. The correction is:

$$q_4 = c_1 \cdot q_{4c} \tag{64}$$

The derivative of the mass time trace gave the rate of mass loss from the water surface in mg/s and its product with the latent heat of vaporization gave the heat lost due to evaporation:

$$q_2 = \frac{dm}{dt} \cdot h_{fg} \tag{65}$$

This contribution of heat loss due to evaporation is deducted from the overall heat loss from water to air obtained from the decay of the bulk temperature time trace as shown in Eq. (60). This was done to obtain the convective component of the heat transfer.

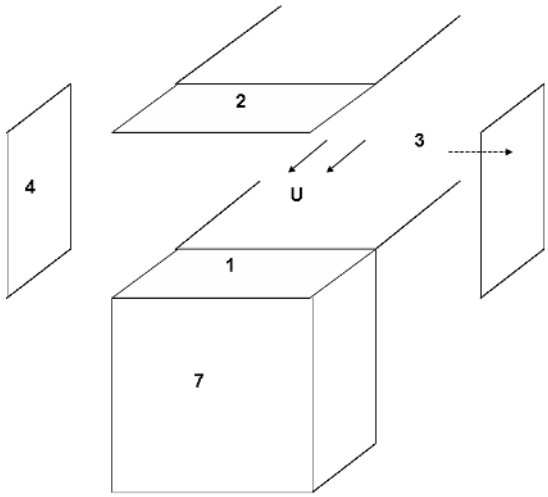

Figure 13: Surfaces for calculating radiation emission from water. Surfaces 2-4 are Plexiglas, surface 1 is the water whereas surfaces 5 and 6 which are the lab wall and the blower interior wall respectively are not shown here. The water tank is labeled 7.

The radiative heat transfer between the water surface and the surroundings also needs to be accounted for. Figure 13 shows the different surfaces of the test section from which the radiative heat loss was calculated. All surfaces of the enclosure were assumed to be diffuse and gray as well as the lab and blower walls which exchange heat with the water surface. The Plexiglas surfaces are numbered 2 to 4, surface 1 is the water surface whereas surfaces 5 and 6, which are the lab wall facing the wind tunnel exit and the blower interior respectively, are not depicted in this figure.

The emissivities of water, Plexiglas, lab walls (brick) and the blower interior (sheet metal) were taken from the Handbook of Chemistry and Physics[82] and are shown in Table 3. The form factors for this geometry which were calculated based on methods presented in Incropera and Dewitt,[1] as well as the areas of the different surfaces are shown in Table 4. The net radiation from surface 1 was determined as:

$$q_4 = \sum_{j=1}^{6} A_1 F_{1j} (J_1 - J_j) \tag{66}$$

Table 3: Emissivities of the different radiating surfaces.[82]

Material	Emissivity
Water	0.97
Plexiglas (0.5")	0.9
Brick	0.93
Sheet metal	0.7

Table 4: Areas and form factors used in Eqs. (66) and (67).

Surface	Form factors	Area (m^2)
1	F_{12}= 0.15, F_{13}, F_{14} = 0.225, F_{15}=0.4, F_{16} = 0.3	0.068
2	F_{21} = 0.15, F_{24} = 0.225; F_{25} = 0.4, F_{26} = 0.3, F_{23}=0.4	0.068
3	F_{34} = 0.21, F_{32}, F_{31} = 0.19, F_{35} = 0.45, F_{36} = 0.31	0.078
4	F_{43} = 0.21, F_{45} = 0.45, F_{46} = 0.31, F_{41}, F_{42} = 0.19	0.078
5	F_{51}, F_{52} = 0.16, F_{53}, F_{54} = 0.19, F_{56} = 0.4 = 0.3	4
6	F_{65} = 0.4, F_{64}, F_{62} = 0.225, F_{61} = 0.4, F_{63} = 0.21	0.0837

where F_{1j} is the view factor for surface 1, J the radiosity for a surface and ϵ_1 is the emissivity of the water surface. Subscript j denotes the receiving surface. All the variables on the right side of Eq. (66) are known except for the surface radiosities. The problem involves solving for the radiosities of the five surfaces exchanging heat with the water surface simultaneously, thus the radiosities for each can be obtained by solving the set of simultaneous equations obtained from:

$$\frac{E_{b1} - J_1}{(1-\epsilon_1)/\epsilon_1 A_1} = \sum_{j=1}^{5} A_1 F_{1j}(J_1 - J_j) \tag{67}$$

where E_{b1} is the emissive heat transfer from the water surface, i is the emitting surface and i and j will have different values depending on the surface under consideration. Using the radiosity from surface 1 obtained on solving Eq. (67), the total radiative

heat flux from this surface was obtained from Eq. (66).

This loss due to the net radiative heat transfer was found to be 0.98% of the total heat loss from the water surface. Once the contributions due to the evaporative loss, radiative loss and wall heat loss were deducted from the total heat lost from the bulk water as shown in Eq. (60), the resulting heat loss was solely due to the convective heat transfer between the bulk water and the bulk air, the driving mechanism behind this heat transfer being the temperature difference between them.

The heat loss due to convective heat transfer was thus calculated as:

$$q_1 = q - q_2 - q_3 - q_4 \tag{68}$$

Using this convective heat loss from the water to air, the heat transfer coefficient and the Nusselt number were calculated as:

$$h_t = \frac{q_1''}{\Delta T} \tag{69}$$

$$Nu = \frac{h_t L}{k} \tag{70}$$

where q_1'' is the heat flux only due to convective heat transfer and ΔT is the gross temperature difference between the bulk water and air. Since natural and forced convection are being studied, L can be the height of the air column, the length of the water tank or the depth of the water tank. This characteristic dimension for studying natural and forced convection will be chosen based on the nature of the flow governing the transport process. For the case of natural convection it has been

shown[83,84] that the breadth of the fluid body is the controlling dimension as it controls the formation of the buoyant plume whereas for Rayleigh-Bénard convection the depth of the fluid medium is used. For forced flow over a flat plate past researchers[32,33] have traditionally used the length of the fluid medium as the characteristic dimension. For the case of the transport process studied here, it will be shown in Section 4.2 that the air side of the interface controls transport. Thus, as the water tank is enclosed within a wind tunnel, the height of the air column above the water tank was used as the characteristic length scale for Ra, Sh and Nu. Using the temperature data for water and air, the Rayleigh number for heat transfer was calculated:

$$Ra = \frac{\beta g \Delta T L^3}{\nu \alpha} \tag{71}$$

These non-dimensional quantities, i.e. Nu, Re and Ra were then related as described in Section 1.3, and a similar methodology was followed to relate Sh to Ra and Re. The Reynolds number was calculated as:

$$Re = \frac{U L_u}{\nu} \tag{72}$$

where L_u was the characteristic length scale for Re. The geometry of the setup for this study i.e. water tank placed in a wind tunnel, resembles that of a flat plate with an unheated starting length, thus the length of the entire wind/water tunnel was chosen as the length scale for calculating Re. These $Nu(Ra, Re)$ and $Sh(Ra, Re)$ relationships thus obtained are presented and analyzed in detail in Section 4.

The power law relationships obtained in this work, for example the $Nu(Ra)$ relationship were obtained by first casting these equations in the logarithmic form:

$$Nu = ARa^b \tag{73}$$

$$\log_{10}(Nu) = (\log_{10} A) + (b \cdot \log_{10} Ra) \tag{74}$$

Thus, obtaining a linear fit to $\log(Nu)$ versus $\log(Ra)$ effectively fits a power law relationship to the $Nu(Ra)$ data. The natural convection $Sh(Ra)$ relationship and the forced convection $Nu(Re)$ and $Sh(Re)$ relationships are fit similarly.

3.5 Uncertainty analysis

The uncertainties in the results presented here are due to the instrumental uncertainties and the uncertainties introduced in the calculations due to the processing method employed. The rules of uncertainty propagation were used to estimate the uncertainty in the final results presented due to these sources.[85,86] Another source of uncertainty in the results is that which comes from the scatter in the data. This uncertainty can be quantified by calculating the confidence interval for the results presented using the students T distribution and by calculating the standard deviation of the data from the fit to it. This uncertainty will be quantified in Section 4.

The rules of error propagation were used to ascertain the accuracy of the results presented here. These rules state that if a quantity R is calculated by adding or subtracting two different terms M and N, each having a certain uncertainty associated with it, then the uncertainty in the calculated value of R given by the quadrature rule is:

$$R_e = \sqrt{(M_e^2 + N_e^2)} \tag{75}$$

where the subscript 'e' denotes the uncertainty in the measurement of the quantity. This rule is valid if M and N are independent quantities e.g. the total uncertainty in the measurement of ΔT_g is obtained from the uncertainties in the measurement of T_b and T_a as both are measured using different thermistors and are thus independent. If M and N are dependent then the total uncertainty in R is:

$$R_e = M_e + N_e \tag{76}$$

For example, the total uncertainty in any quantity that is obtained by combining measurements made by the same instrument. If R is calculated by multiplying or dividing two different quantities, the uncertainty in R which is calculated as the sum of the fractional uncertainties in M and N is:

$$R_e = \frac{M_e}{|M|} + \frac{N_e}{|N|} \tag{77}$$

The final rule states that the uncertainty in the n^{th} order derivative of a quantity is of an order equal to the n^{th} power of the period 'h' between successive measurements of that quantity:

$$R = \frac{d}{dt}(M) \tag{78}$$

$$R_e = \theta(h^n) \tag{79}$$

$$h = M_{i+1} - M_i \tag{80}$$

where θ denotes the order of magnitude, i denotes the data point number and n denotes the order of the polynomial used to fit the data.

The total uncertainty in measurements made by the temperature probes, thermohygrometer and anemometer, were calculated using the quadrature rule[85] for additive errors shown in Eq. (75). The total uncertainty in measurements made by each instrument was calculated by using the additive rule to combine the uncertainty in each component of the particular instrument as:

$$\Delta E_1 = [(\Delta e_1)^2 + (\Delta e_2)^2]^{1/2} \tag{81}$$

$$\Delta E_2 = [(\Delta e_3)^2 + (\Delta e_4)^2]^{1/2} \tag{82}$$

$$\Delta E_3 = [(\Delta e_5)^2 + (\Delta e_6)^2]^{1/2} \tag{83}$$

where ΔE_1 is the total uncertainty in measurements made by the thermistor setup, ΔE_2 is the total uncertainty in measurements made by the thermohygrometer and

Table 5: Instrumental uncertainties.

Component	Source	Uncertainty
Δe_1	Thermistor meter	$\pm 0.01^{\circ}$C
Δe_2	Thermistor probes	$\pm 0.01^{\circ}$C
ΔE_1	Air/water temperature measurement	$\pm 0.014^{\circ}$C
Δe_3	RH meter accuracy	$\pm 1\%$
Δe_4	RH probe accuracy	$\pm 1\%$
ΔE_2	Relative humidity measurement	$\pm 1.4\%$
Δe_5	Anemometer accuracy	± 0.01m/s
Δe_6	Anemometer probe accuracy	± 0.01m/s
ΔE_3	Velocity measurement	± 0.014m/s

ΔE_3 is the total uncertainty in measurements made by the anemometer. Here, Δe_1 is the uncertainty in the thermistor meter, Δe_2 is the uncertainty in the thermistor probe, Δe_3 is the uncertainty in the thermohygrometer, Δe_4 is the uncertainty in the thermohygrometer probe, Δe_5 is the uncertainty in the anemometer and Δe_6 is the uncertainty in the anemometer probe. The total uncertainty in measurements made by each component of a particular instrument i.e. Δe_1 through Δe_6 were obtained by combining the random uncertainty and the systematic uncertainty in that component using the additive rule of uncertainty analysis.

These individual uncertainties along with the uncertainty of each measurement are listed in Table 5. The thermistor had a resolution viz. random uncertainty of 0.001°C and a systematic uncertainty of 0.011°C while the thermohygrometer had a random uncertainty of 0.1% and a systematic uncertainty of $\pm$ 1.4% when measuring the relative humidity. The source of the instrument accuracies, repeatabilities and resolutions was the respective manufacturer's product specifications manual. The rules of error propagation stated above are explained in detail by Taylor[85] and Figliola and Beasley.[86]

Table 6 shows the uncertainties in the different measurements. These uncertainties propagate through the various calculations done to obtain the required dimensionless quantities and will also be quantified using the rules of error propagation defined

Table 6: Uncertainty propagation in Nu.

Quantity	Source	Systematic uncertainty	Random uncertainty(fit)	Total uncertainty
T_b	Thermistor	±0.014°C	0.015°C	0.018°C
T_a	Thermistor	±0.014°C	0.015°C	0.018°C
ΔT_g	Thermistor	NA	NA	0.028°C
m_w	Mg balance	±0.11mg	8 mg	8.23 mg
$\frac{dT_b}{dt}$	Poly. fit	NA	NA	0.014 °C/s
$\frac{dM}{dt}$	Poly. fit	NA	NA	0.018 mg/s
A	Ruler	±1mm	NA	±1.4mm^2
L	Ruler	±1mm	NA	±1mm
m_g	Ruler	±1mm	NA	13 mg
C_{pw}	Thermistor	±0.02°C	NA	18 KJ/kgK
C_{pg}	Thermistor	±0.02°C	NA	8.4 KJ/kgK

above. The aim here is to ascertain the total uncertainty in the final measurement of Nu, Ra, Sh and Re, thus the propagation of uncertainties from the initial measurement of the raw data to the final expression of the Nu, Ra, Sh and Re must be calculated. The uncertainties in the measured quantities are expressed in terms of their absolute values in Table 5. Thus, as Nu, Ra, Sh and Re are calculated from ΔT, $\frac{dT_b}{dt}$, $\frac{dM}{dt}$ and U the uncertainties in these quantities are combined using the rules of error propagation shown above to get the errors in Nu, Ra, Sh and Re. The following is a sample calculation for the total uncertainty in Nu:

$$Nu = \frac{(m_w C_{pw} + m_g C_{pg}) \cdot \frac{dT_b}{dt} \cdot L}{A \cdot k \cdot \Delta T} - (h_{fg} \cdot \frac{dM}{dt}) - (1.127(\Delta T_g) + 2.5163 \cdot 10^{-14}) \quad (84)$$

In Eq. (84), where two quantities are multiplied the multiplicative rule of error propagation is used. Where a derivative is calculated, the derivative rule for error propagation is used. Thus the different uncertainties are combined to give the final uncertainty in Nu, the total uncertainty in Nu being due to the uncertainties in its individual terms. Table 6 shows the uncertainties in the measured quantities and also their source.

Using these rules defined in Eqs. (75) - (77) and the equations defining the dimensionless quantities in Section 1, the total uncertainties in the Nusselt, Sherwood, Rayleigh and Reynolds numbers were found to be ± 34.62 units, ± 0.19 units, $\pm 4.8 \times 10^5$ units and $\pm 2 \times 10^3$ units respectively within a 95% confidence interval. These translate into a percentage uncertainty of $\pm 7.8\%$, $\pm 4.9\%$, $\pm 1.8\%$ and $\pm 1.3\%$ in Nu, Sh, Ra and Re for experiments at 0 m/s where the percentage will be largest.

4 RESULTS

The results presented here are subdivided into two sections; $Nu(Ra, Re)$ relationships and $Sh(Ra, Re)$ relationships. The experimental results are preceded by a discussion about the significance of a few experimental and data processing techniques which were implemented to ensure greater accuracy of the presented results.

4.1 Significance of Ra versus $Nu \cdot Ra$ and $Sh \cdot Ra$

The propagation of errors was discussed in Section 3.5 and it was shown that the Nusselt, Rayleigh, Sherwood and Reynolds numbers have errors of ± 34.62 units, ± 0.19 units, $\pm 4.8 \times 10^5$ units and $\pm 2 \times 10^3$ units respectively. Though these errors are not large and it is not possible to completely eliminate all errors, it is desirable to reduce them further. The largest part of these errors comes from calculating the temperature difference driving natural convection based on the polynomial fits of the bulk air and water temperatures. This ΔT term is in the denominators of Nu and Sh and the numerator of Ra. Thus an uncertainty in ΔT creates opposite errors in Nu and Sh and Ra i.e. if the uncertainty in ΔT is positive, Nu and Sh will be overestimated while Ra will be underestimated. This magnifies errors in the $Nu(Ra)$ and $Sh(Ra)$ relationships. The ΔT term affects Sh as the density gradient driving mass transfer is calculated from it.

Globe and Dropkin[3] reduced this uncertainty by plotting the product of $Nu \cdot Ra$ against Ra instead of plotting Nu versus Ra to get the functional relationship between these two groups. This reduces errors because the ΔT terms in the numerator of Ra and the denominator of Nu cancel, making $Nu \cdot Ra$ a quantity derived only from the fluid's thermophysical properties and the convective heat flux:

$$NuRa = \frac{q_c \beta g L^4}{\nu \kappa^2} \tag{85}$$

Thus the errors due to the ΔT term are eliminated in the $Nu \cdot Ra$ term. Similarly, when the product $Sh \cdot Ra$ is plotted against Ra, errors present in Sh from the ΔT term used to calculate the density gradient driving evaporation are eliminated.

The method of fitting a power law to the $Nu(Ra)$ and $Sh(Ra)$ data was described in Section 3.4. This was done by fitting a line to the logarithms of the respective quantities and extracting the exponent and prefactor of the power law from the slope and intercept of the linear fit. When plotting $Nu \cdot Ra$ versus Ra and $Sh \cdot Ra$ versus Ra the power law fit changes to:

$$Nu \cdot Ra = MRa^n \tag{86}$$

where M and n are the exponent and prefactor of the power law relationship between $Nu \cdot Ra$ and Ra. On taking the log of both sides of Eq. (86) this relationship becomes:

$$\log_{10}(Nu \cdot Ra) = \log_{10}(MRa^n) \tag{87}$$

$$\log_{10}(Nu) + \log_{10}(Ra) = (\log_{10} M) + (n \cdot \log_{10} Ra) \tag{88}$$

Comparing the above equation to Eq. (74) we obtain:

$$A = M \tag{89}$$

$$b = n - 1 \tag{90}$$

Thus, using the modified power law fit, the exponent of the $Nu(Ra)$ power law fit can be obtained by subtracting 1 from the slope of the linear fit to the $\log(Nu \cdot Ra)$ versus $\log(Ra)$ data. This same procedure can be followed for the $Sh(Ra)$ relationship. The exponents and prefactors for all $Nu(Ra)$ and $Sh(Ra)$ power law relationships presented in this thesis are obtained in this way.

The $Nu(Ra)$ and $Sh(Ra)$ relationships for pure natural convection can be adequately modeled using a power law fit. However for data obtained at a fixed wind speed this approach fails since Nu will have a finite value as Ra approaches zero. Thus, for all wind speeds greater than 0 m/s, a linear fit of the $Nu(Ra)$ relationship was obtained as it provided the best fit to the data which was also physically plausible. To model this linear fit of the $Nu(Ra)$ data, the following approach was used:

$$Nu \cdot Ra = M_1 Ra^2 + M_2 Ra + M_3 \tag{91}$$

where M_1, M_2 and M_3 are coefficients of the quadratic relationship between $Nu \cdot Ra$ and Ra. M_3 is specified to be equal to zero in Eq. (91) while fitting a quadratic equation to the $Nu \cdot Ra$ values. The $Nu \cdot Ra(Ra)$ relationship was modeled instead of $Nu(Ra)$ to reduce errors due to the ΔT term, the aim being to extract a linear

$Nu(Ra)$ relationship from this quadratic $Nu \cdot Ra(Ra)$ model. This equation can be transformed into an $Nu(Ra)$ relationship by dividing both sides of Eq. (91) by Ra, giving:

$$Nu = M_1 Ra + M_2 \tag{92}$$

Thus a linear relationship between Nu and Ra for wind speeds greater than zero is obtained. The $Nu(Ra)$ linear fits for forced convection and power law fits for zero wind speed are presented and discussed in Section 4.4.

4.2 Heat and mass transfer resistance

Thermal resistance is defined as the ratio of the temperature difference, ΔT, to the heat transferred q. Thus, convection heat transfer resistance is:

$$R_h = \frac{\Delta T}{q_c} \tag{93}$$

where R_h is the convection heat transfer resistance and q_c is the convective heat transfer. The ratio of the convective heat flux to the driving temperature difference is the heat transfer coefficient, thus R_h can also be defined as:

$$R_h = \frac{1}{h_t \cdot A} \tag{94}$$

where A is the area over which heat transfer takes place. For the case of an air-water interface, R_h can be used to estimate the heat transfer resistances on both sides of the interface. If one side has a significantly higher heat transfer resistance than the other, then this side controls the heat transfer, in effect acting as a bottleneck for heat transfer. For the air-water interface, the resistances on both sides of the interface are:

$$R_a = \frac{\Delta T_a}{q_c''} \tag{95}$$

$$R_w = \frac{\Delta T_w}{q_c''} \tag{96}$$

where R_w and R_a are the heat transfer resistances on the water and air side of the interface respectively. Due to conservation of energy, the convective heat flux q_c'' on both sides of the interface is the same. For the experiments conducted for this thesis ΔT_a was never less than 6 °C, and ranged from 7.0 °C to 15 °C whereas it is also known that ΔT_w typically has a value between 2 to 5°C.[79,87] The heat transfer resistance on the air side of the interface was therefore always greater for these experiments and thus the air side controlled the heat transfer.

Similarly, the maximum and only possible resistance to mass transfer is provided by the air side as water faces no resistance to transfer in water. The only exception to this would be if the resistance to heat transfer in water is greater than the resistance to mass transfer, as the energy for evaporation is provided by the bulk water which dissipates heat to the surface and drives evaporation. Thus comparing the mass transfer resistance on the air side to the heat transfer resistance on the water side it was found that:

$$R_m = \frac{1}{h_m \cdot A} > R_w \tag{97}$$

where R_m is the resistance to mass transfer on the air side. Thus, as the air side of the interface controls the maximum possible heat and mass transfer from the water to air, all non-dimensional relationships ($Nu(Ra)$, $Nu(Re)$, $Sh(Ra)$, $Sh(Re)$, $Nu(Ra, Re)$ and $Sh(Ra, Re)$) will be calculated for the air side of the interface.

4.3 Prandtl and Schmidt number variations

The equations governing natural and forced convective heat and mass transfer have been described in Sections 1 and 3. It can be seen from these equations that Nu and Sh are functions of Pr and Sc of a fluid respectively, just as they are each functions of Ra and Re. However, the effect of Pr and Sc on Nu and Sh has been ignored in the research done for this thesis as the air temperature range for the experiments conducted for this thesis was too small to cause a large change in Pr and Sc. During a typical experiment, Pr for air changed by approximately 1.24% while Sc for air changed by approximately 1.4%. These values were calculated based on the air temperature change at the water surface in comparison with the free stream as this will be the maximum air temperature fluctuation possible and thus the worst case possible for Pr and Sc change. The standard deviation of the Prandtl and Schmidt number from the mean was calculated to be 0.11% of its absolute value.

4.4 $Nu(Ra, Re)$ relationships

To summarize the methodology used to obtain Nu, Ra and Sh, the first step involved actual measurement of bulk air and water temperatures and the mass flux rate. This raw data was fit using suitable polynomial functions and these polynomial functions were then used to calculate the various dimensionless quantities i.e. Nu, Ra and Sh. The $Nu(Ra)$ and $Sh(Ra)$ plots obtained from these calculated values were subsequently fit as well to obtain physically meaningful relationships between them. The various non-dimensional quantities are calculated for the air side of the interface and using the gross temperature difference between the bulk water and air as explained in Sections 1.6 and 4.2.

Figure 14 is a plot of Nu versus Ra for the entire range of wind speeds explored for the research presented here, five experimental runs being conducted at each wind speed. This plot shows the results obtained by calculating Nu and Ra from the fitted

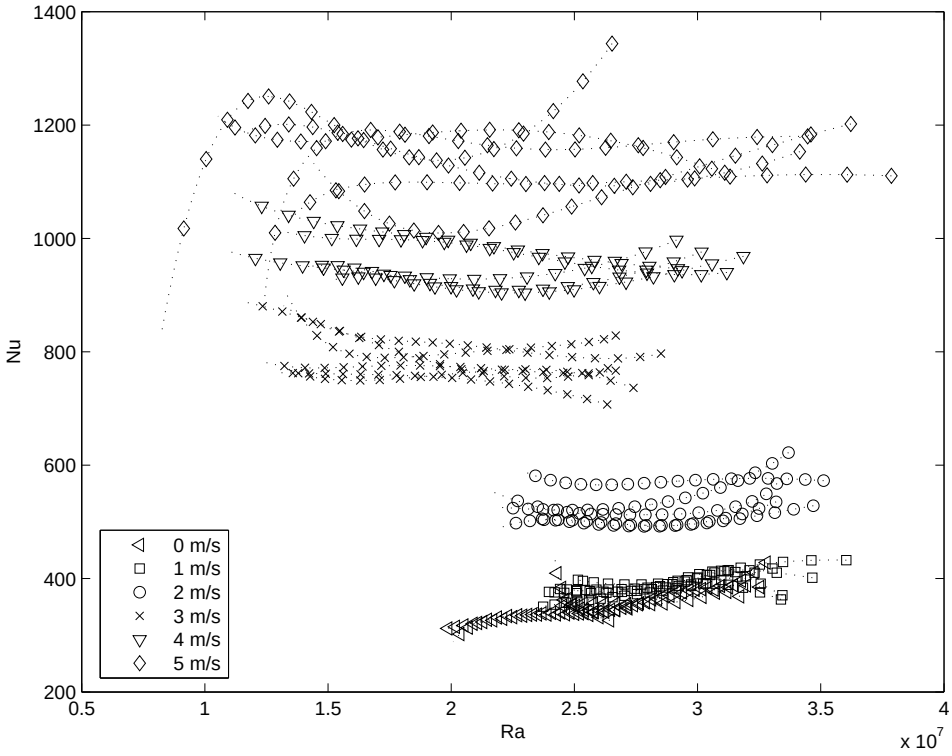

Figure 14: Plot of Nu versus Ra for all wind speeds.

raw data, thus the dotted lines are obtained from the polynomial functions which were used to fit the raw temperature and mass data. Each dotted line represents an experiment conducted at the wind speed indicated by the symbols on that dotted line. For each experiment, the symbols are spaced 10 minutes apart. The gap in the symbols is used to facilitate viewing the closely grouped lines, while still differentiating experiments at different wind speeds.

It is evident from Fig. 14 that Nu increases with increasing wind speed as expected. It is also evident that Nu increases with Ra at the lower wind speeds, however this trend reverses for wind speeds greater than 2 m/s. At a wind speed of 5 m/s Nu is essentially constant for all Ra, and thus forced convection dominated.

The functional form fitted to the $Nu(Ra)$ relationships at each wind speed has been explained in Section 4.1. Figure 15 shows the fits thus obtained for each individual wind speed plotted on linear coordinates along with the actual $Nu(Ra)$ values.

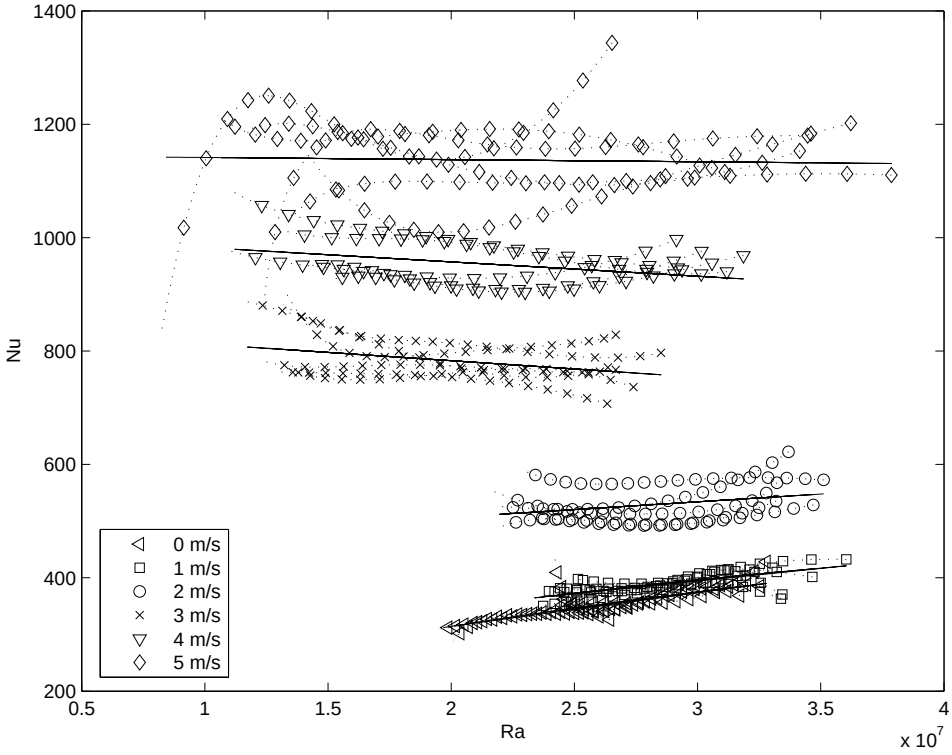

Figure 15: Plot of Nu versus Ra for all wind speeds with the fit for each wind speed superimposed. Symbols and dotted line show the fit data and solid lines show the fit.

Table 7: A table of the exponent (b), prefactor (A), slopes (M_1), and intercepts (M_2) of the $Nu(Ra)$ fits and the standard deviations in each.

Wind speed (m/s)	b ± S.D.	M_1 ± S.D.	A ± S.D.	M_2 ± S.D.
0	0.37±0.05	-	0.67±0.03	-
1	-	$4.6 \times 10^{-6} \pm 0.3 \times 10^{-6}$	-	341.7±56
2	-	$3.3 \times 10^{-6} \pm 2.3 \times 10^{-7}$	-	522.2±74.3
3	-	$-4.7 \times 10^{-6} \pm 3.0 \times 10^{-6}$	-	1009.4±108.2
4	-	$-1.5 \times 10^{-7} \pm 0.8 \times 10^{-7}$	-	1203.1±121.1
5	-	$1.3 \times 10^{-6} \pm 0.8 \times 10^{-6}$	-	1401±183

The dotted lines with symbols show the values calculated from the fit data and the solid lines show the best fit to the data at each particular wind speed. The observations previously presented regarding the $Nu(Ra)$ trends are confirmed here and an uncertainty analysis is presented later in Section 5. The quality of the fit and the scatter in the data, which is denoted by the standard deviation (S.D.) in the functional constants is shown in Table 7. The functional constants at each wind speed are obtained from the linear fits to the $Nu(Ra)$ values at each wind speed. It can be seen that the scatter in the experimental data, reflected by the high standard deviation values, generally increases as the wind speed increases. This points to the increasing difficulty in maintaining a consistent surfactant film during experiments at the higher wind speeds.

It was discussed in Section 3.4 that the fits obtained from Fig. 14 are liable to contain errors due to the ΔT term in Nu and Ra and thus cannot be used to extract accurate $Nu(Ra)$ relationships. Thus, as discussed before the $Nu \cdot Ra(Ra)$ plot was used to obtain all $Nu(Ra)$ relationships and the fits thus obtained are replotted on the linear scale in Fig. 15. Figure 16 shows a plot of the original $\log(Nu \cdot Ra)$ versus $\log(Ra)$ for all wind speeds. It can be seen from this plot that the undulations present in Fig. 14 have been eliminated to a large extent in Fig. 16. Though this plot is difficult to interpret and doesn't provide an intuitive understanding of the $Nu(Ra)$

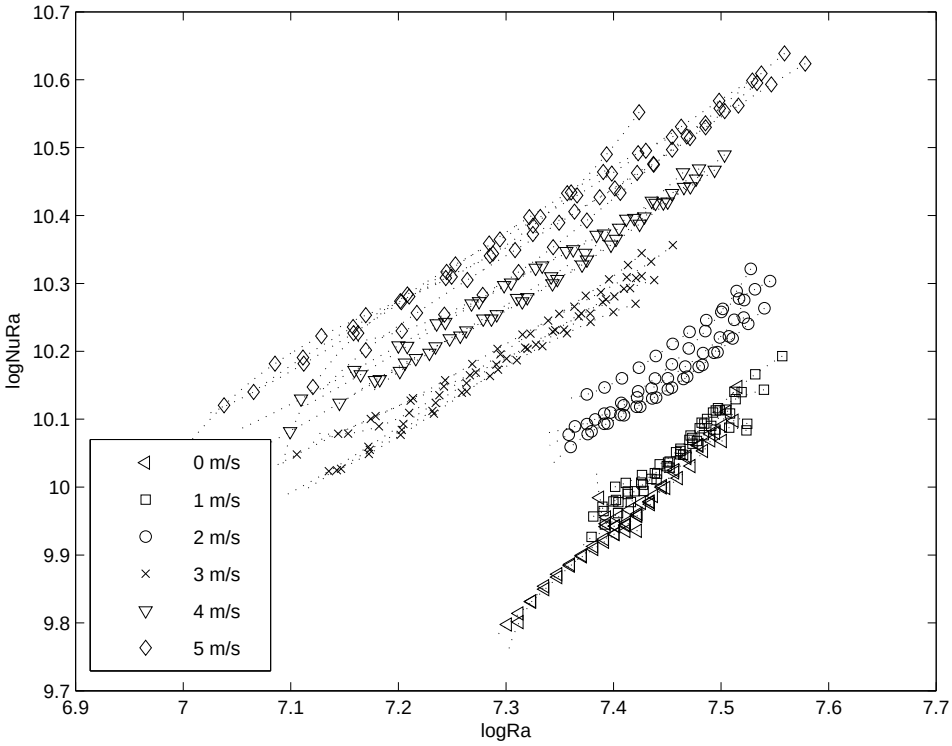

Figure 16: Plot of $\log(NuRa)$ versus $\log(Ra)$ for all wind speeds.

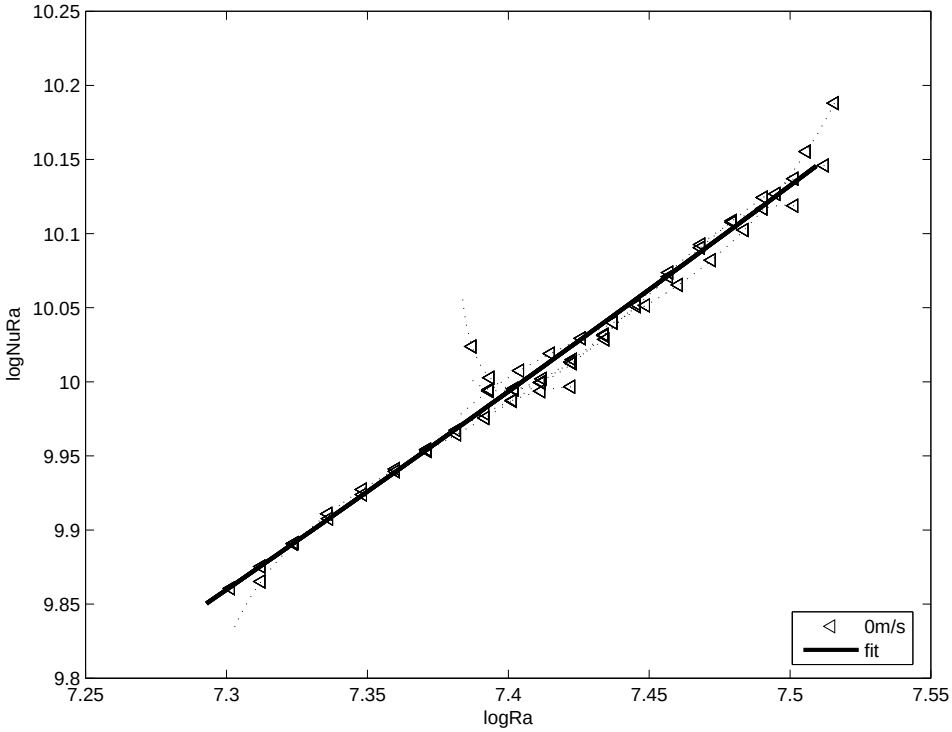

Figure 17: Plot of $\log(NuRa)$ versus $\log(Ra)$ at 0 m/s.

behavior, it is a much better tool to obtain $Nu(Ra)$ relationships as described in Section 4.1. Thus, all $Nu(Ra)$ relationships at each wind speed will be obtained from and be graphically presented in this form i.e. $\log(Ra)$ versus $\log(Nu \cdot Ra)$ and such a plot will be referred to as the LNR plot.

Figure 17 shows the LNR plot for 0 m/s and the power law fit to it and this fit defines the $Nu(Ra)$ relationship for pure natural convective conditions. The solid line shows the power law fit to the $Nu(Ra)$ data whereas the dotted lines show the LNR plot of the fits obtained from the experimental data at the wind speed indicated by the symbol. The $Nu(Ra)$ relationship obtained at this wind speed is:

$$Nu_n = 0.67(Ra)^{0.37} \tag{98}$$

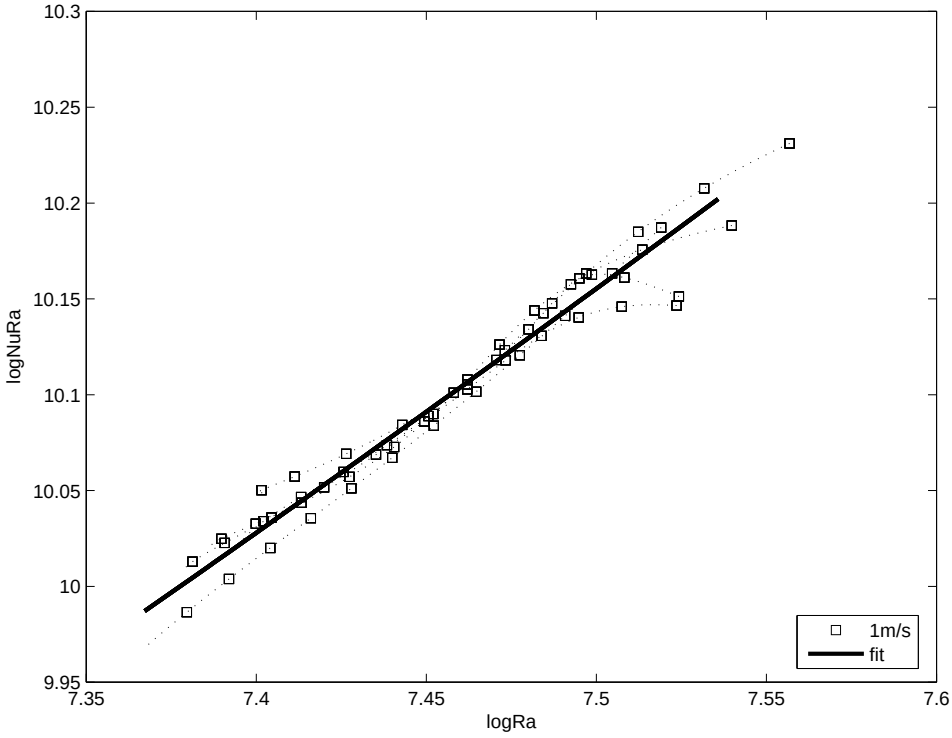

Figure 18: Plot of $\log(NuRa)$ versus $\log(Ra)$ at 1 m/s.

The exponent of the power law, $b = 0.37$ is slightly more than the classic $\frac{1}{3}$ power law for natural convection.

While the power law was used to fit the natural convection runs, a linear $Nu(Ra)$ model was used for runs having a forced convection component. The resulting $Nu(Ra)$ relationships obtained at different wind speeds are plotted in Figs. 18 - 22, which are LNR plots for the different wind speeds, and presented in Table 8. Here, the $Nu(Ra)$ relationships were obtained by getting a best fit to the $Nu \cdot Ra(Ra)$ data. These relationships define the $Nu(Ra)$ behavior for all wind speeds. The statistical significance of these relationships is shown in Table 9 which shows the 95% confidence interval of the fitting constants at each wind speed. The significance of these constants and inferences drawn from them will be discussed in Section 5. The table also shows the values of the comparative term G which was introduced in a bid to identify the transport regime present during experimentation.

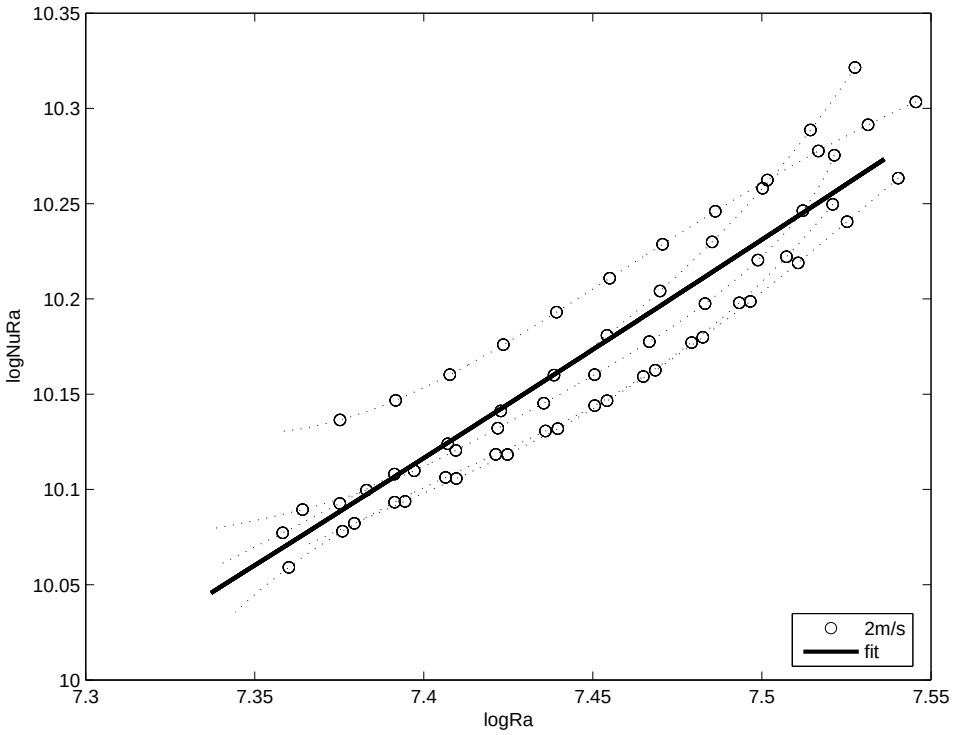

Figure 19: Plot of $\log(NuRa)$ versus $\log(Ra)$ at 2 m/s.

Table 8: $Nu(Ra)$ relationships for all wind speeds

Wind speed (m/s)	$Nu = f(Ra)$	G
0	$Nu = 0.67(Ra^{0.37})$	∞
1	$Nu = (4.6 \times 10^{-6})Ra + 341.7$	0.03
2	$Nu = (3.3 \times 10^{-6})Ra + 522.2$	0.001
3	$Nu = (-4.7 \times 10^{-6})Ra + 1009.4$	0.0001
4	$Nu = (-1.5 \times 10^{-7})Ra + 1203.1$	0.00006
5	$Nu = (1.3 \times 10^{-6})Ra + 1401$	0.000004

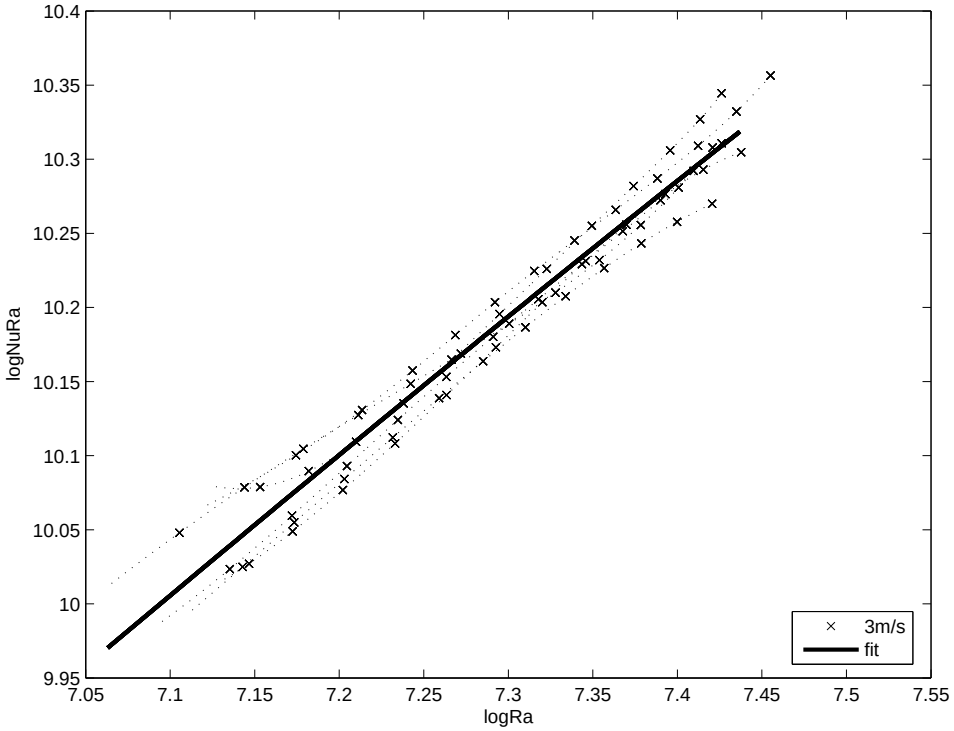

Figure 20: Plot of $\log(NuRa)$ versus $\log(Ra)$ at 3 m/s.

Table 9: Table of the exponent (b), prefactor (A), slopes (M_1), and intercepts (M_2) of the $Nu(Ra)$ fits and the 95% confidence interval (C.I.) of each constant.

Wind speed (m/s)	b ± 95%C.I.	M_1 ± 95%C.I.	A ± 95%C.I.	M_2 ± 95%C.I.
0	0.37±0.07	-	0.67±0.07	-
1	-	$4.6 \times 10^{-6} \pm 0.5 \times 10^{-6}$	-	341.7±65.1
2	-	$3.3 \times 10^{-6} \pm 3.1 \times 10^{-7}$	-	522.2±87.3
3	-	$-4.7 \times 10^{-6} \pm 4.9 \times 10^{-6}$	-	1009.4±147.3
4	-	$-1.5 \times 10^{-7} \pm 1.8 \times 10^{-7}$	-	1203.1±170
5	-	$1.3 \times 10^{-6} \pm 1.6 \times 10^{-6}$	-	1401±236

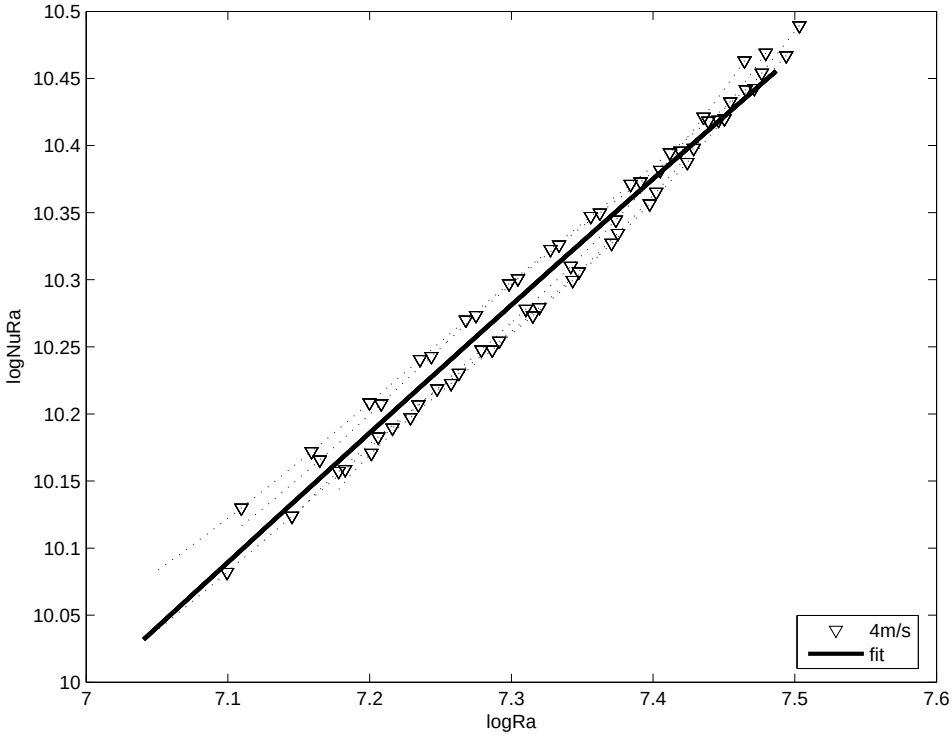

Figure 21: Plot of $\log(NuRa)$ versus $\log(Ra)$ at 4 m/s.

Figure 23 is a plot of Nu versus Re for all wind speeds and it shows the change in Nu with wind speed, with the different points at each wind speed being obtained from different experiments at a constant value of $Ra = 2.5 \times 10^7$. This value of Ra was chosen as all experiments conducted had this Ra value in common. It is evident from Fig. 14 that the number of Ra values in common among all the experiments was very small and also spread over a very small range, thus this was the only value at which an $Nu(Re)$ relationship was obtained. It should be noted that these points were obtained from the calculated Nu values and not from the fits to this data which gave the $Nu(Ra)$ relationships. Thus there are 5 points at each wind speed representing each experiment conducted at that wind speed. The $Nu(Re)$ relationship thus obtained is:

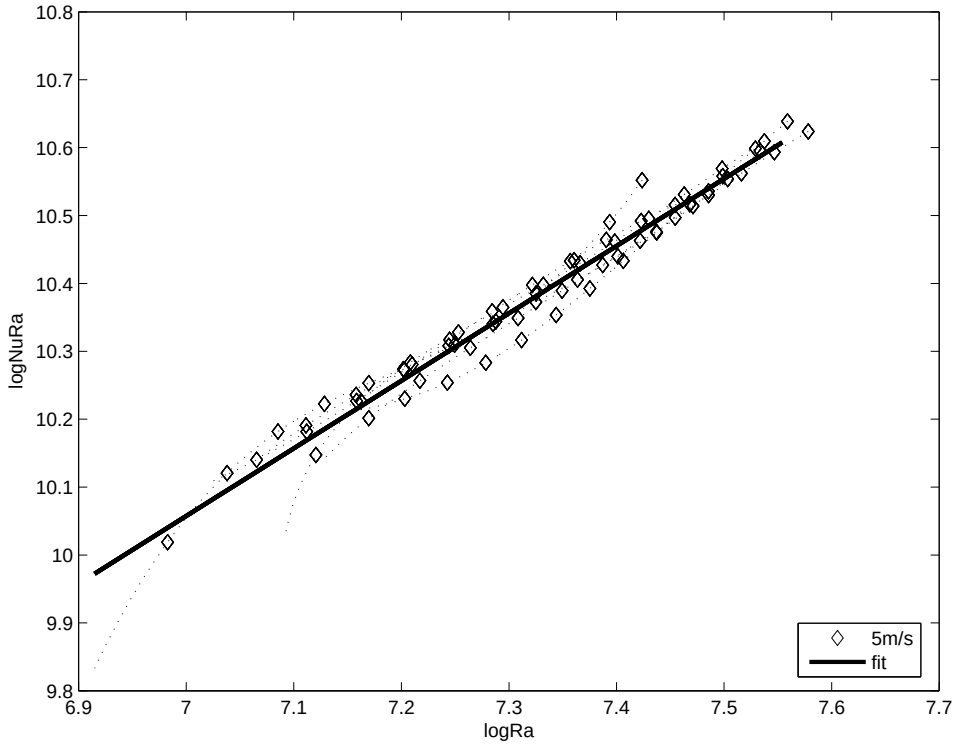

Figure 22: Plot of $\log(NuRa)$ versus $\log(Ra)$ at 5 m/s.

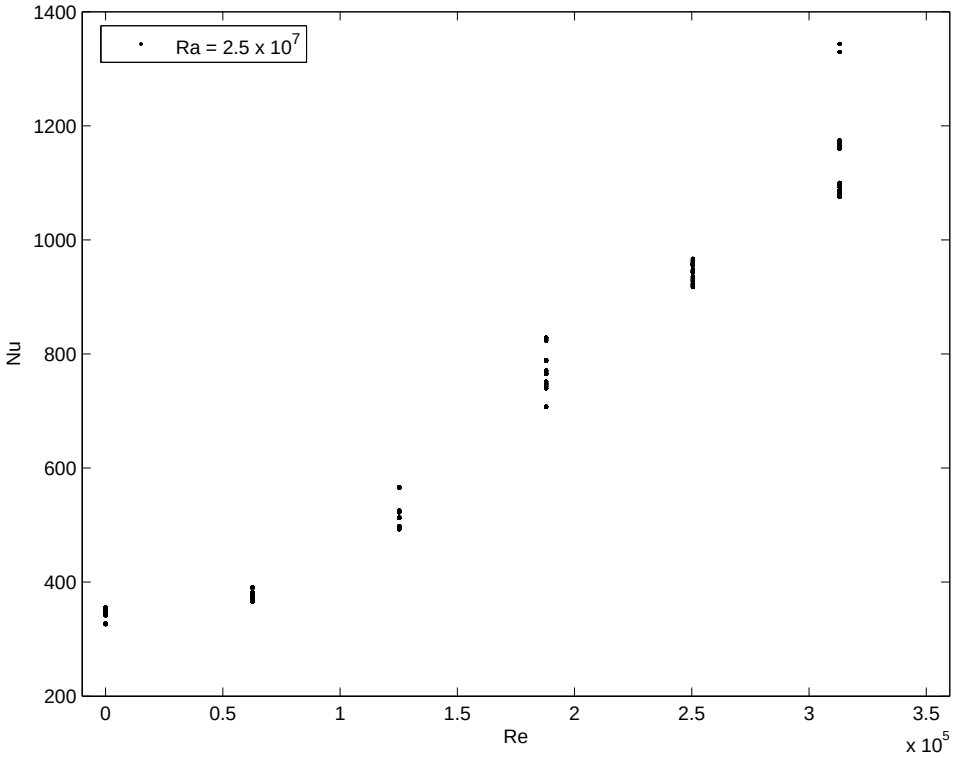

Figure 23: Plot of Nu versus Re for all wind speeds at $Ra = 2.5 \times 10^7$.

$$Nu_f = 0.1585(Re)^{0.85} \tag{99}$$

This relationship is graphically depicted in Fig. 24 where only the wind speeds of 2 - 5 m/s were used to obtain Eq. (99). These wind speeds were selected because they exhibit a strong dependence of Nu on Re. This method of getting the $Nu(Re)$ relationship at constant Ra has been used by Oosthuizen[46] and Pauken.[32] An initial attempt was made to formulate an $Nu(Re)$ relationship by using wind speeds ranging from 1 m/s to 5 m/s. However, all attempts made to use the $Nu(Re)$ relationship obtained in this way when formulating the $Nu(Ra, Re)$ mixed convection relationship gave a very high rms deviation from the fitted functions at each wind speed.

Another method which was tried to obtain the $Nu(Re)$ relationship involved using

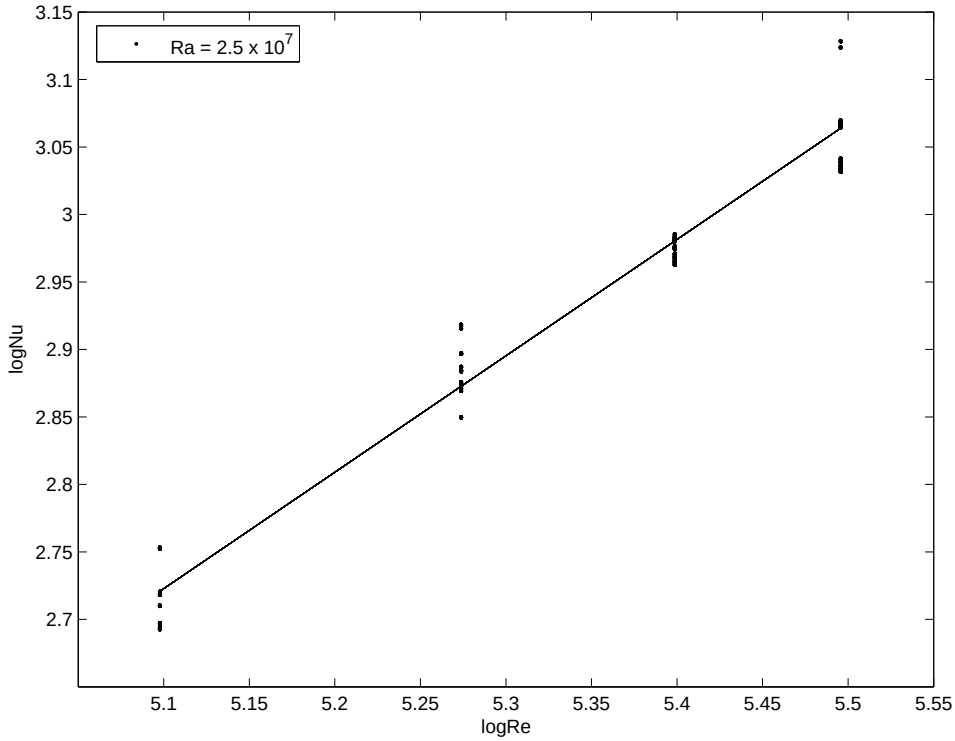

Figure 24: Plot of $\log(Nu)$ versus $\log(Re)$ for wind speeds 2 - 5 m/s at $Ra = 2.5 \times 10^7$.

the intercepts of the $Nu(Ra)$ linear fits obtained for wind speeds 1 - 5 m/s as a measure of zero Ra value of Nu. This was meant to be the completely forced convection dominated value for Nu. A linear fit was obtained between $\log(Nu)$ and $\log(Re)$ using these values, and a power law relationship was obtained between Nu and Re. However, when the $Nu(Re)$ relationship obtained in this way was used to get an $Nu(Ra, Re)$ equation for mixed convection the mixed convection equation showed a very high rms deviation. A similar attempt made by using the intercepts for only wind speeds 2 - 5 m/s also gave a very high rms deviation and was abandoned. The reason behind the failure of this method may be that the linear fits were extrapolated far outside their Ra range to get these intercepts, thus giving an erroneous value of Nu at zero Ra.

Once the individual equations governing the $Nu(Ra)$ relationship at each wind speed and the $Nu(Re)$ equation were obtained, the final step of obtaining a fit to the entire data set was completed. The best fit to the data was given by a vectorial fit to the data using the $Nu(Ra)$ relationship at 0 m/s and the $Nu(Re)$ relationship at constant Ra for wind speeds of 2 - 5 m/s. The form of the equation adopted to obtain this mixed convective equation is:

$$Nu_m = (Nu_n^n + Nu_f^n)^{\frac{1}{n}} \tag{100}$$

Equation (100) was used to obtain the equation governing mixed convective heat transfer, by iterating for the exponent n over a range of -100 to 100 in steps of 0.5 to obtain the best fit to the experimental data. A value of $n = 4$ gave the best fit to the data giving the least rms deviation from the $Nu(Ra)$ values. Smaller iteration increments were not chosen to maintain consistency with past mixed convection studies[32,33,46] which have shown exponents of 3.5[32] and 4.[46] The resulting equation

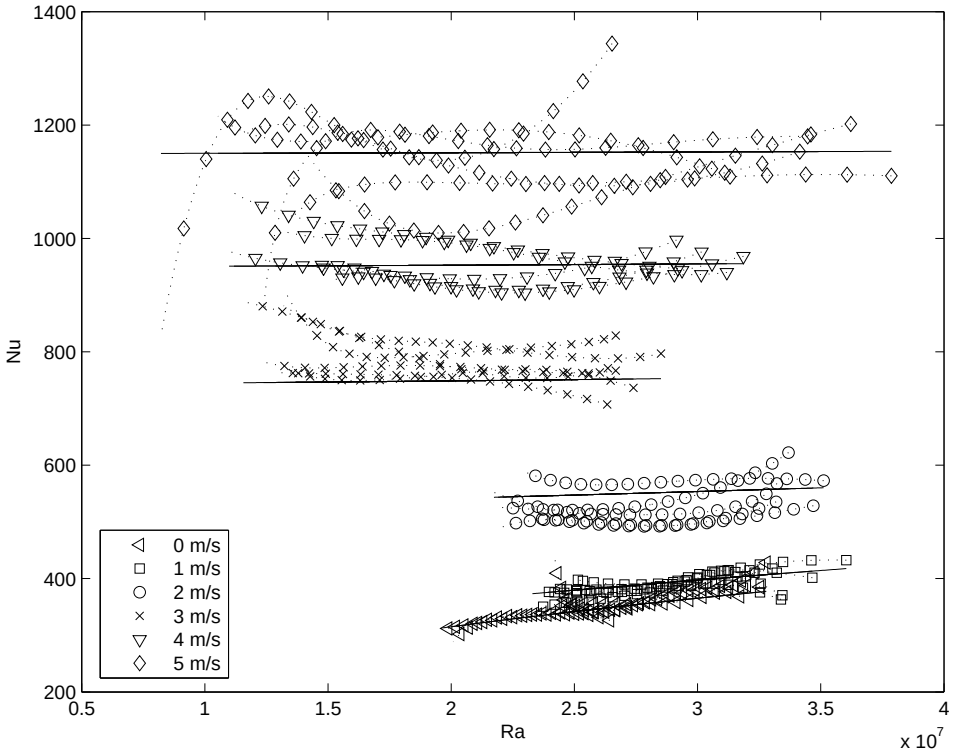

Figure 25: $Nu(Ra, Re)$ relationship predicted by the vectorial additive equation for an exponent of four. Symbols show data and solid lines show vectorial fit.

is:

$$Nu_m = [(0.67Ra^{0.37})^4 + (0.1585Re^{0.85})^4]^{\frac{1}{4}} \tag{101}$$

Figure 25 shows a plot of Eq. (101) along with the experimental data. Figure 26 is a similar plot with an exponent n = 3, revealing unsatisfactory results in that the rms deviation of the values predicted by the mixed convection equation from the $Nu(Ra)$ fit values was very high. Comparing Figs. 25 and 26, the latter can be clearly seen to perform much worse in predicting the $Nu(Ra)$ results. Similar poor behavior resulted when using the vectorial model with other exponents. The performance of the mixed convective equation in predicting the $Nu(Re)$ data can be seen in Fig. 27.

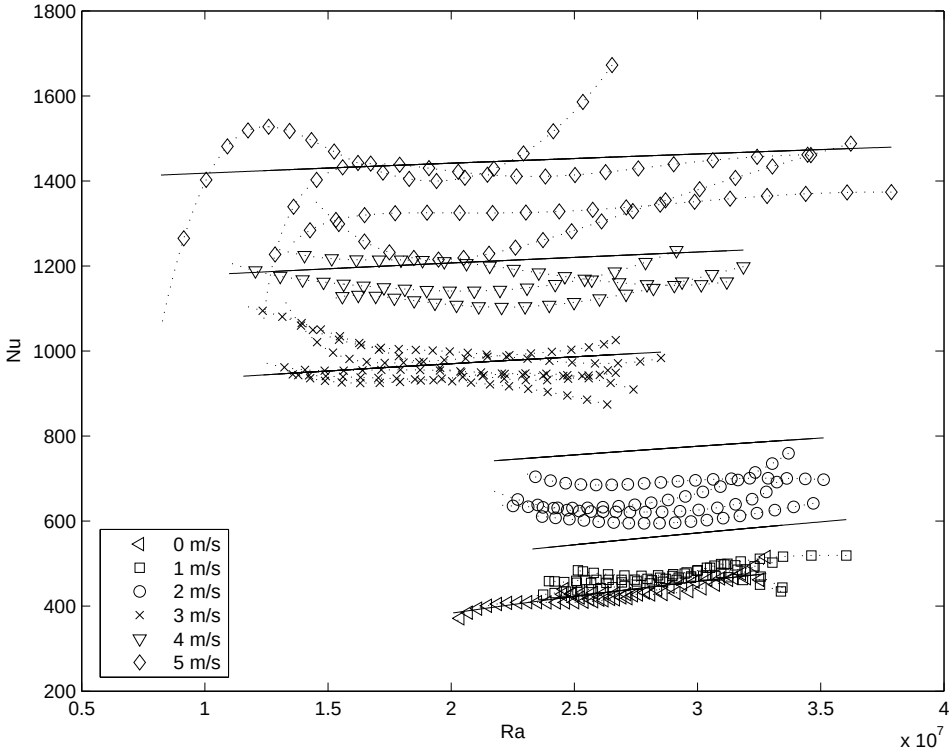

Figure 26: $Nu(Ra, Re)$ relationship predicted by the vectorial additive equation for an exponent of three. Symbols show data and solid lines show vectorial fit.

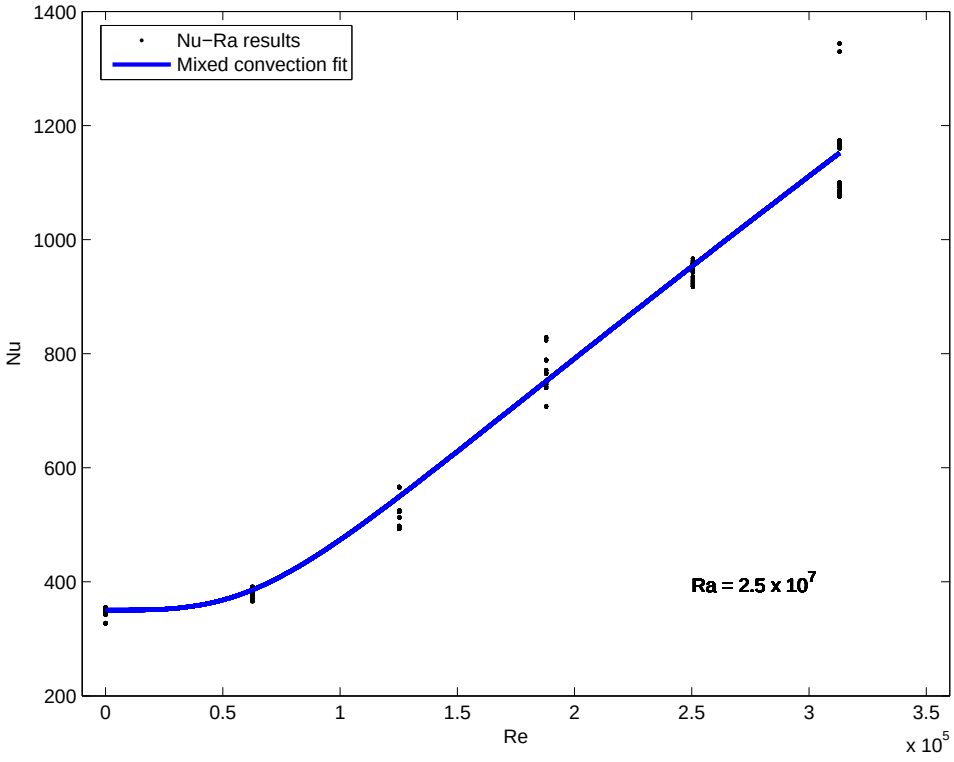

Figure 27: $Nu(Ra, Re)$ relationship predicted by the vectorial additive equation for an exponent of four on $Nu - Re$ coordinates. Symbols show data and the solid line shows the vectorial fit.

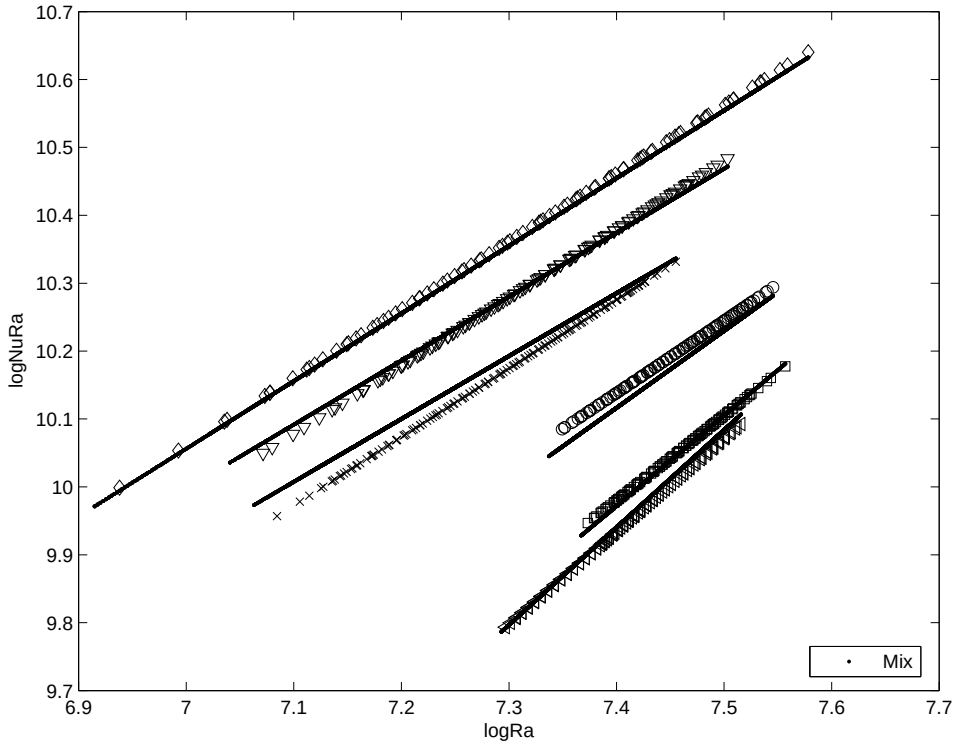

Figure 28: LNR plot of the fits to the $Nu(Ra)$ data with the mixed convection equation superimposed. Solid lines show individual fits and symbols show the performance of the mixed convection equation of exponent four at each wind speed.

Table 10 shows the percent rms deviation from the fits to the experimental data of the mixed convection equation at each wind speed. The percent rms deviation is the rms deviation divided by the fitted experimental values at each wind speed. It can be seen that the mixed convection equation performs best at the lower wind speeds and has the lowest rms deviation at these wind speeds. A better idea of the performance of this fit is provided by Fig. 28 which shows the LNR plot of the mixed convection equation superimposed on the fits to the experimental data at each wind speed. Solid lines show the mixed convection equation fit at each wind speed whereas the symbols show the experimental data.

The different methods described above were tried out to get the function describing the entire data set. Another method which was used to obtain a consolidated

Table 10: Percent rms deviation of the mixed convective equation from the individual fits at each wind speed.

Wind speed (m/s)	% rms deviation
0	8.1
1	9.4
2	9.9
3	16.1
4	14.7
5	15.4

$Nu(Ra, Re)$ relationship was by fitting a 3-D surface to the fitted $Nu(Ra)$ equation at each Re. This was done by plotting the $Nu(Ra)$ fit obtained for each wind speed against Re, and then fitting a surface to this 3-D data optimized to reduce the least squares error of the surface fit. However, this equation gave an rms deviation from the fit worse than that provided by the optimized vectorial fit, and was thus abandoned.

4.5 $Sh(Ra, Re)$ relationships

Figure 29 is a plot of Sh versus Ra for the entire range of wind speeds explored for the research presented here. Five experimental runs were conducted at each wind speed. These are the results obtained by calculating Sh and Ra from the fitted experimental data. That is, each curve is derived from the polynomial function used to fit the temperature and mass data. The format of the plots presented here is the same as that used to present the $Nu(Ra)$ results.

Figure 29 shows that Sh increases with an increase in wind speed as expected. This plot also shows that Sh increases with increasing Ra at wind speeds of 0 and 1 m/s, thus indicating the presence of some natural convection influence. This trend reverses for wind speeds of 2 and 3 m/s, and for wind speeds above 3 m/s Sh is essentially constant.

The functional form fitted to the $Sh(Ra)$ relationships at each wind speed has been

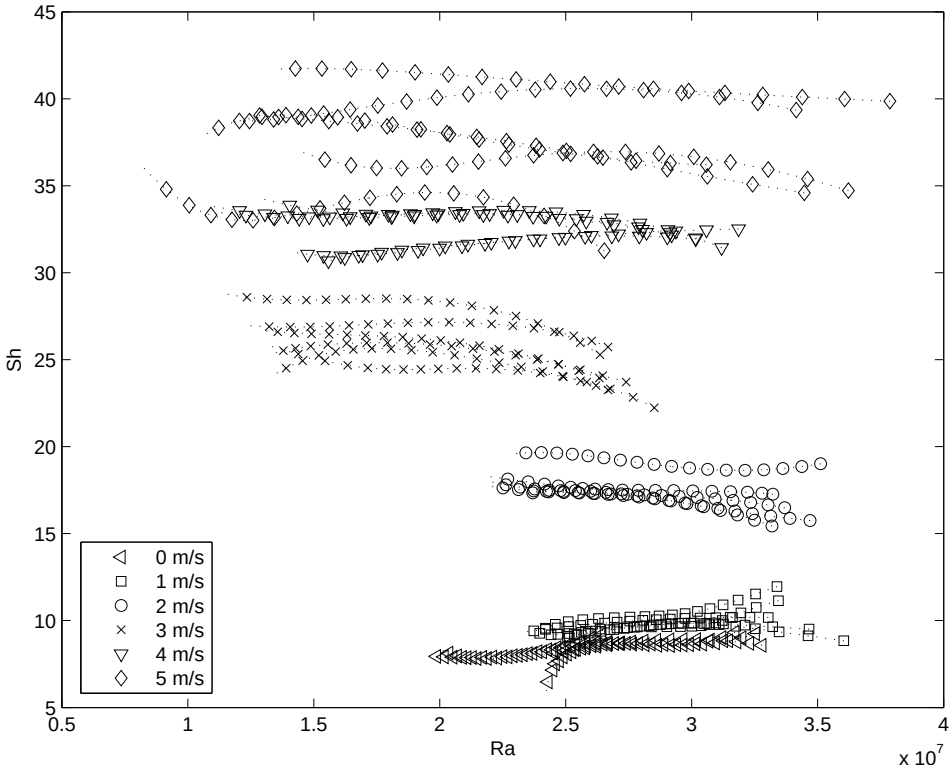

Figure 29: Plot of Sh versus Ra for all wind speeds.

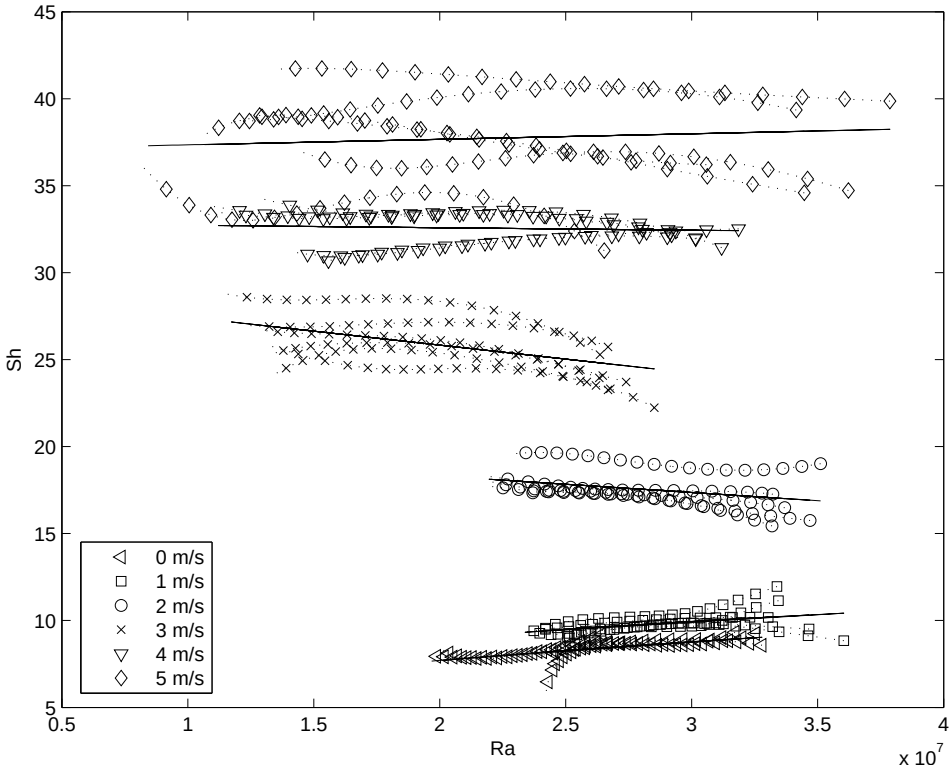

Figure 30: Plot of Sh versus Ra for all wind speeds with the fit at each wind speed superimposed. Symbols and dotted lines show the data and solid lines show the fit.

Table 11: A table of the exponent (b_1), prefactor (A_1), slopes (M_1), and intercepts (M_2) of the $Sh(Ra)$ fits and the standard deviation in each constant.

Wind speed (m/s)	$b_1 \pm$ S.D.	$M_1 \pm$ S.D.	$A_1 \pm$ S.D.	$M_2 \pm$ S.D.
0	0.323±0.05	-	0.029±0.002	-
1	-	$9.5 \times 10^{-8} \pm 1.7 \times 10^{-8}$	-	5.1±0.86
2	-	$6.4 \times 10^{-9} \pm 1.3 \times 10^{-9}$	-	20±2.18
3	-	$-1.3 \times 10^{-8} \pm 3 \times 10^{-9}$	-	28±8.4
4	-	$1.1 \times 10^{-8} \pm 0.4 \times 10^{-8}$	-	34±9.1
5	-	$0.8 \times 10^{-8} \pm 0.4 \times 10^{-9}$	-	42±9.43

explained in Section 4.1. Figure 30 shows the fits thus obtained for each individual wind speed plotted on linear coordinates along with the calculated $Sh(Ra)$ values, the plot pattern being the same as that for the $Nu(Ra)$ fit shown in Fig. 15. The fits obtained confirm the observations made about the $Sh(Ra)$ trends and an uncertainty analysis is presented in Section 5. The quality of the fit and the scatter in the data, which is denoted by the standard deviation (S.D.) of the functional constants for all experiments at a particular wind speed from those of the fitted function is shown in Table 11. It can be seen that the scatter in the experimental data, reflected by the high standard deviation values, is generally higher for experiments with a greater forced convection influence i.e. 3 - 5 m/s than for those with a greater natural convection influence i.e. experiments at wind speeds lower then 3 m/s. This points to the increasing irreproducibility of experiments at the higher wind speeds. The statistical significance of these relationships is shown in Table 12 which shows the 95% confidence interval of the fitting constants at each wind speed. The significance of these fit constants and inferences drawn from them will be discussed in Section 5.

Figure 31 shows a plot of $\log(Sh \cdot Ra)$ versus $\log(Ra)$ for all wind speeds. It can be seen from this plot that the undulations present in the data which were evident in Fig. 29 have been eliminated to a large extent due to the reduction in the uncertainty associated with the ΔT term. This plot will be used to obtain the $Sh(Ra)$ fits and in

Table 12: A table of the exponent (b_1), prefactor (A_1), slopes (M_1), and intercepts (M_2) of the $Sh(Ra)$ fits and the 95% confidence interval (C.I.) of each.

Wind speed (m/s)	$b_1 \pm 95\%$C.I.	$M_1 \pm 95\%$C.I.	$A_1 \pm 95\%$C.I.	$M_2 \pm 95\%$C.I.
0	0.323± 0.065	-	0.029± 0.0049	-
1	-	$9.5 \times 10^{-8} \pm 2.1 \times 10^{-8}$	-	5.1± 1.4
2	-	$6.4 \times 10^{-9} \pm 1.9 \times 10^{-9}$	-	20± 2.88
3	-	$-1.3 \times 10^{-8} \pm 3.7 \times 10^{-9}$	-	28± 4.3
4	-	$1.1 \times 10^{-8} \pm 0.7 \times 10^{-8}$	-	34± 7.10
5	-	$0.8 \times 10^{-8} \pm 0.7 \times 10^{-9}$	-	42± 7.76

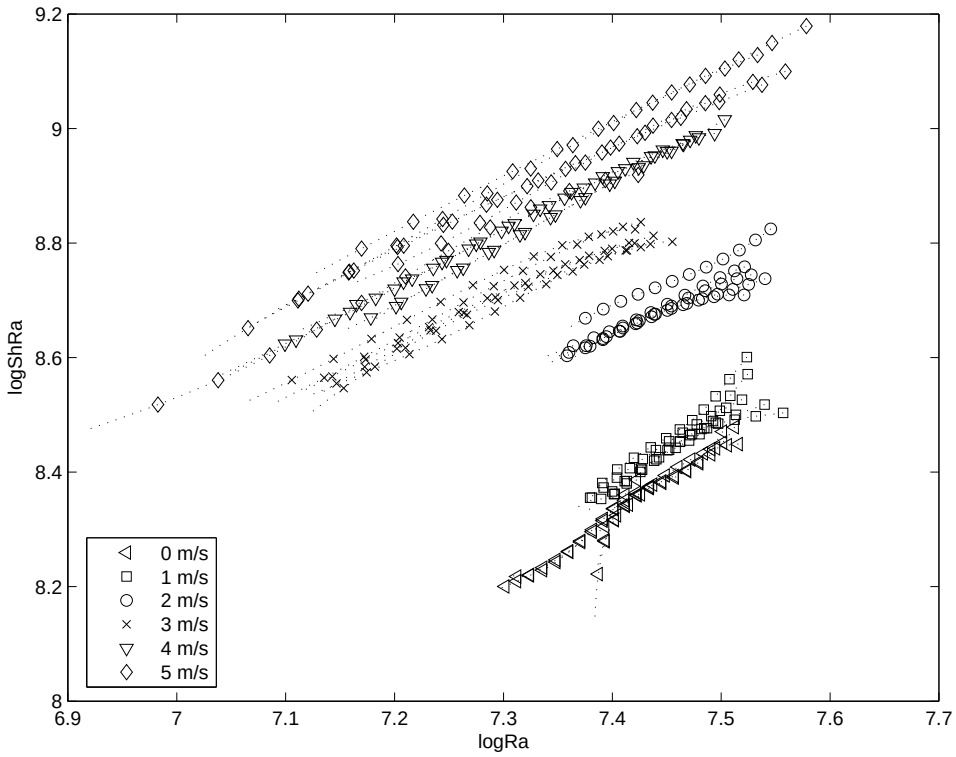

Figure 31: Plot of $\log(ShRa)$ versus $\log(Ra)$ for all wind speeds.

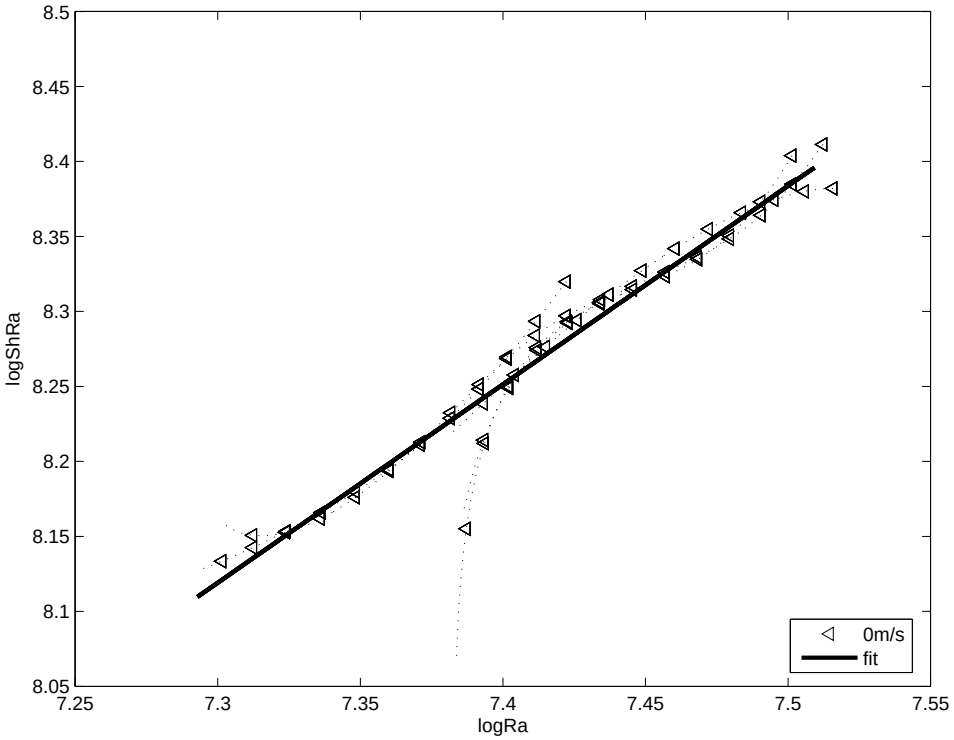

Figure 32: Plot of $\log(ShRa)$ versus $\log(Ra)$ at 0 m/s.

conjunction with an accurate $Sh(Re)$ relationship extract a meaningful $Sh(Ra, Re)$ function which explains the entire data set. The $Sh(Ra)$ fits obtained from this plot are replotted on a linear scale in Fig. 30. All $Sh(Ra)$ relationships will henceforth be presented in this format and such a plot will be referred to as an LSR plot.

Figure 32 is the LSR plot at 0 m/s. The bold line shows the power law fit to the $Sh(Ra)$ data. The Sherwood numbers presented here are accurate to ± 0.19 units with the standard deviation in the exponent and prefactor shown in Table 11. The $Sh(Ra)$ relationship obtained at this wind speed is:

$$Sh_n = 0.029(Ra)^{0.323} \tag{102}$$

The $Sh(Ra)$ relationships for 1 - 5 m/s were obtained from a best fit model to the

Table 13: $Sh(Ra)$ relationships for all wind speeds

Wind speed (m/s)	$Sh = f(Ra)$	G
0	$Sh = 0.029(Ra^{0.323})$	∞
1	$Sh = 9.5 \times 10^{-8} Ra + 5.1$	0.03
2	$Sh = 6.4 \times 10^{-9} Ra + 20$	0.001
3	$Sh = -1.3 \times 10^{-8} Ra + 28$	0.001
4	$Sh = 1.1 \times 10^{-8} Ra + 34$	0.00006
5	$Sh = 0.8 \times 10^{-8} Ra + 42$	0.000004

$Sh \cdot Ra(Ra)$ data. The best fit to this data was given by a linear $Sh(Ra)$ model as discussed in Section 4.1. The $Sh(Ra)$ relationships thus obtained at different wind speeds are graphically shown in Figs. 32 - 37, which are LSR plots for wind speeds 0 - 5 m/s. To reiterate, the dotted line with symbols shows the LSR plot of the Sh and Ra values which were obtained by fitting the raw data and then calculating Sh and Ra based on formulae described in Section 3.4. The solid line is the best fit to the $Sh(Ra)$ data which gives physically meaningful results. The final working relationships for each wind speed are presented in Table 13.

Figure 38 is a plot of Sh versus Re and it shows the change in Sh with wind speed. The different points at each wind speed are calculated Sh values from each experimental run when $Ra = 2.5 \times 10^7$. The sensitivity of Sh to Re decreases at 0 and 1 m/s and thus presents a move away from the forced convective regime. The $Sh(Re)$ equation for forced convection obtained from the data at 2 - 5 m/s is:

$$Sh_f = 0.001(Re)^{0.81} \tag{103}$$

This relationship is graphically depicted in Fig. 39 which is a plot of $\log(Sh)$ versus $\log(Re)$ at a fixed Ra of 2.5×10^7, the reason behind the choice of this Ra being explained in Section 4.4.

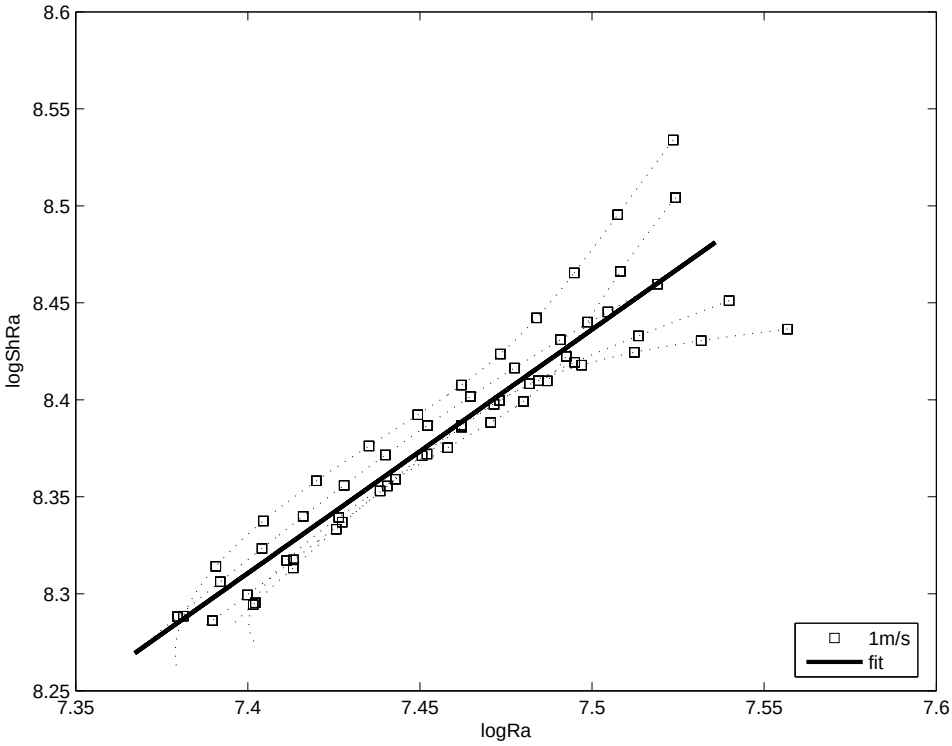

Figure 33: Plot of $\log(ShRa)$ versus $\log(Ra)$ at 1 m/s.

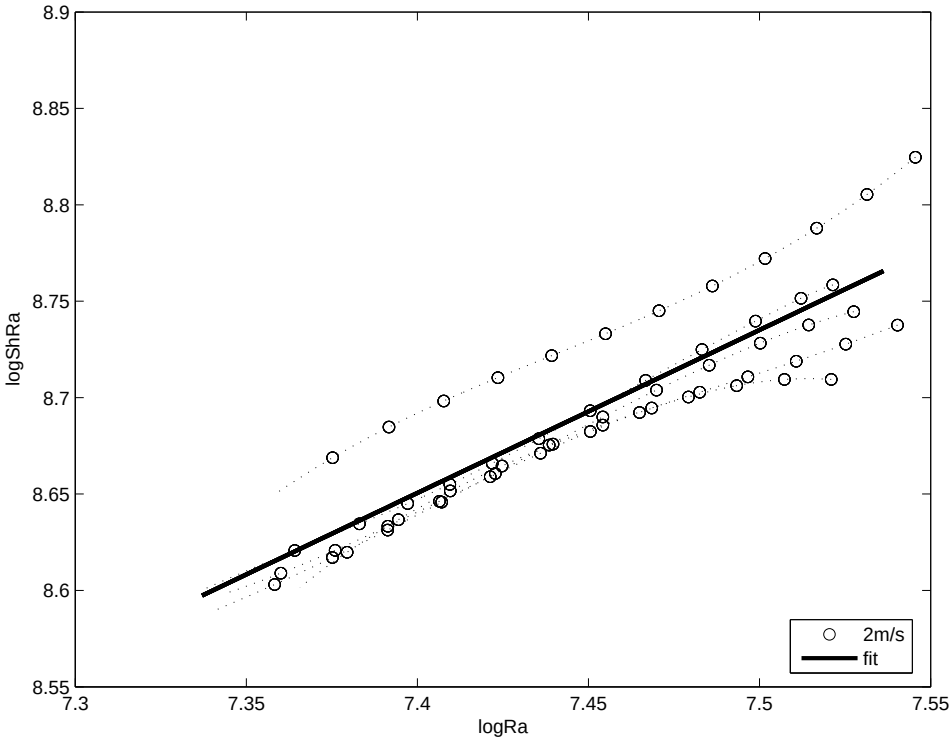

Figure 34: Plot of $\log(ShRa)$ versus $\log(Ra)$ at 2 m/s.

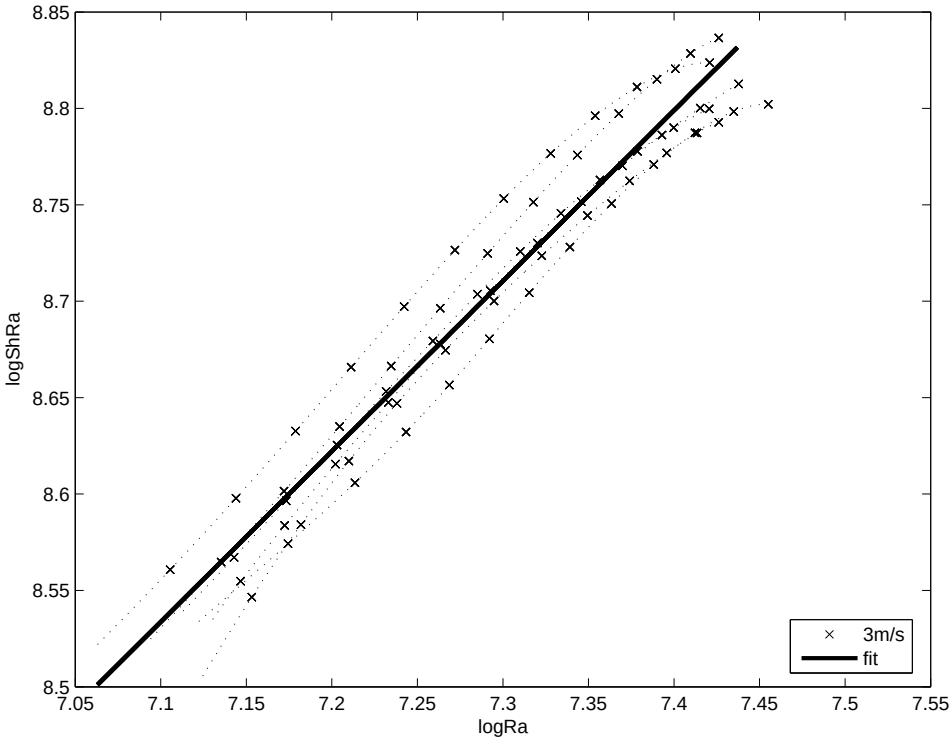

Figure 35: Plot of $\log(ShRa)$ versus $\log(Ra)$ at 3 m/s.

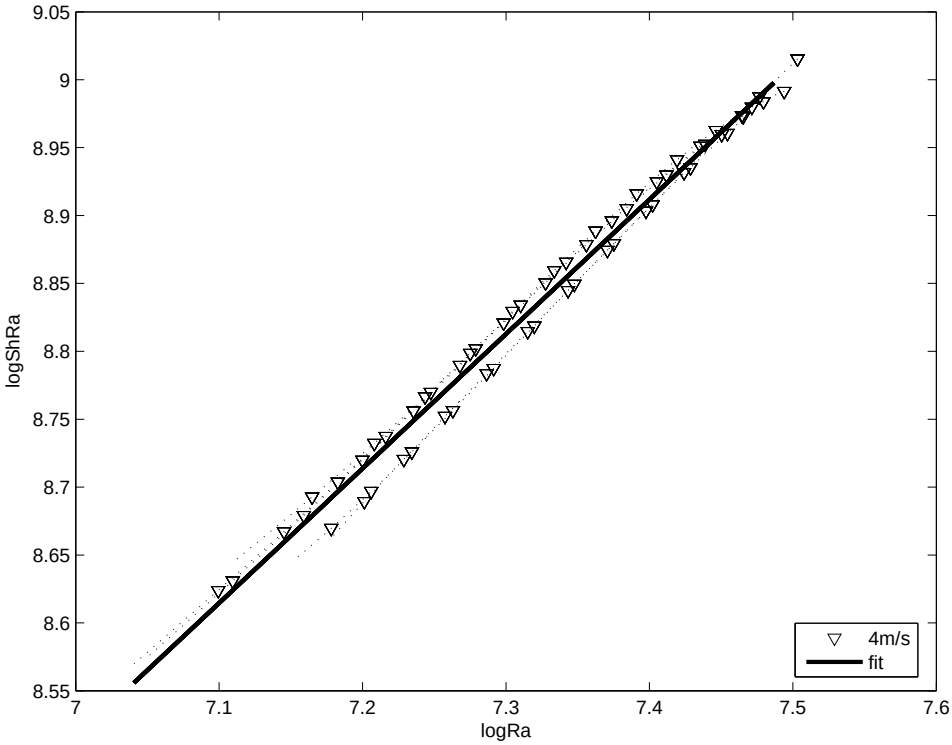

Figure 36: Plot of $\log(ShRa)$ versus $\log(Ra)$ at 4 m/s.

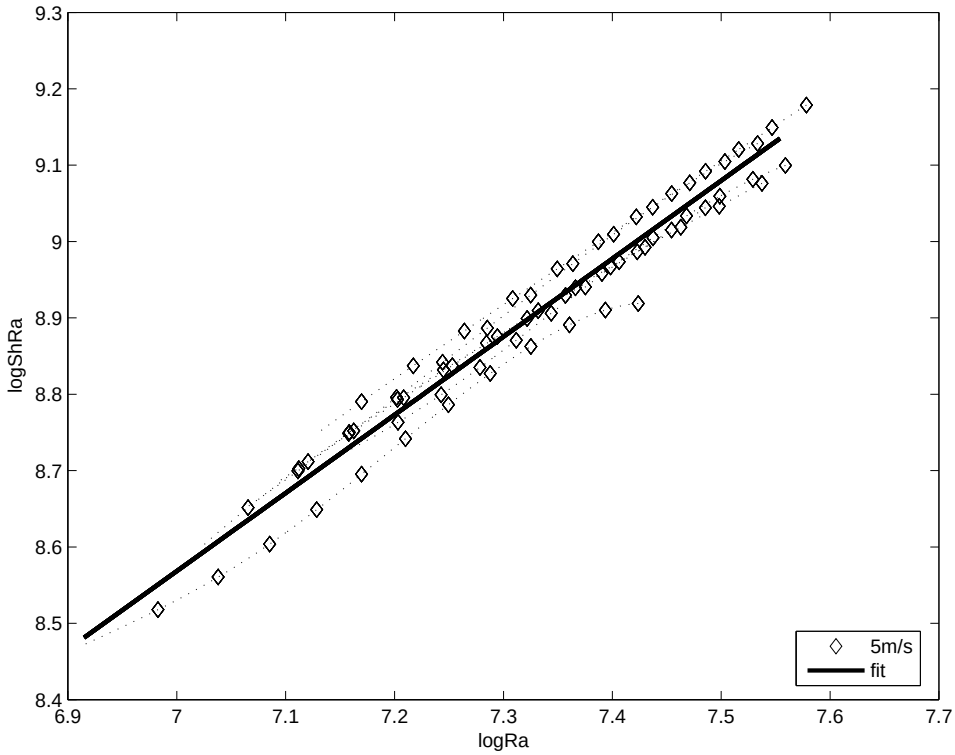

Figure 37: Plot of $\log(ShRa)$ versus $\log(Ra)$ at 5 m/s.

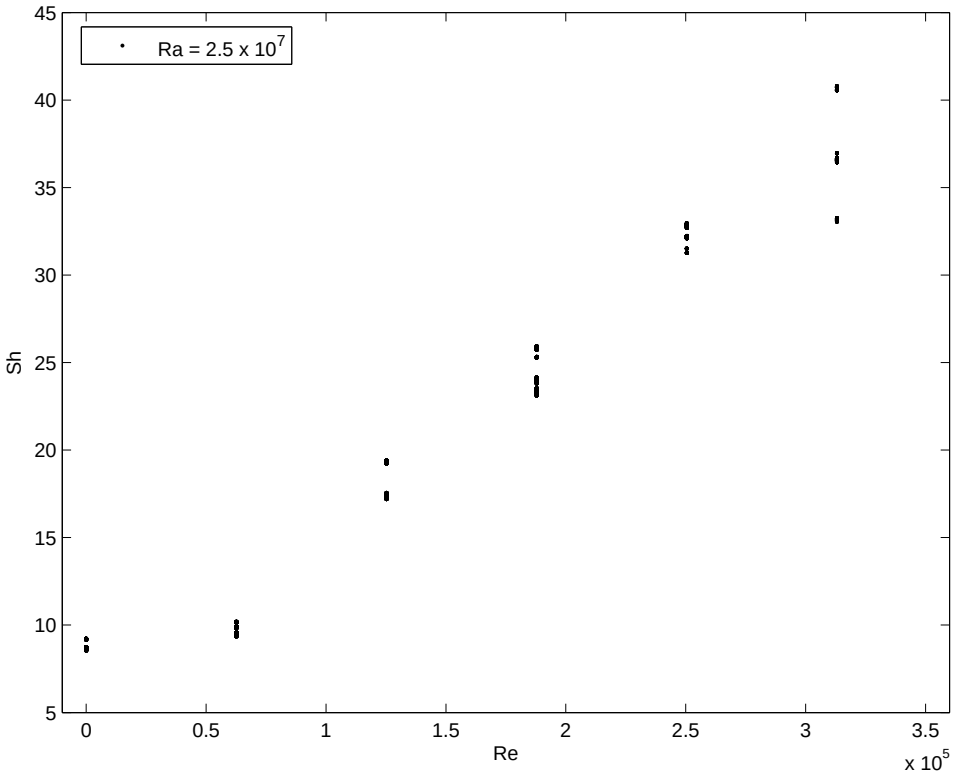

Figure 38: Plot of Sh versus Re for all wind speeds at $Ra = 2.5 \times 10^7$.

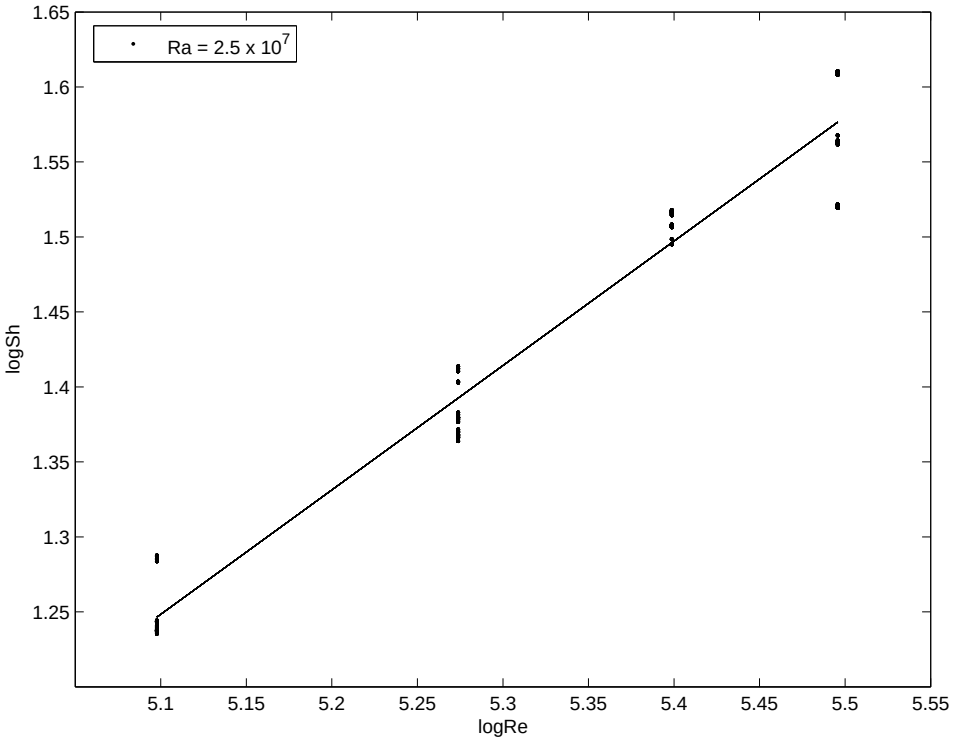

Figure 39: Plot of $\log(Sh)$ versus $\log(Re)$ for wind speeds 2 - 5 m/s at $Ra = 2.5 \times 10^7$.

Once the individual $Sh(Ra)$ relationship at each wind speed and the $Sh(Re)$ relationship were obtained, the final step of obtaining a fit to the entire data set was completed. The best fit to the data was given by a vectorial fit to the data using the $Sh(Ra)$ relationship at 0 m/s and the $Sh(Re)$ relationship at constant Ra for wind speeds of 2 - 5 m/s. The form of the equation adopted to obtain this mixed convective equation is:

$$Sh_m = (Sh_n^p + Sh_f^p)^{\frac{1}{p}} \tag{104}$$

Equation (104) was used to obtain the equation governing mixed convective heat transfer, by iterating over the exponent n to obtain the best fit to the experimental data. A value of $n = 4$ gave the best fit to the data giving the least rms deviation from the $Sh(Ra)$ values. The full form of this equation therefore, is:

$$Sh_m = [(0.029Ra^{0.323})^p + (0.001Re^{0.81})^p]^{\frac{1}{p}} \tag{105}$$

This mixed convective equation is graphically depicted in Fig. 40, the symbols and dotted lines represent the fitted experimental results, whereas the solid lines show the predicted $Sh(Ra)$ relationship obtained by using Eq. (105). Figure 41 shows a sample plot at an exponent of 3, which gave unsatisfactory results. Similar results were given by a vectorial model with other exponents. The performance of the mixed convective equation in predicting the $Sh(Re)$ data can be seen in Fig. 42.

Table 14 shows the percent rms deviation of the $Sh(Ra)$ relationships from the fits to the experimental data obtained at each wind speed from the mixed convection equation. The percent rms deviation is the rms deviation divided by the fitted

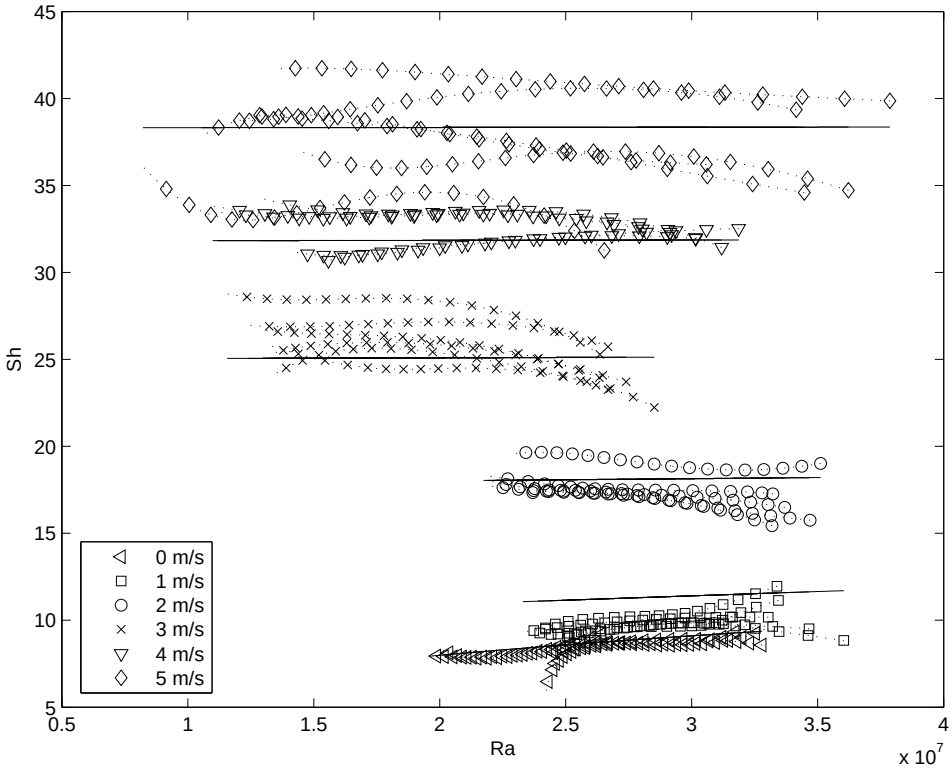

Figure 40: Performance of the $Sh(Ra, Re)$ relationship predicted by the mixed convection equation for an exponent of four.

Table 14: Percent rms deviation of the mixed convective equation from the individual fits at each wind speed.

Wind speed (m/s)	% rms deviation
0	7.9
1	19.6
2	9.1
3	16.5
4	15.1
5	14.8

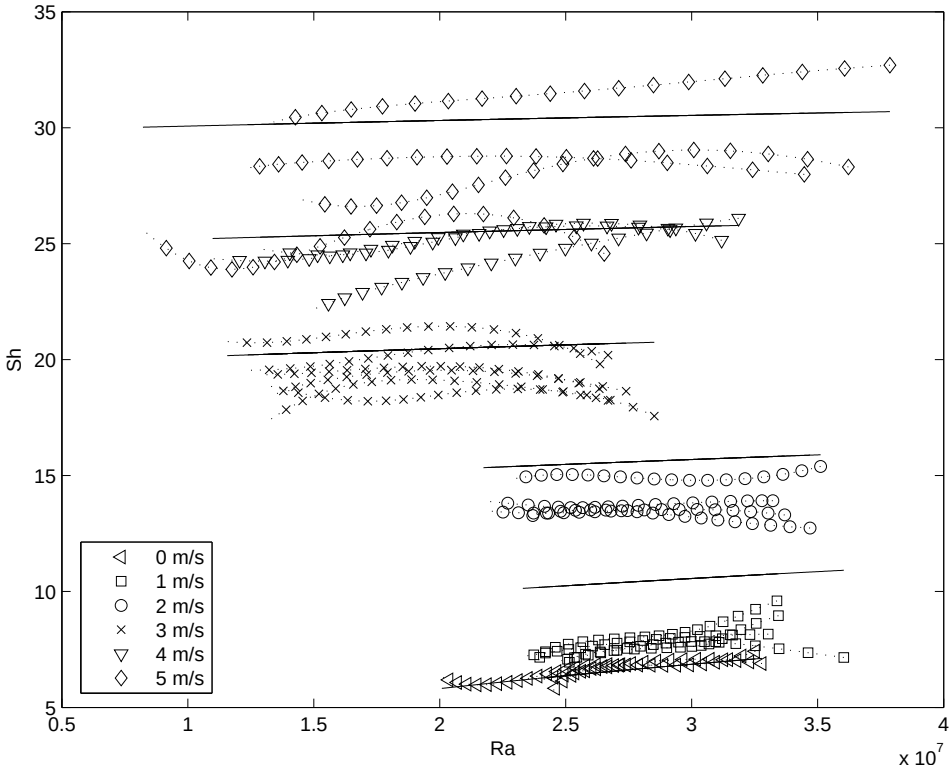

Figure 41: Performance of the $Sh(Ra, Re)$ relationship predicted by the mixed convection equation for an exponent of three.

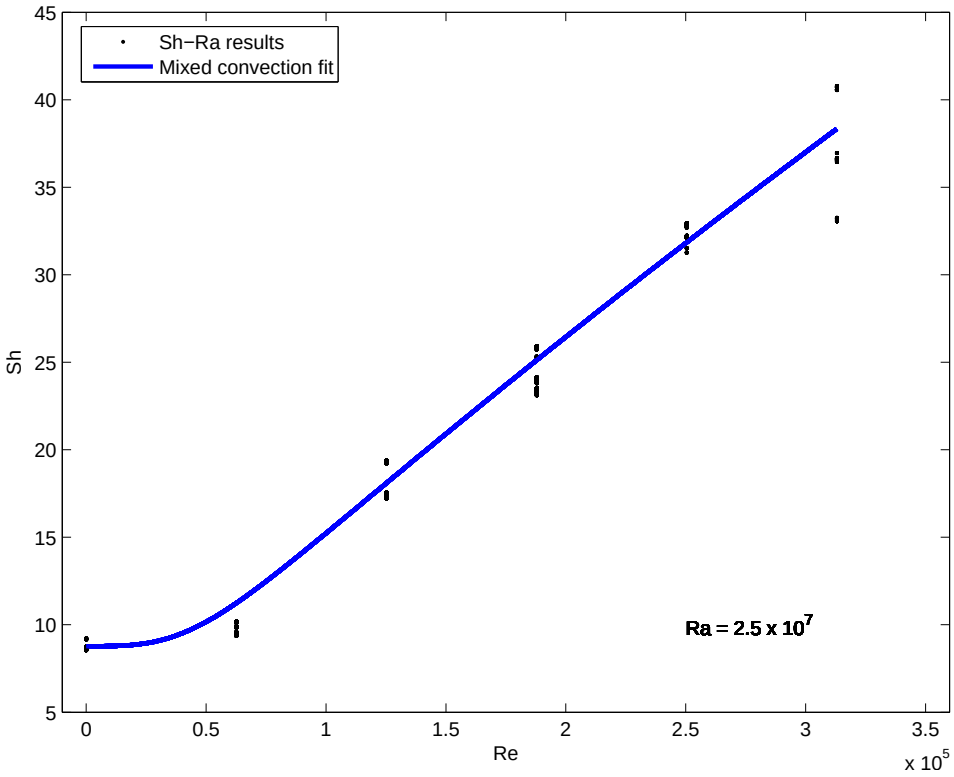

Figure 42: $Sh(Ra, Re)$ relationship predicted by the vectorial additive equation for an exponent of four on $Sh - Re$ coordinates. Symbols show data and the solid line shows the vectorial fit.

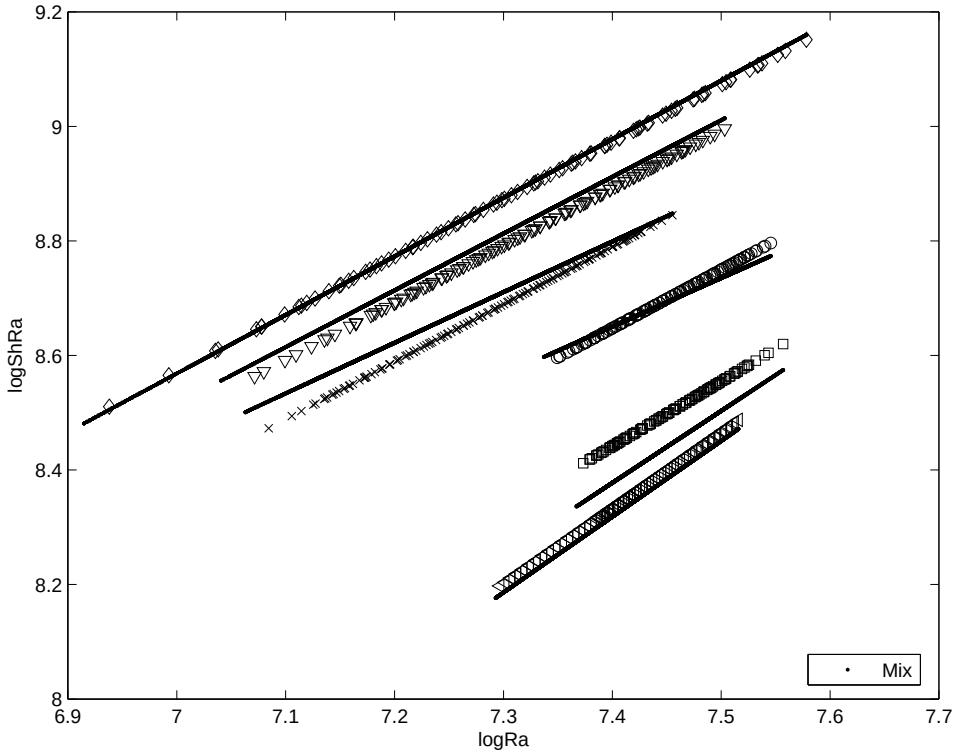

Figure 43: LSR plot of the fits of the $Sh(Ra)$ data with the mixed convection equation superimposed. Symbols show individual fits at each wind speed and solid lines show the performance the of mixed convection equation of exponent four.

experimental results at each wind speed. Overall, the $Nu(Ra, Re)$ mixed convection equation performs better than the $Sh(Ra, Re)$ equation. A better idea of the performance of the $Sh(Ra, Re)$ vectorial fit is provided by Fig. 43 which shows the LSR plot of the mixed convection equation superimposed on the fits to the experimental data. The plot format is similar to Fig. 28.

Another method which was attempted to obtain an $Sh(Ra, Re)$ equation utilized a surface fit as in the case of the $Nu(Ra, Re)$ equation. However, this method showed an rms deviation of the data from the surface fit which was much worse than the vectorial additive fit. An $Sh(Ra, Re)$ equation was also attempted by using the $Sh(Re)$ relationship modeled from the intercepts of the linear fits to the data at 1 - 5 m/s and also 2 - 5 m/s as a separate attempt. The combined $Sh(Ra, Re)$ equation

modeled using both these methods gave an rms deviation of the data from the fit that was very high. Thus, these methods were abandoned in favor of the vectorial additive fit.

5 DISCUSSION

The discussion of the results is categorized in two sections: discussion of $Nu(Ra, Re)$ results and discussion of $Sh(Ra, Re)$ results.

5.1 Curve fitting procedure

The method of fitting the raw data was described in Section 3.4. It was mentioned there that the best fit to the data that was physically appropriate was chosen to fit the data. It was seen that for the various polynomial fits chosen to fit the raw data, the 22^{nd} order polynomial fit fitted the data with the least rms deviation of the fit from the data. However, this fit gave extrema in the time derivatives of the raw temperature and mass data which were physically incorrect. Thus the lowest order fit which minimized these extrema while at the same time fitting the data reasonably accurately was chosen. The quality of the fit was judged from the rms deviation of the data from the fit. The fit thus chosen was a fourth order polynomial fit.

It can be seen from the $Nu(Ra)$ plots shown in Section 4.4 that the extrema that had to be avoided are still present in the plot. This could only be eliminated by reducing the order of the polynomial function fitting the raw temperature and mass data. Figure 44 shows a plot of Nu versus Ra obtained by fitting the raw data by a second order polynomial. It can be clearly seen from this plot that the $Nu(Ra)$ relationships obtained at the lower Ra have a large scatter with the non-physical behavior seen with the fourth order fit still present. Thus a compromise was reached between modeling the data physically as accurately as possible without sacrificing the accuracy of the fitting procedure by utilizing the fourth order polynomial fit.

5.2 $Nu(Ra, Re)$ results

Table 15 outlines the relevant prior work on convective heat transfer, the parameter range explored, the experimental configuration and their results. The results obtained

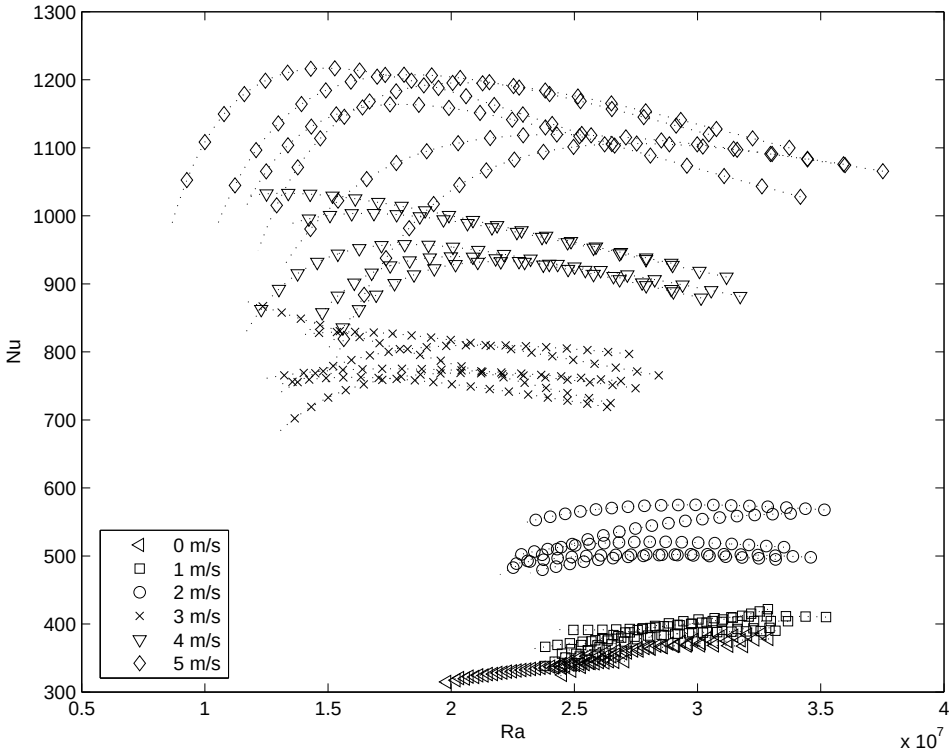

Figure 44: Plot of Nu versus Ra for all wind speeds obtained from a second order fit to the raw data.

Table 15: Comparison of $Nu(Ra)$ results of different studies.

Study	Config.	Re range	Ra range	$Nu(Ra)/Nu(Re)$ reln.
Present	Evap - N	-	$1.1 \times 10^7 - 4.1 \times 10^7$	$Nu = 0.67Ra^{0.37}$
Globe and Dropkin[3]	RB - N	-	$1 \times 10^5 - 7 \times 10^8$	$Nu = 0.069Ra^{0.33}$
Katsaros *et al.*[4]	Evap - N	-	$3 \times 10^8 - 4 \times 10^9$	$Nu = 0.06Ra^{0.33}$
Chu and Goldstein[2]	RB - N	-	$10^8 - 2 \times 10^{11}$	$Nu = 0.055Ra^{0.33}$
Garon[88]	RB - N	-	$10^7 - 3 \times 10^9$	$Nu = 0.1Ra^{0.293}$
Present work	Evap - F	$1.4 \times 10^5 - 3.5 \times 10^5$	-	$Nu = 0.1585Re^{0.85}$
Boyarishnov[70] *et al.*	Evap - F	?	-	$Nu = 0.67Re^{0.8}$
Katto[67]	Evap - F	$10^5 - 4 \times 10^5$	-	$Nu = 0.06Re^{0.8}$
Oosthuizen[46]	FL - F	?	-	$Nu = 0.59Re^{0.5}$

in the present work are compared with these studies.

Table 15 is divided in two parts, the top half compares the natural convection results, and the bottom half compares the forced convection results from different studies. In this table, 'RB' refers to Rayleigh-Bénard studies, 'Evap' refers to evaporative studies and 'FL' refers to flat plate studies. The extensions -N and -F stand for 'natural' and 'forced' thus indicating the transport regime.

It can be seen from the table that the natural convection results for the present work are close to the $\frac{1}{3}$ power law relationship which is typical of natural convection results obtained over a flat plate, and the geometry of the experimental setup here is similar to a flat plate. The small deviation in the results can also be logically explained. While Katsaros *et al.*[4] are the only researchers who study natural convection for an air-water interface, there are some dissimilarities from the research presented here as they do not account for the heat lost due to evaporation, thus effectively defining the Nusselt number on the basis of the total heat lost due to evaporation and convective heat transfer. In the research done for this thesis the contribution of evaporative heat loss to the total heat lost from the air-water interface during natural convection increased as the temperature decreased i.e. as Ra decreased. This indicates a greater percentage change in the convective heat loss compared to the per-

centage change in the total heat loss as Ra decreases. Thus, should the evaporative loss be included in the calculation of the Nusselt number, it will result in a smaller reduction in Nu as Ra decreases i.e. a smaller exponent for the $Nu(Ra)$ relationship. This can explain the results obtained by Katsaros *et al.*[4] Secondly, Katsaros *et al.*[4] define the heat transfer process for the water side of the air-water interface whereas it is defined for the air side for the work done for this thesis. The effect of this on the $Nu(Ra)$ relationship obtained cannot be gauged. This can explain the small deviation in the natural convection results obtained in the present research.

Another point to note is the fact the while the exponent for natural convection is 0.37, it has an uncertainty of ± 0.07 units associated with it. Thus, the exponent may vary from to 0.3 to 0.44 which included the $\frac{1}{3}$ power law that has been observed. Thus, this study which is among the first that obtained air-water interfacial natural convective results with the presence of foreign surfactants on the water surface, shows that the results under such a scenario are close to the natural convection power law results obtained in general and also to the results obtained by Katsaros *et al.*

The second section of Table 15 compares the results obtained by different researchers studying the relationship between Nu and Re for forced convective heat transfer. The listed studies are those which are closest in terms of the experimental scenario to the present work. While the results of Oosthuizen[46] differ from the present work, the study by Boyarishnov *et al.*[70] is closest in its results to the present work. This may be explained by the fact that Boyarishnov *et al.* work over the same parameter range and for the same experimental configuration as the present work while Oosthuizen works over a much smaller Re range. The exponent of the $Nu(Re)$ relationship obtained in the present work, being 0.85, is very close to the classic turbulent flat plate exponent of 0.8 and falls within the general range of Re exponents from 0.5 to 0.8 that has been seen by previous researchers.

It is evident from the results obtained that the scatter in the data increases as

the wind speed increases. This is also indicated by the high value of the S.D. in the fitting constants at the higher wind speeds. This should be expected because the surfactant loss rate increases with wind speed, thus complicating maintenance of consistent surface conditions.

The individual natural and forced convective relationships obtained in this study were used to develop a mixed convective equation which provided a consolidated $Nu(Ra, Re)$ relationship which can explain the $Nu(Ra)$ trend over the entire range of Re. The performance of the mixed convection equation is shown in Table 10. It can be seen here that the rms deviation of the $Nu(Ra)$ relationships predicted by the mixed convection equation for each wind speed indicates that the mixed convection equation is reasonably accurate within the Ra and Re range of these experiments. However, for all instances, the percentage rms deviation of the relationships predicted by the mixed convection equation from the $Nu(Ra)$ fits to the fitted experimental data is less than 16%.

The $Nu(Ra)$ relationships and the C.I. of the fitting constants obtained at each wind speed are tabulated in Table 9 and shown in Fig. 15. It can be seen that Nu is dependent on Ra for wind speeds of 0 and 1 m/s whereas for wind speeds of 3 - 5 m/s, Nu is largely independent of Ra as seen from the slope of the $Nu(Ra)$ plot. However, the slope is very close to zero at 2 m/s, thus it can be concluded that the mixed convection region falls between 1 and 3 m/s for this experimental setup and is very close to 2 m/s. It can also be concluded that the air-water system is natural convection dominated at 0 and 1 m/s and forced convection dominated for 3 - 5 m/s. The same conclusion can be drawn from the $Nu(Ra)$ fits at each wind speed given by the vectorial additive equation. The table also shows the value of the comparative term G which was introduced in a bid to identify the transport regime present during experimentation. However, it was seen that the values of the term G indicated the presence of forced convection throughout the range of wind speeds from 1 - 5 m/s.

Table 16: Comparison of $Sh(Ra)$ results of different studies.

Study	Config.	Re range	Ra range	Relation
Present work	Evap - N	-	$1.1 \times 10^7 - 4.1 \times 10^7$	$Sh = 0.029(Ra)^{0.323}$
Pauken[32]	Evap - N	-	?	$Sh = 0.14(Ra_m)^{0.33}$
Present work	Evap - F	$0 - 3.5 \times 10^5$	-	$Sh = 0.001(Re)^{0.81}$
Pauken[32]	Evap - F	?	-	$Sh = 1.3(Re)^{0.5}$
Smolsky[69]	TF - F	?	-	$Sh = 0.4(Re)^{0.67}$

As from the $Nu(Ra)$ and $Nu(Re)$ data it is known that experiments at 1 m/s are natural convection dominated, and also the fact that this term had been derived for mixed convection over solid bodies and the present research focuses on the air-water interface, this term is thus not used as a tool to identify the transport regimes.

5.3 $Sh(Ra, Re)$ results

Table 16 outlines the available studies on evaporative mass transfer, the parameter range explored, the medium of mass transfer and their results. The results obtained in the present work are compared with these studies.

The top half of the table compares the $Sh(Ra)$ i.e. natural convection results while the bottom half compares the $Sh(Re)$ i.e. forced convection results of different studies. In the table 'TF' refers to evaporative studies from a thin film on a flat plate. The exponent of the $Sh(Ra)$ relationships obtained here is 0.323. However, it should be noted that this value of the exponent is accurate to ± 0.07 and thus can have any value from 0.25 to 0.39. The exponent of the $Sh(Re)$ relationship, being 0.81, is also very close to the classic 0.8 power law relationship between Sh and Ra that has been observed.

Pauken[32] relates a mass transfer Rayleigh number to the Sherwood number, and though this study is similar to the present research Pauken does not employ surfactants to maintain consistent surface conditions. Inspite of this fact, the results

obtained by Pauken fall within the C.I. of the natural convection results obtained in the present work. Smolsky[69] studied the evaporative mass transfer process from a thin film applied to a flat plate. Thus, a comparison between this study and the present work is not possible due to the difference in the experimental setup. This table reflects the lack of available literature on $Sh(Ra, Re)$ relationships for the experimental setup similar to the present work.

As seen in Figs. 29 and 38 the nature of the $Sh(Ra)$ relationships obtained in the present work suggest a minimal role played by forced convection at 1 m/s. This scenario however quickly changes for wind speeds greater than 1 m/s. It can be seen from Figs. 29 and 38 that the $Sh(Ra)$ curve obtained at 2 m/s, shows a sudden transition away from natural convection. This dependence reduces further at 3 m/s, with the least Rayleigh number dependence seen at this wind speed. In fact, a negative slope is seen at 2 and 3 m/s, which is counter-intuitive as it suggests an increase in the mass transfer coefficient as Ra reduces. The general Ra dependence of Sh at 4 and 5 m/s is much smaller than that at 0 and 1 m/s and these runs can be considered to be forced convection dominated runs. These results are counter-intuitive as an increase in Re should produce a continuous trend of reducing Ra dependence of Sh. An explanation of the negative slope at 2 and 3 m/s will be provided in Section 5.4 which shows the $Sh(Ra)$ relationships at different wind speeds considering ΔT_a to be the temperature difference creating the water vapor density difference driving evaporation as opposed to ΔT_g. It will be shown in this section that the counter-intuitive $Sh(Ra)$ relationship seen at 2 and 3 m/s can be explained by computing Sh and Ra using ΔT_a. This trend can be considered to be an accurate representation of the actual $Sh(Ra)$ trend though the accuracy of the fit constants themselves is doubtful due to the use of the limited IR data available for obtaining these relationships.

The individual natural and forced convective relationships obtained in this study were used to develop a mixed convective equation which provided a consolidated

$Sh(Ra, Re)$ relationship that can explain the $Sh(Ra)$ trend over the entire range of Re. The performance of this mixed convection equation in predicting the data is shown in Table 14. It can be seen here that the rms deviation of the $Sh(Ra)$ relationships predicted by the mixed convection equation from the fits obtained indicates that the mixed convection equation is reasonably accurate within the Ra and Re range of these experiments. For all wind speeds, the percentage rms deviation of the relationships predicted by the mixed convection equation from the $Nu(Ra)$ fits to the fitted experimental data is less than 20%.

The $Sh(Ra)$ relationships and the C.I. of the fitting constants obtained at each wind speed are tabulated in Table 12 and the fits are shown in Fig. 30. It can be seen here that Sh is dependent on Ra for wind speeds of 0 and 1 m/s whereas for wind speeds 3 - 5 m/s, Sh is largely independent of Ra as seen from the slope of the $Sh(Ra)$ plot. However, the slope is very close to zero at 2 m/s, thus it can be concluded that the mixed convection region falls between 1 and 3 m/s for this experimental setup and is very close to 2 m/s. It can also be concluded that the air-water system is natural convection dominated at 0 and 1 m/s and forced convection dominated for 3 - 5 m/s. The same conclusion can be drawn from the $Sh(Ra)$ fits at each wind speed given by the vectorial additive equation.

5.4 $Sh(Ra)$ relationships using surface temperatures.

The $Sh(Ra)$ results presented in Section 4.5 were obtained by considering ΔT_g to be the temperature difference creating the water vapor density difference which is the driving force behind the evaporation process. However, as has been discussed before, it is ΔT_a which drives this process and it was due to the errors in the measurements made using the IR camera that the use of ΔT_a was not feasible. Thus, the effect of using ΔT_g instead of ΔT_a in calculating Sh needs to be studied. It should be noted that this will only demonstrate a qualitative effect and will not be used to

Table 17: Estimates of ΔT_w at the start and end of experiments at each wind speed.

Wind speed (m/s)	ΔT_a at start	ΔT_a at end
0	2.5	2.5
1	3.0	2.6
2	2.5	1.5
3	3.5	2.2
4	3.6	2.0
5	4.0	2.5

quantify the uncertainty in the $Sh(Ra)$ due to using ΔT. The most reliable means of carrying out this study was by first assuming a certain reasonable value of ΔT_w to be utilized in calculating T_s. From the limited IR data available, a measure of ΔT_w at the start and end of each experiment was obtained and a characteristic value of ΔT_w at the start and end of experiments at each wind speed was obtained from these values. The aim of this exercise was only to study the qualitative effect of using the surface temperature on the $Sh(Ra)$ trends, thus the quantitative uncertainty in the IR measurement is not measured here. The estimates of ΔT_w obtained at each wind speed are shown in Table 17.

Since data on values of ΔT_w at the start and end of each experiment was now available, assuming a linear drop in ΔT_w, values of ΔT_w and consequently of T_s were obtained for the entire length of experiments at each wind speed. Using these estimates of T_s, the new values of Sh were calculated as were the $Sh(Ra)$ relationships at each wind speed for these values. These relationships are presented in Table 18 and graphically depicted in Fig. 45. Table 19 shows the confidence interval of the fit constants thus obtained.

It is evident that the negative slope in the $Sh(Ra)$ which was seen at 2 and 3 m/s is not seen when ΔT_a is used instead of ΔT_g. These relationships define the $Sh(Ra)$ relationships and trends with the uncertainty introduced due to the incorrect use of ΔT_g eliminated. However, it should be noted that the estimates of ΔT_a were obtained

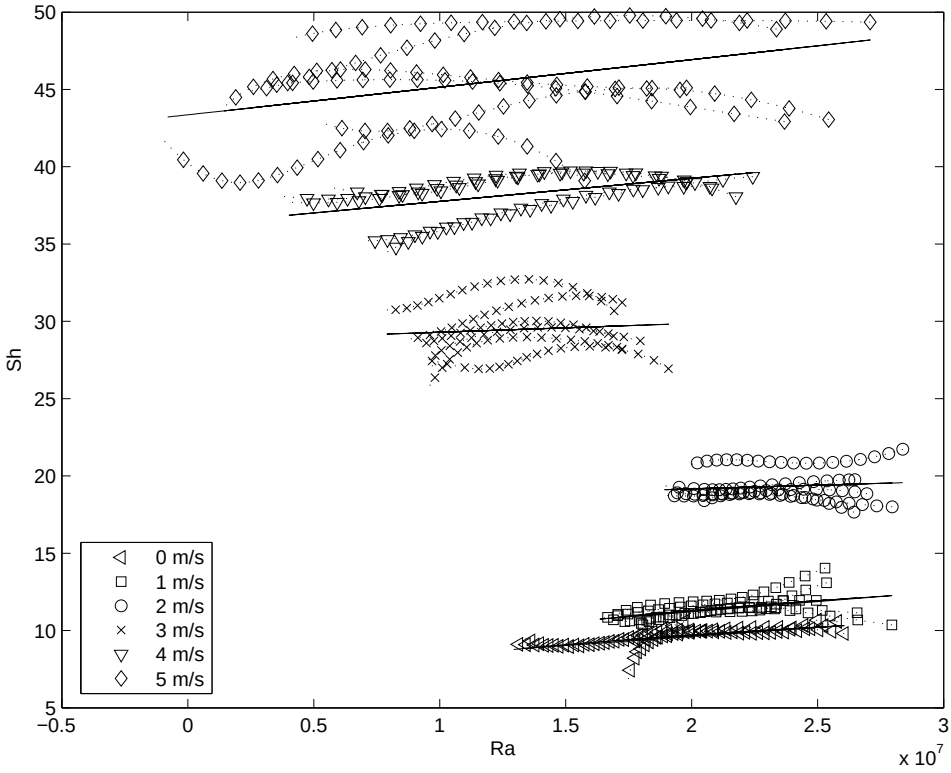

Figure 45: Plot of Sh versus Ra for all wind speeds calculated using the surface temperature with the fit for each wind speed superimposed. Symbols and dotted line show the data and solid lines show the fit.

Table 18: $Sh(Ra)$ relationships for all wind speeds obtained using the surface temperature.

Wind speed (m/s)	$Sh = f(Ra)$
0	$Sh = 0.039(Ra^{0.317})$
1	$Sh = 1.3 \times 10^{-7} Ra + 8.4$
2	$Sh = 1.2 \times 10^{-8} Ra + 19$
3	$Sh = 9 \times 10^{-9} Ra + 32$
4	$Sh = 1.4 \times 10^{-8} Ra + 40$
5	$Sh = 1.3 \times 10^{-8} Ra + 44$

Table 19: A table of the exponent (b_1), prefactor (A_1), slopes (M_1), and intercepts (M_2) of the $Sh(Ra)$ fits and the 95% confidence interval (C.I.) of each calculated using T_s.

Wind speed (m/s)	$b_1 \pm 95\%$C.I.	$M_1 \pm 95\%$C.I.	$A_1 \pm 95\%$C.I.	$M_2 \pm 95\%$C.I.
0	0.317± 0.065	-	0.039± 0.0059	-
1	-	$1.3 \times 10^{-7} \pm 0.23 \times 10^{-7}$	-	8.4± 0.004
2	-	$1.2 \times 10^{-8} \pm 1.4 \times 10^{-8}$	-	19± 2.38
3	-	$9 \times 10^{-9} \pm 0.8 \times 10^{-9}$	-	32± 4.3
4	-	$1.4 \times 10^{-8} \pm 1.0 \times 10^{-8}$	-	40± 6.9
5	-	$1.3 \times 10^{-8} \pm 1.2 \times 10^{-8}$	-	44± 7.2

from a small pool of estimates of T_s, and due to this lack of absolutely reliable surface temperature data, these results cannot be considered to be accurate. However, as it is known that ΔT_a will follow the trend shown in Table 17, the reversal in the $Sh(Ra)$ trends seen at 2 and 3 m/s is reasonable. Thus, it can be argued that experiments for wind speeds 0 - 1 m/s are natural convection dominated, those for wind speeds 1 - 3 m/s are mixed convection dominated and experiments for wind speeds 3 - 5 m/s are forced convection dominated.

Just as in the case of the $Nu(Ra)$ results, it can be seen that Sh is dependent on Ra for wind speeds of 0 and 1 m/s whereas for wind speeds 3 - 5 m/s, Sh is largely independent of Ra as seen from the slope of the $Sh(Ra)$ plot. However, the slope is very close to zero at 2 m/s, thus it can be concluded that the mixed convection region falls between 1 and 3 m/s for this experimental setup and is very close to 2 m/s. The same conclusions can be drawn from the $Sh(Ra)$ fits at each wind speed given by the vectorial additive equation.

6 CONCLUSION

In this work functional forms for mixed convective heat transfer and evaporation at the air-water interface in the presence of an oleyl alcohol monolayer were obtained. To obtain these functions, equations defining natural and forced convective heat and mass transfer as functions of the Rayleigh and Reynolds number respectively were obtained.

It was thus shown that the power law relationships normally associated with natural and forced convective transport over a flat plate can be used to model heat transfer and evaporation at the air-water interface. The equation defining natural convective heat transfer at the air-water interface thus obtained is:

$$Nu_n = 0.67(Ra)^{0.37} \tag{106}$$

whereas the natural convective mass transfer equation which was obtained is:

$$Sh_n = 0.029(Ra)^{0.323} \tag{107}$$

Thus, a power law fit for evaporative heat and mass transfer for natural convective conditions gave a functional form with an exponent of 0.37 $\pm$ 0.08 for heat transfer within a 95% confidence interval. The natural convective mass transfer equation gave a power law fit with an exponent of 0.323 $\pm$ 0.07 within a 95% confidence interval.

The forced convection results gave a power law fit for forced convective heat transfer which agreed with the turbulent flat plate correlation with a Reynolds number exponent of 0.85 for the $Nu(Re)$ relationship and a Reynolds number exponent of 0.81 for the $Sh(Re)$ relationship. The prefactors for the forced convective $Nu(Re)$

and $Sh(Re)$ relationships are 0.1585 and 0.001 respectively. The $Nu(Re)$ and $Sh(Re)$ equations thus obtained are:

$$Nu_f = 0.1585(Re)^{0.85} \tag{108}$$

$$Sh_f = 0.001(Re)^{0.81} \tag{109}$$

A vectorial functional form was used to fit the $Nu(Ra, Re)$ and $Sh(Ra, Re)$ data and obtain a mixed convection equation which fit the entire data. The equation thus obtained defining mixed convective heat transfer is:

$$Nu_m = [(0.67Ra^{0.37})^4 + (0.1585Re^{0.85})^4]^{\frac{1}{4}} \tag{110}$$

whereas the equation defining mixed convective mass transfer is:

$$Sh_m = [(0.029Ra^{0.323})^4 + (0.001Re^{0.81})^4]^{\frac{1}{4}} \tag{111}$$

It was thus shown that heat transfer and evaporation at the air-water interface can be defined by expressing the Nusselt and Sherwood numbers as functions of the Rayleigh and Reynolds numbers in a vectorial additive form. All relationships were evaluated for the air side of the interface and using the gross temperature difference between the bulk water and air as the driving force. The mixed convective equations

predicted the $Nu(Ra, Re)$ and $Sh(Ra, Re)$ data obtained at all wind speeds with reasonable accuracy.

It was concluded that the mixed convective region lies between 1 and 3 m/s for both heat and mass transfer. The $Nu(Ra)$ and $Sh(Ra)$ experimental results in this region are reasonably well predicted by the vectorial additive form and this form is thus adopted for defining mixed convection.

References

[1] F. P. Incropera and D. P. Dewitt. *Fundamentals of Heat and Mass Transfer*. Wiley, 1998.

[2] T. Y. Chu and R. J. Goldstein. Turbulent convection in a horizontal layer of water. *Journal of Fluid Mechanics*, 60:141–159, 1973.

[3] S. Globe and D. Dropkin. Natural-convection heat transfer in liquids confined by two horizontal plates and heated from below. *American Society of Mechanical Engineers – Transactions – Journal of Heat Transfer*, 81C(1):24–28, 1959.

[4] K. B. Katsaros, T. W. Liu, A. B. Joost, and J. E. Tillman. Heat transport and thermal structure in the interfacial boundary measured in an open tank of water in turbulent free convection. *Fluid Mechanics*, 83(2):311–335, 1977.

[5] J. J. Niemela, L. Skrbek, and R. J. Donnelly. Ultra-high Rayleigh number convection in cryogenic helium gas. *Journal of Fluid Mechanics*, pages 141–159, 1973.

[6] T. Watanabe. Flow pattern and heat transfer rate in Rayleigh-Bénard convection. *Physics of Fluids*, 16:972–978, 2004.

[7] D. R. Moore and N. O. Weiss. Two-dimensional Rayleigh-Bénard convection. *Journal of Fluid Mechanics*, 58(289–312), 1973.

[8] S. Kenjereš and K. Hanjalić. Convective rolls and heat transfer in finite-length Rayleigh-Bénard convection: A two-dimensional numerical study. *Phys. Rev. E*, 62:7987–7998, 2000.

[9] M. Ishiwatari, S. I. Takehiro, and Y. Y. Hayashi. The effects of thermal conditions on the cell sizes of two-dimensional convection. *J. Fluid Mech.*, 281:33–50, 1994.

[10] S. Ciliberto, S. Cioni, and C. Laroche. Large-scale flow properties of turbulent thermal convection. *Physical Review E*, 54:5901–5904, 1996.

[11] G. Zocchi, E. Moses, and A. Libchaber. Coherent structures in turbulent convection, an experimental study. *Physica A*, 166:387–407, 1990.

[12] R. Krishnamurti and L. N. Howard. Large-scale flow generation in turbulent convection. *Proc. Natl. Acad. Sci*, 78:1987–1985, 1981.

[13] H. Tanaka and H. Miyata. Turbulent natural convection in a horizontal water layer heated from below. *Int. J. Heat Mass Transfer*, 23:1273–1281, 1980.

[14] J. N. Shadid and R. J. Goldstein. Visualization of longitudinal convection roll instabilities in an inclined enclosure heated from below. *J. Fluid Mech.*, 215:61–84, 1990.

[15] R. J. Goldstein and T. Y. Chu. Thermal convection in a horiztonal layer of air. *Prog. Heat and Mass Transfer*, 2:55–75, 1969.

[16] E. F. C. Somerscales and I. W. Gazda. Thermal convection in high prandtl number liquids at high Rayleigh numbers. *Int. J. Heat Mass Transfer*, 12:1491–1511, 1969.

[17] R. H. Kraichnan. Turbulent thermal convection at arbitrary Prandtl number. *Phys. Fluids*, 5:1374–1389, 1962.

[18] W. V. R. Malkus. The heat transfer and spectrum of thermal turbulence. *Proc. Roy Soc. A*, 225:196 –212, 1954.

[19] L. N. Howard. Convection at high Rayleigh number. In H. Görtler, editor, *Proc. 11th Int. Congr. on Applied Mechanics*, pages 1109–1115. Springer-Verlag, 1966.

[20] L. N. Howard. Heat transport by turbulent convection. *J. Fluid Mech.*, 17:405–432, 1963.

[21] F. H. Busse. On Howard's upper bound for heat transport by turbulent convection. *J. Fluid Mech.*, 37:457–477, 1969.

[22] W. V. R. Malkus. Discrete transitions in turbulent convection. *Proc. Roy Soc. A*, 225:185 – 191, 1954.

[23] E. Bodenschatz, W. Pesch, and G. Ahlers. Recent developments in Rayleigh-Bénard convection. *Ann. Rev. Fluid Mech.*, 32:709–778, 2000.

[24] J. J. Niemela, L. Skrbek, K. R. Sreenivasan, and R. J. Donnelly. Turbulent convection at very high Rayleigh numbers. *Nature*, 404:837–840, 2000.

[25] J. J. Niemela, L. Skrbek, C. Swanson, S. Hall, K. R. Sreenivasan, and R. J. Donnelly. New results in cryogenic helium flows at ultra-high Reynolds and Rayleigh numbers. *Journal of Low Temperature Physics*, 121:417–422, 2000.

[26] J. J. Niemela, L. Skrbek, and R. J. Donnelly. Ultra-high Rayleigh number convection in cryogenic helium gas. *Physica B*, 284:61–62, 2000.

[27] J. J. Niemela, L. Skrbek, K. R. Sreenivasan, and R. J. Donnelly. The wind in confined thermal convection. *J. Fluid Mech.*, 449:169–178, 2001.

[28] J. J. Niemela, L. Skrbek, K. R. Sreenivasan, and R. J. Donnelly. Self-sustained large-scale flow in turbulent cryogenic convection. *Journal of Low Temperature Physics*, 126:297–302, 2002.

[29] J. J. Niemela and K. R. Sreenivasan. Confined turbulent convection. *J. Fluid Mech.*, 481:355–384, 2003.

[30] W. H. Carrier. The temperature of evaporation. *ASHRAE Transactions*, 24:25, 1918.

[31] W. H. Carrier. Evaporation from free water surface. *US Agricultural dept. Technical Bulletin*, 1(271), 1931.

[32] M. T. Pauken, B. Farley, S. M. Jeter, and S. I. Abdel-Khalik. Experimental investigation of combined turbulent free and forced evaporation. *ASHRAE Transactions*, 101:90–96, 1995.

[33] M. T. Pauken, B. Farley, S. M. Jeter, and S. I. Abdel-Khalik. Experimental investigation of water evaporation into low-velocity air currents. *ASHRAE Transactions*, 101(1):90–96, 1995.

[34] M. Chattree and S. Sengupta. Heat transfer and evaporation from heated water bodies. *Journal of Heat Transfer, Transactions ASME*, 107(4):779–787, 1985.

[35] A. H. Rasmussen, M. Hondzo, and H. G. Stefan. Test of several evaporation equations for water temperature simulations in lakes. *Water Resources Bulletin*, 31(6):1023–1028, 1995.

[36] J. T. Zhang and B. X. Wang. Evaporation rates of water from concentrated oil-in-water emulsions. *International Journal of Heat and Mass Transfer*, 46(26):5059–5064, 2003.

[37] H. T. El-Dessouky, H. M. Ettouney, I. M. Alatiqi, and M. A. Al-Shamari. Evaporation rates from fresh and saline water in moving air. *Industrial and Engineering Chemistry Research*, 41(3):642–650, 2002.

[38] E. M. Sparrow, G. K. Kratz, and M. J. Schuerger. Evaporation of water from a horizontal surface due to natural convection. *Journal of Heat Transfer, Transactions ASME*, 105(3):469–475, 1983.

[39] W. M. Kays and M. E. Crawford. *Convective Heat and Mass Transfer*. McGraw Hill, 1980.

[40] E. Sartori. Convection coefficient equations for forced air flow over flat surfaces. *Solar Energy*, 80:1063–1071, 2006.

[41] T. Inagaki and K. Kitamura. Turbulent forced and free convection along a vertical flat plate (opposing flow). *Heat Transfer - Japanese Research*, 20:203–216, 1991.

[42] M. A. Ebadian and P. H. Oosthuizen. Fundamentals of forced convection heat transfer. *ASME-HTD*, 210:171, 1992.

[43] E. J. Braga. Turbulent heat transfer in an enclosure with a horizontal permeable plate in the middle. *Journal of Heat Transfer*, 128:171, 2006.

[44] A. Ortega, D. Agonafer, and B.W. Webb. Heat transfer in electronic equipment. *ASME-HTD*, pages 1122–1129, 1991.

[45] M. Hirota, H. Fujita, H. Yokosawa, H. Nakai, and H. Itoh. Turbulent heat transfer in a square duct. *International Journal of Heat and Fluid Flow*, 80:170–180, 1997.

[46] P. H. Oosthuizen and M. Bassey. Experimental study of combined forced and free-convective heat transfer from flat plates to air at low Reynolds numbers. *Journal of Heat Transfer, Transactions ASME*, 95(1):120–121, 1973.

[47] S. C. R. Dennis and N. Smith. Forced convection from heated flat plate. *Journal of Fluid Mechanics*, 24(3):509–519, 1966.

[48] M. Rebay, J. Padet, and S. Kakac. Forced convection from a microstructure on a flat plate. *Heat and Mass Transfer/Waerme- und Stoffuebertragung*, 43(4):309–317, 2007.

[49] G. H. Juncu. Unsteady forced convection heat/mass transfer from a flat plate. *Heat and Mass Transfer/Waerme- und Stoffuebertragung*, 41(12):1095–1102, 2005.

[50] H. R. Nagendra. Transient forced convection heat transfer from an isothermal flat plate. *AIAA Journal*, 11(6):876–878, 1973.

[51] A. J. Chambers, P. A. Mangerella, R. L. Street, and E. Y. Hsu. Experimental investigation of transfer of momentum at an air-water interface. *Stanford Univ, Dep Civ Eng, Tech Rep*, 133:156, 1970.

[52] C. Gau, Y. C. Jeng, and C. G. Liu. An experimental study on mixed convection in a horizontal rectangular channel heated from the side. *Journal of Heat Transfer*, 122:701–707, Nov 2000.

[53] P. H. Oosthuizen and S. Madan. Combined convective heat transfer from horizontal cylinders in air. *Journal of Heat Transfer, HTD*, pages 194–196, 1970.

[54] A. P. Hatton, D. D. James, and H. W. Swire. Combined forced and natural convection with low speed air flow over horizontal cylinders. *Journal of Fluid Mechanics*, 42(1):17–31, 1993.

[55] J. Donald. Comparison of correlations and experiments in opposing flow, mixed convection heat transfer in a vertical tube with Grashof number variation. *International Journal of Heat Transfer*, 39(5):1033–1038, 1993.

[56] S. Baskaya, U. Erturhan, and M. Sivrioglu. Experimental investigation of mixed convection from an array of discrete heat sources at the bottom of a horizontal channel. *Heat Mass Transfer*, 42, 2005.

[57] T. W. Jackson and H. H. Yen. Combining forced and free convection equations to represent combined heat transfer coefficients for a horizontal cylinder. *Journal of Heat Transfer*, 93(2):247–248, 1971.

[58] E. M. Sparrow and J. L. Gregg. Buoyancy effects in forced convection flow. *Journal of Applied Mechanics*, pages 133–134, 1959.

[59] Y. Mori. Buoyancy effects in forced laminar convection flow over a horizontal flat plate. *Journal of Heat Transfer*, pages 479–482, 1969.

[60] N. Ramachandran, B. F. Armaly, and T. S. Chen. Turbulent mixed convection over an isothermal horizontal flat plate. *Journal of Heat Transfer (HTD), Transactions of the ASME*, 112:124–129, 1987.

[61] W. R. Risbeck, T. S. Chen, and B. Armaly. Laminar mixed convection on horizontal flat plates with variable surface heat flux. *International Journal of Heat Mass Transfer*, 37(4):699–704, 1994.

[62] N. Afzal and T. Hussain. Mixed convection over a horizontal plate. *Journal of Heat Transfer HTD, Transactions of the ASME*, 106:240–241, 1984.

[63] N. Hattori and K. Tokunaga. Convection heat transfer from three circular cylinders to water at relatively low Reynolds number. *Transactions of the Japan Society of Mechanical Engineers*, 59:556–563, 1993.

[64] R. Kronig and J. Bruijsten. On the theory of heat and mass transfer from a sphere in a flowing medium at low Reynolds number. *Applied Scientific Research*, A2:439–446, 1965.

[65] F. J. Ocampo-Torres and M. A. Donelan. Laboratory measurements of mass transfer of carbon dioxide and water vapor for smooth and rough flow conditions. *Tellus*, 46(B):16–32, 1992.

[66] T. Kumada, T. Hirota, N. Tamura, and R. Ishiguro. Heat and mass transfer with liquid evaporation into a turbulent air stream. *Letters in Heat and Mass Transfer*, 9(1):1–9, 1982.

[67] Yoshiro Katto, Hideo Koizumi, and Tatuo Yamaguchi. Turbulent heat transfer of a gas flow on an evaporation liquid surface. *Bulletin of the JSME*, 18(122):866–873, 1975.

[68] L. S. Klyachko. Theory and calculation of evaporation processes from liquid surfaces. *Zh. Tekh. Fiz.*, 6:4–11, 1936.

[69] B. M. Smolsky and G. T. Sergeyev. Heat and mass transfer with liquid evaporation. *International Journal of Heat and Mass Transfer*, 5:1011–1021, 1962.

[70] B. F. Boyarshinov, E. P. Volchkov, and V. I. Terekhov. Heat and mass transfer with evaporation of a liquid into gaseous flow. *Russian Journal of Engineering Thermophysics*, 1(1):93–112, 1991.

[71] I. Gentle and G. Barnes. *Interfacial Science*. Oxford, 2005.

[72] A. W. Adamson. *Physical Chemistry of Surfaces*. Wiley, 1990.

[73] G. L. Gaines. *Insoluble Monolayers at Liquid-Gas Interface*. Wiley, 1966.

[74] K. A. Flack, J. R. Saylor, and G. B. Smith. Near surface turbulence for evaporative convection at an air/water interface. *Physics of Fluids*, 13:3338–3345, 2001.

[75] V. K. La Mer, T. W. Healy, and L. A. G. Aylmore. The transport of water through monolayers of long chain n-parafinnic alcohols. *Journal of Colloid Science*, 19:673–684, 1964.

[76] R. Kurzeja. Personal communication.

[77] K. Klink. Climatological mean and interannual variance of united states surface wind speed, direction and velocity. *International Journal of Climatology*, 19:471–488, 1999.

[78] P. H. Oosthuizen and D. Naylor. *Introduction to Convective Heat Transfer Analysis*. William C Brown Pub, 1998.

[79] S. Phongikaroon, R. Hoffmaster, K. P. Judd, G. B. Smith, and R. A. Handler. Effect of temperature on the surface tension of soluble and insoluble surfactants of hydrodynamical importance. *Journal of Chemical and Engineering Data*, 50(5):1602–1607, 2005.

[80] A. E. Alexander and J. H. Brooks. Losses by evaporation and solution from monolayers of long-chain aliphatic compounds. *Proceedings, International Congress of Surface Activity*, page 196, 1960.

[81] O. Reynolds. British association for advancement of science report. *British Association for Advancement of Science*, pages 524 – 525, 1881.

[82] C. D. Hodgman, R. C. Weast, and S. M. Selby. *Handbook of Chemistry and Physics*. Chemical Rubber Publishing Company, 2004.

[83] E. M. Sparrow, R. J. Goldstein, and V. K. Jonsson. Thermal instability in a horizontal fluid layer: effect of boundary conditions and nonlinear temperature profile. *J. Fluid Mech.*, 18:513–528, 1964.

[84] E. M. Sparrow, R. B. Husar, and R. J. Goldstein. Observations and other characteristics of thermals. *J. Fluid Mech.*, 41:793–800, 1970.

[85] J. R. Taylor. *Introduction To Error Analysis*. University Science Books, 1997.

[86] R. S. Figliola and D. E. Beasley. *Theory and Design for Mechanical Measurements*. Wiley, 2001.

[87] J. Wu. Parameterization of sensible and latent heat fluxes across the sea surface. *ASME,HTD*, 246:151–163, 1993.

[88] A. M. Garon and R. J. Goldstein. Velocity and heat transfer measurements in thermal convection. *Physics of Fluids*, 16(11):1818–1825, 1973.